

UNIVERSITAT POLITÈCNICA DE CATALUNYA
FACULTAT DE MATEMÀTIQUES I ESTADÍSTICA
ESCOLA TÈCNICA SUPERIOR D'ENGINYERS
DE CAMINS, CANALS I PORTS DE BARCELONA

DEPARTAMENT DE MATEMÀTICA APLICADA III

MESH-FREE METHODS AND FINITE ELEMENTS: FRIEND OR FOE?

by

SONIA FERNÁNDEZ MÉNDEZ

Doctoral Thesis

Advisor: Antonio Huerta

Barcelona, Setember 2001

To Sebas and my parents

Contents

| | |
|--|-------------|
| Acknowledgements | xiii |
| 1 Introduction | 1 |
| 2 State of the art in mesh-free methods | 5 |
| 2.1 Interpolation in mesh-free methods | 7 |
| 2.1.1 Smooth Particle Hydrodynamic | 7 |
| 2.1.2 Moving Least Squares interpolants | 14 |
| 2.2 Implementation details | 24 |
| 2.2.1 Collocation methods | 24 |
| 2.2.2 Methods based on a Galerkin weak form | 25 |
| 2.2.3 Essential boundary conditions | 28 |
| 2.2.4 EFG implementation details: computation of EFG interpolation functions and derivatives | 31 |
| 3 Locking in the incompressible limit for the Element Free Galerkin method | 33 |
| 3.1 Introduction | 33 |
| 3.2 Volumetric locking in standard finite elements | 34 |
| 3.2.1 Preliminaries | 34 |
| 3.2.2 Bilinear finite elements (Q1) | 36 |
| 3.2.3 Biquadratic finite elements (Q2) | 38 |
| 3.3 Volumetric locking in element free Galerkin methods | 39 |
| 3.3.1 Locking for bilinear consistency | 41 |
| 3.3.2 Locking for biquadratic consistency | 44 |
| 3.4 Numerical examples | 47 |
| 3.4.1 The cantilever beam | 47 |

| | | |
|----------|--|------------|
| 3.4.2 | The plate with a hole | 49 |
| 3.4.3 | The Prandtl's punch test | 50 |
| 3.5 | Conclusions | 54 |
| 4 | Enrichment and Coupling of the Finite Element and Mesh-free Methods | 57 |
| 4.1 | Introduction | 57 |
| 4.2 | A hierarchical mixed approximation: finite elements with EFG | 58 |
| 4.2.1 | Evaluation of the mesh-free shape functions N_j^p | 60 |
| 4.3 | Coupled Finite Element and Element-Free Galerkin | 63 |
| 4.4 | Finite Element enrichment with Element-Free Galerkin | 67 |
| 4.5 | Numerical examples | 72 |
| 4.5.1 | Coupled EFG-FEM | 72 |
| 4.5.2 | Coupled and Enriched EFG-FEM | 73 |
| 4.5.3 | Finite element enrichment with EFG in a 2D Poisson problem | 76 |
| 4.5.4 | Finite element enrichment with EFG in nonlinear computational mechanics | 77 |
| 4.5.5 | Adaptivity in 2D convection-diffusion and diffusion-reaction problems coupling finite elements and particles | 83 |
| 4.6 | Conclusions | 91 |
| 5 | Time accurate consistently stabilized mesh-free methods for convection dominated problems | 93 |
| 5.1 | Introduction | 93 |
| 5.2 | Time and space discretization for the transient convection-diffusion equation | 95 |
| 5.2.1 | Time discretization | 96 |
| 5.2.2 | Spatial discretization. (I) Galerkin and stabilized formulations for the FE method | 97 |
| 5.2.3 | Spatial discretization. (II) Galerkin and stabilized formulations for the EFG method | 100 |
| 5.3 | Convergence of the Galerkin approach and the stabilized formulations | 101 |
| 5.4 | Numerical examples | 104 |
| 5.4.1 | 1D example | 105 |
| 5.4.2 | 2D example | 106 |
| 5.5 | Concluding remarks | 108 |
| 6 | Summary and future developments | 111 |

| | | |
|----------|---|------------|
| A | Convergence of finite elements enriched with mesh-free methods | 115 |
| A.1 | Previous results | 116 |
| A.2 | FE element properties | 117 |
| A.3 | Convergence of FE enriched with EFG | 121 |
| A.4 | Concluding remarks | 127 |
| B | Numerical simulation of active carbon canisters | 129 |
| B.1 | Numerical examples | 133 |
| B.2 | Conclusions and remarks | 135 |

List of Tables

| | | |
|-----|--|----|
| 3.1 | Mode classification for a distribution of 4×4 particles/nodes | 42 |
| 3.2 | Mode classification for a distribution of 5×5 particles/nodes | 42 |
| 3.3 | Mode classification for a distribution of 4×4 particles/nodes | 46 |
| 3.4 | Mode classification for a distribution of 5×5 particles/nodes | 46 |
| 3.5 | Load at the final displacement for the Prandtl's punch test. | 53 |
| 4.1 | Measures of error for 6 particles and 5 nodes. | 74 |
| 4.2 | Measures of error for 11 particles and 5 nodes. | 74 |

List of Figures

| | | |
|------|--|----|
| 2.1 | SPH interpolation functions and approximation of $u(x) = 1 - x^2$ with cubic spline window function, distance between particles $h = 0.5$ and quadrature weights $\omega_i = h$, for $\rho/h = 1, 2, 4$ | 9 |
| 2.2 | Cubic spline and corrected window function for polynomials of degree 2. | 10 |
| 2.3 | Modified cubic splines and particles, $h = 0.5$, and SPH discrete approximation for $u(x) = x$ with $\rho/h = 2$ in a “not bounded domain”. | 11 |
| 2.4 | Modified cubic splines and particles, $h = 0.5$, and SPH discrete approximation for $u(x) = x$ with $\rho/h = 2$ in a bounded domain. | 11 |
| 2.5 | Interpolation functions with $\rho/h \simeq 1$ (similar to finite elements) and $\rho/h = 2.6$, with cubic spline and linear consistency. | 19 |
| 2.6 | Shape function and derivatives for linear finite elements and the EFG interpolation. | 20 |
| 2.7 | Distribution of particles, EFG interpolation function and derivatives, with $\rho/h \simeq 2.2$ with circular supported cubic spline and linear consistency. | 21 |
| 2.8 | Particle distribution (in blue) and two possible cell structures. The first one is simpler; however, the second one is adapted to the geometry in a more efficient way. | 26 |
| 2.9 | Particle distribution (in blue) and underground mesh. | 27 |
| 2.10 | Mixed interpolation with linear finite element nodes near the boundary and particles in the interior of the domain, with $\rho/h = 3.2$, cubic spline and linear consistency in all the domain. | 29 |
| 3.1 | Non locking modes for one bilinear element (Q1) | 37 |
| 3.2 | Physical locking mode for one bilinear element (Q1) | 37 |
| 3.3 | Non-physical locking modes for one bilinear element (Q1) | 37 |
| 3.4 | Comparison between the hourglass mode and a divergence-free bending field | 37 |

| | | |
|------|--|----|
| 3.5 | Modes for the Q2 element (9 nodes) | 38 |
| 3.6 | Modes of four Q1 elements (9 nodes) | 38 |
| 3.7 | Modes for a 3×3 distribution of particles with Q_1 and $\rho/h = 1.2$ | 40 |
| 3.8 | Modes for a 3×3 distribution of particles with Q_1 and $\rho/h = 2.2$ | 40 |
| 3.9 | Evolution of the eigenvalue as ν goes to 0.5 for the same non-physical locking mode obtained with $\rho/h = 1.2$, and 2.2. | 41 |
| 3.10 | Modes for a 4×4 distribution of particles with Q_1 and $\rho/h = 1.2$ | 43 |
| 3.11 | Modes for a 4×4 distribution of particles with Q_1 and $\rho/h = 2.2$ | 43 |
| 3.12 | Modes for a 4×4 distribution of particles with Q_1 and $\rho/h = 3.2$ | 43 |
| 3.13 | Evolution of the eigenvalue as ν goes to 0.5 for the same non-physical locking mode obtained with $\rho/h = 1.2$, 2.2, and 3.2. | 44 |
| 3.14 | Modes for a 3×3 distribution of particles with Q_2 and $\rho/h = 2.2$ | 45 |
| 3.15 | Modes for a 4×4 distribution of particles with Q_2 and $\rho/h = 2.2$ | 45 |
| 3.16 | Modes for a 4×4 distribution of particles with Q_2 and $\rho/h = 3.2$ | 45 |
| 3.17 | Cantilever beam problem | 47 |
| 3.18 | Relative L_2 error with FE and $\nu = 0.3, 0.4999, 0.499999$ | 48 |
| 3.19 | Relative L_2 error with EFG and $\nu = 0.3, 0.4999, 0.499999$ | 48 |
| 3.20 | Relative L_2 error with Q_1 and $\rho/h = 1.6$ (left), with Q_1 and $\rho/h = 3.2$ (centre) and with Q_2 and $\rho/h = 3.2$ (right). | 48 |
| 3.21 | Problem statement for the plate with hole and discretizations. | 49 |
| 3.22 | FE, $\nu = 0.3$ (left) and $\nu = 0.4999$ (right) | 50 |
| 3.23 | EFG, $\nu = 0.3$ (left) and $\nu = 0.4999$ (right) | 50 |
| 3.24 | Prandtl's punch test: problem statement | 51 |
| 3.25 | Load <i>versus</i> displacement with 9×9 particles, $m = 1$ and $\nu = 0.49$ | 51 |
| 3.26 | Load <i>versus</i> displacement with 9×9 (up) and 17×17 (down) particles, $m = 1$ and $\nu = 0.49$ | 52 |
| 3.27 | Reaction force vs displacement with 9×9 particles and $\nu = 0.49999$ | 53 |
| 3.28 | Load <i>versus</i> displacement with 9×9 (up) and 17×17 (down) particles, Q_2 consistency and $\nu = 0.49$ | 54 |
| 4.1 | Coupled Finite Element and Element-Free Galerkin | 60 |
| 4.2 | Finite Element Enrichment with Element-Free Galerkin | 60 |
| 4.3 | Substitution of a finite element node by one particle. Non admissible distribution. | 62 |
| 4.4 | Substitution of a finite element node by two particles. Admissible distribution. | 62 |

| | | |
|------|---|----|
| 4.5 | Non admissible distribution. $\tilde{\Omega}$ is under the influence of only one particle. | 62 |
| 4.6 | Approximation functions before and after imposing the consistency condition of order one. | 63 |
| 4.7 | Coupled approximation functions with consistency of order one and two particles in the transition region $\tilde{\Omega}$ | 64 |
| 4.8 | Coupled approximation functions with consistency of order two and two different distributions of particles. | 65 |
| 4.9 | Convergence of FEM and coupled FEM-EFG for a distribution of elements and particles shown in figure 4.6. | 66 |
| 4.10 | Convergence for a mesh and mesh-free refinement: constant h/ρ and $h \rightarrow 0$ | 69 |
| 4.11 | Convergence for a mesh refinement: constant ρ and $h \rightarrow 0$ | 69 |
| 4.12 | Convergence for a mesh-free refinement: constant h and $\rho \rightarrow 0$ | 69 |
| 4.13 | Function $u(x)$ defined in (4.4.1) | 70 |
| 4.14 | Approximation functions —4 particles and 5 nodes— (left) and interpolation result, $u^\rho + u^h$, with error distribution (right). | 73 |
| 4.15 | Approximation functions —12 particles and 5 nodes— (left) and interpolation result, $u^\rho + u^h$, with error distribution (right). | 73 |
| 4.16 | Approximation functions: 6 particles and 5 nodes | 74 |
| 4.17 | Mixed interpolation with 6 particles and 5 nodes | 75 |
| 4.18 | Mixed interpolation with 11 particles and 5 nodes | 75 |
| 4.19 | Analytical solution and section along $y = x$ | 77 |
| 4.20 | Finite element mesh and error distribution. | 78 |
| 4.21 | Approximation with 8×8 Q1 finite elements | 78 |
| 4.22 | Finite element mesh enriched with particles and error distribution of the mixed approximation. | 78 |
| 4.23 | Finite element contribution u^h , enrichment with EFG u^ρ and mixed approximation $u^h + u^\rho$ | 79 |
| 4.24 | Problem statement: rectangular specimen with one centred imperfection. | 80 |
| 4.25 | Final mesh with its corresponding equivalent inelastic strain for a standard finite element (8 noded elements) computation (top) and distribution of particles with its inelastic strain distribution for EFG (bottom). | 81 |
| 4.26 | Coarse finite element mesh (Q1 elements) with its corresponding equivalent inelastic strain (top) and mixed interpolation with its equivalent inelastic strain distribution (bottom). | 82 |

| | | |
|------|--|-----|
| 4.27 | Force <i>versus</i> displacement (left) and evolution of the equivalent inelastic strain along (A-A') for each approximation (right). | 83 |
| 4.28 | FE mesh (11x11=121 nodes) and Galerkin solution with $\nu = 10^{-5}$, $\sigma = 1$ | 84 |
| 4.29 | Mixed distribution with 81 nodes (o) and 387 particles (x), and Galerkin solution with $\nu = 10^{-5}$, $\sigma = 1$ | 84 |
| 4.30 | Convection-diffusion problem statement. | 85 |
| 4.31 | FE mesh (21x21=441 nodes) and Galerkin solution for $ a = 1$, $\nu = 0.0025$ | 86 |
| 4.32 | FE mesh (81x81=6561 nodes) and Galerkin solution for $ a = 1$, $\nu = 0.0025$ | 86 |
| 4.33 | Discretization with 361 nodes and 289 particles and Galerkin solution for $ a = 1$, $\nu = 0.0025$ | 86 |
| 4.34 | FE mesh (21x21=441 nodes) and SUPG solution with $\tau = 0.025$ and $\tau = 0.005$, for $ a = 1$, $\nu = 10^{-4}$ | 87 |
| 4.35 | Discretization with 361 nodes (o) and 289 particles (x), and SUPG solution with $\tau = 0.025$ and $\tau = 0.005$, for $ a = 1$, $\nu = 10^{-4}$ | 88 |
| 4.36 | Convection-diffusion problem statement. | 89 |
| 4.37 | SUPG solution with 15×15 linear finite elements and $\tau = 0.0333$, and detection of elements with $\ \nabla u\ > \frac{1}{3h}$ (in white) | 89 |
| 4.38 | Mixed distribution with 210 nodes (o) and 211 particles (x), and corresponding SUPG solution with $\tau = 0.0333$ (left) and $\tau = 0.015$ (right) | 90 |
| 4.39 | Section along $x = 0.75$ for the finite element interpolation with $\tau = 0.0333$ and the mixed interpolation with $\tau = 0.0333$ and $\tau = 0.015$ | 91 |
| 5.1 | Finite elements convergence results with $h = 0.001$ and $a = 1$ | 101 |
| 5.2 | EFG convergence results with $h = 0.01$ (distance between particles), $\rho/h = 3.2$, $\mathbf{P} = \{1, x\}^T$ and $a = 1$ | 102 |
| 5.3 | Finite elements convergence results with $h = 0.001$ and $a = 1$ | 104 |
| 5.4 | EFG convergence results with $h = 0.01$, $\rho/h = 3.2$, $\mathbf{P} = \{1, x\}^T$ and $a = 1$ | 104 |
| 5.5 | R_{11} solution at $t = 1$ for $a = 1$, $\nu = 10^{-3}$, $\rho/h = 3.2$ with $c = 1$ | 105 |
| 5.6 | R_{22} solution at $t = 1$ for $a = 1$, $\nu = 10^{-3}$, $\rho/h = 3.2$ with $c = 2$ | 106 |
| 5.7 | Problem statement for the 2D example | 107 |
| 5.8 | Galerkin solution and contour plot at $t = 15.9$ for $\nu = 10^{-5}$, $h = 0.05$, $\rho/h = 3.2$ with $c = 1$ for R_{11} and $c = 3$ for R_{22} | 107 |
| 5.9 | Least-squares solution and contour plot at $t = 15.9$ for $\nu = 10^{-5}$, $h = 0.05$, $\rho/h = 3.2$ with $c = 1$ for R_{11} and $c = 3$ for R_{22} | 108 |

| | | |
|------|---|-----|
| 5.10 | Section along $x = 0.8$ | 109 |
| 5.11 | Section along $y = x$ | 109 |
| B.1 | Canister location | 130 |
| B.2 | Canister | 131 |
| B.3 | Active carbon and several canisters | 132 |
| B.4 | Three 2D canister models with active carbon (in green) and air cambers (in yellow) | 133 |
| B.5 | Evolution of the concentration at five different time steps for the three canisters described in figure B.4 | 134 |
| B.6 | Concentration in a 3D canister and orthogonal cut. | 135 |

Acknowledgements

I would like to thank Antonio Huerta, my supervisor, for his suggestions, support and dedication during this research. He has been an important motor in the development of this thesis. I am also thankful to my colleagues of the *Departament de Matemàtica Aplicada III* of the *Universitat Politècnica de Catalunya*, I would not have been able to arrange teaching and research during this last five years without them. In particular I would like to thank Pedro Díez, Antonio Rodríguez-Ferran and Josep Sarrate for the interesting discussions and support.

Of course, I am also grateful to my family, with a particular mention to Sebas, for his support, patience and good-natured character.

Partial financial support to this research has been provided by the *Ministerio de Educación y Cultura* (grant number: TAP98–0421), the *Comisión Interministerial de Ciencia y Tecnología* (grant number: 2FD97–1206), the *Escola Tècnica Superior the Camins Canals i Ports de Barcelona*, the *Departament de Matemàtica Aplicada III* and the *Universitat Politècnica de Catalunya*. Their support is gratefully acknowledged.

Barcelona
Setember, 2001

Sonia Fernández-Méndez

Chapter 1

Introduction

Recently the limitations of conventional computational methods, such as finite elements, finite volumes or finite difference methods, became apparent. There are many problems of industrial and academic interest which cannot be easily treated with these classical mesh-based methods: for example, the simulation of manufacturing processes such as extrusion and molding where it is necessary to deal with extremely large deformations of the mesh, or simulations of failure where the modelization of the propagation of cracks with arbitrary and complex paths is needed. The underlying structure of the classical mesh-based methods, which strongly depends on their reliance on a mesh, is not ideally suited for the treatment of discontinuities that do not coincide with the original mesh edges. With a mesh-based method, the most viable strategy for dealing with moving discontinuities is to remesh whenever it is necessary in order to keep the mesh edges coincident with the discontinuities throughout the evolution of the problem. The remeshing process, and projection of quantities of interest between successive meshes, usually leads to degradation of accuracy and complexity in the computer program, and often results in an excessive computational cost.

The objective of mesh-free methods is to eliminate at least part of this mesh dependent structure by constructing the approximation entirely in terms of nodes (usually called particles in the context of mesh-free methods). Moving discontinuities or interfaces can usually be treated without remeshing with minor costs and accuracy degradation, see for instance (Belytschko and Organ 1997). Thus the range of problems that can be addressed by mesh-free methods is much wider than mesh-based methods. Moreover, large deformations can be handled more robustly with mesh-free methods because the interpolation is not based on elements whose distortion may degrade the accuracy. This is useful in both fluid and solid computations.

Moreover, one of the major drawbacks of mesh-based methods is the difficulty in en-

sureing for any real geometry a smooth, painless and seamless integration with Computer Aided Engineering (CAE), industrial Computer Aided Design (CAD) and Computer Aided Manufacturing (CAM) tools. Mesh-free methods were design not to suffer from the same problems. The freedom in the definition of the shape/interpolation functions is the key issue. The advantages of mesh-free methods for 3D computations will become more apparent.

On the other hand, mesh-free methods present obvious advantages in adaptive processes. There are *a priori* error estimates for most of the mesh-free methods, see for instance (Liu, Li and Belytschko 1997). This allows the definition of adaptive refinement processes as it is usual in finite element computations: an *a posteriori* error estimation is computed and the solution is improved adding nodes/particles where it is needed, until the error becomes acceptable, see (Huerta, Rodríguez-Ferran, Díez and Sarrate 1999) for details. With a mesh-based method a new finite element mesh must be computed in order to include the new nodes in the interpolation. The cost and difficulty of remeshing is not negligible. In fact, it represents an important drawback in finite element 3D computations. However, mesh-free methods allow refinement without any remeshing cost: the interpolation does not depend on connectivities, and thus, particles can be added with total freedom.

Although mesh-free methods were originated about twenty-five years ago, the popularization of these methods still requires further research. The aim of this thesis is to advance in the development and understanding of these methods through some contributions in this novel research line.

There are different mesh-free methods which are based on different developments and with different properties. Although these methods have a lot of points in common, there is a real need of classifying, ordering and comparing mesh-free methods. Thus, first of all an introductory description of the most common mesh-free methods is presented in chapter 2 with special attention on the differences and similarities between the different formulations.

Moreover, the behaviour of mesh-free methods and its comparison with finite elements is still an open topic in many problems. It is well known that mesh-free methods, such as the Element Free Galerkin (EFG) method, performs much better than standard finite elements in some problems, see for instance (Bouillard and Suleau 1998) or (Askes, de Borst and Heeres 1999). However, finite element methods are still more competitive in some other problems. Thus, one objective of this work is to determine in which situations mesh-free methods can be advantageous or not. For instance, chapter 3 is devoted to the study of volumetric locking in the EFG method. As it is shown in the examples, volumetric locking can drastically degrade the finite element solution in mechanical problems. The objective

is to verify if, as it was originally claimed, mesh-free methods do not exhibit volumetric locking. As will be seen, this is not true: although the EFG method can avoid or alleviate locking in some particular problems, chapter 3 shows through modal analysis that the EFG method is not free from locking. The modal analysis also justifies the better behaviour of the EFG, compared with finite elements, in this kind of problems. Although all the developments are done for the EFG method, all the results can be easily extended to other particle methods.

Results in Chapter 3 show how in some situations mesh-free methods can perform much better than mesh-based methods. However, from a practical point of view, the use of finite elements presents several advantages: the computation and integration of the shape functions are less costly, essential boundary conditions can be implemented in a more simple way (see section 2.2.3 for essential boundary conditions in mesh-free methods), and, above all, they are widely used and trusted by practitioners. In order to take advantage of both methods, a mixed interpolation that combines the EFG interpolation and the finite element interpolation is presented in chapter 4. Although several authors have already proposed to use mixed finite elements and mesh-free interpolations, in chapter 4 a unified and general formulation for mixed interpolations is presented. In particular, this formulation can be applied in two useful situations: enrichment and coupling. The first one (enrichment) allows increasing the order of the finite element interpolation just adding particles where it is wanted. This is comparable to h - p refinement in finite elements. However, the presented approach avoids remeshing and the computational difficulties of non-conforming finite elements. An *a priori* error estimate is presented and proved for this situation in appendix A. In the second one (coupling) the domain is decomposed in one region where only finite elements are present, another region where only particles are present and a transition region where both particles and elements are coupled in order to preserve consistency and continuity in the interpolation. Thus, the finite element interpolation can be used in almost all the domain, with less computational cost, and particles can be used only in the regions where they are really advantageous. This philosophy can be useful, for instance, in adaptive computations: a coarse finite element mesh can be used in the whole domain and, after an error estimation, some nodes can be removed and replaced by a suitable quantity of particles with no remeshing cost. The applicability of this mixed interpolation is shown in several examples.

Moreover, the mixed interpolation presented in chapter 4 can also be useful in the solution of convection dominated problems, such as the numerical simulation of flow in active

carbon canisters presented in appendix A. In this problem, there is a moving front in the solution that must be accurately interpolated. However, most of the realistic examples need 3D computations, and thus, the use of a uniform sufficiently dense mesh in the whole domain leads to a too large computational cost. If only finite elements are used, the mesh must be adapted in order to capture the advancing front. This implies a degradation in the solution (due to successive projections of the solution between meshes) and an increase in the computational cost. In fact, in 3D it is not easy to find a good mesh generator, which adapts the mesh to the prescribed densities of nodes. So, the mixed interpolation can be a good choice: a fixed coarse finite element mesh can be used in the whole domain, with a cloud of moving particles following the moving front in order to increase the spatial accuracy where it is needed. Thus, first of all it is important to study the behaviour of the EFG interpolation in convection dominated problems. Section 4.5.5, in chapter 4, shows how the mixed interpolation is used in the resolution of the stationary convection diffusion equation: the finite element solution can be easily improved using particles in the refinement process.

However, it is also necessary to carefully study the transient case. There are two important topics in the resolution of the transient convection-diffusion equation: (1) accurate transport of the unknown quantity is necessary, and thus, high-order time stepping schemes are needed, and (2) in the presence of boundary or internal layers, it is necessary to stabilize the solution in order to avoid oscillations. In chapter 5 the behaviour of high-order time stepping methods combined with mesh-free methods is studied. The EFG interpolation allows to easily increase the order of consistency and, thus, to formulate high-order schemes in space and time. Moreover, second derivatives of the EFG shape functions can be constructed with a low extra cost and are well defined, even for linear interpolation. Thus, consistent stabilization schemes can be considered without loss in the convergence rates. So, the use of mixed interpolations combining finite elements and mesh-free methods turns out to be a promising alternative in the resolution of transient convection dominated problems, such as the simulation of advancing fronts in active carbon canisters.

Chapter 2

State of the art in mesh-free methods

Although mesh-free methods were originated about twenty-five years ago, the research effort devoted to them until the last decade was miniscule. The starting point that seems to have the longest continuous history is the smooth particle hydrodynamic (SPH) method (Lucy 1977), see section 2.1.1. It was used in the modelization of astrophysical phenomena without boundaries such as exploding stars and dust clouds. Compared to other methods the rate of publications was very modest for many years; this is mainly reflected in the papers of Monaghan and coworkers (Monaghan 1982, Monaghan 1988). However, further research was needed in the estimation of the accuracy of the method.

Recently, there has been substantial improvement in these methods. For instance, references (Swengle, Hicks and Attaway 1995) and (Dyka 1994) have presented important advances in the study of its instabilities. In (Johnson and Beissel 1996) a method for improving strain calculations is presented. Reference (Liu, Jun and Zhang 1995) has proposed a correction function for kernels in both the discrete and continuous case. In fact, this approach can be seen as an extension of moving least-squares approximations (see section 2.1.2) to the continuous case. Reference (Nayroles, Touzot and Villon 1992) was evidently the first to use moving least square approximations in a Galerkin method and called it the diffuse element method (DEM). Reference (Belytschko, Lu and Gu 1994) refined and modified the method and called it EFG, element-free Galerkin. This class of methods is consistent and, in the forms proposed, quite stable, although substantially more expensive than SPH. Recently, the work in (Duarte and Oden 1996) and (Babuška and Melenk 1995) recognizes that the methods based on moving least squares are specific instances of partitions of unity. These references and (Liu et al. 1997) were also among the first to prove convergence of this class of methods. On a parallel path, reference (Vila 1999) has introduced a different mesh-free approximation specially suited for conservation laws: the renormalized Meshless Deriva-

tive (RMD) with turns out to give accurate approximation of derivatives in the framework of collocation approaches. Two other paths in the evolution of mesh-free methods have been the development of generalized finite difference methods, which can deal with arbitrary arrangements of nodes, and particle-in-cell methods. One of the early contributors to the former was (Perrone and Kao 1975), but (Liszka and Orkisz 1980) proposed a more robust method. Recently these methods have taken a character which closely resembles moving least squares and partitions of unity.

In recent papers the possibilities of mesh-free methods become apparent. The special issue of CMAME (1996) shows the ability of mesh-free methods to handle complex situations, such as impact problems, crack simulations or fluid dynamics. Reference (Bouillard and Suleau 1998) has applied a mesh-free formulation to acoustic problems with good results. In (Bonet and Lok 1999) a gradient correction is introduced in order to preserve the linear and angular momentum with applications to fluid dynamics. Another paper, (Bonet and Kulasegaram 2000), proposes the introduction of integration correction that improves accuracy with applications to metal forming simulation. Reference (Oñate and Idelsohn 1998) proposes a mesh-free method (finite point method) based on a weighted least-squares interpolation with point collocation with applications to convective transport and fluid flow. Moreover, recently several authors have proposed to use mixed interpolations combining finite elements and mesh-free methods, in order to take profit of the advantages of each method (see chapter 4).

This chapter is devoted to the description of the most common mesh-free methods and to the analysis of the differences and similarities between the different formulations. This chapter will also introduce the basic concepts and notation necessary for the developments in the following chapters. It is organized as follows. Section 2.1 presents the most popular mesh-free interpolations: a small introduction to the original SPH interpolation and its improved versions is presented in section 2.1.1, then section 2.1.2 describes the mesh-free interpolations based on a moving least-squares development, in both its continuous and discrete versions. Once the interpolation has been introduced, it can be used in the discretization of a boundary value problem. So, some concepts of collocation techniques and weak formulations are recalled in section 2.2; with special attention on the Galerkin formulation and, in particular, on the Element-Free Galerkin method. In fact, section 2.2.4 is devoted to the explanation of some implementation details of the EFG method, since all the developments in the following chapters will be done with this mesh-free method. However, as will be commented, generalization to other mesh-free methods is straightforward. Sec-

tion 2.2 also includes some remarks on how to impose essential boundary conditions with these methods, see section 2.2.3.

2.1 Interpolation in mesh-free methods

This section is devoted to describe the most common interpolations used in mesh-free methods. There can be considered two important families: interpolations based on Smooth Particle Hydrodynamic (SPH) and interpolations based on Moving Least Squares (MLS). As will be commented in section 2.2 the SPH interpolations are usually combined with collocation or point integration techniques, while the MLS interpolations are mostly combined with Galerkin formulations, and in some cases with collocation techniques.

2.1.1 Smooth Particle Hydrodynamic

The early SPH

The earliest mesh-free method is the SPH method (Lucy 1977). This method is based on a simple property of the Dirac delta function $\delta(x)$:

$$u(x) = \int \delta(x - y)u(y) \, dy,$$

where $u(x)$ is the function to be interpolated. The basic idea is to approximate this equation as

$$u(x) \simeq \tilde{u}^\rho(x) := \int C_\rho \phi\left(\frac{x - y}{\rho}\right) u(y) \, dy, \quad (2.1.1)$$

where ϕ is a positive, even and compact supported function, usually called *window function* or *weighting function*, and ρ is the so-called dilation parameter. The dilation parameter characterizes the support of $\phi(\frac{x}{\rho})$. C_ρ is a normalization constant such that

$$\int C_\rho \phi\left(\frac{x}{\rho}\right) \, dy = 1$$

and, therefore, $C_\rho \phi(\frac{x}{\rho})$ tends to $\delta(x)$ as ρ goes to zero. That is,

$$\lim_{\rho \rightarrow 0} \tilde{u}^\rho(x) = u(x).$$

In order to define a discrete interpolation, a numerical quadrature must be applied in (2.1.1):

$$u(x) \simeq \tilde{u}^\rho(x) \simeq u^\rho(x) := \sum_i C_\rho \phi\left(\frac{x - x_i}{\rho}\right) u(x_i) \omega_i \quad (2.1.2)$$

where x_i and ω_i are the points and weights of the numerical quadrature. Usually the quadrature points are called *particles*. Finally, the SPH mesh-free interpolation can be defined as

$$u(x) \simeq u^\rho(x) = \sum_i N_i(x)u(x_i),$$

with the interpolation base

$$N_i(x) = C_\rho \phi\left(\frac{x - x_i}{\rho}\right) \omega_i.$$

Remark 2.1.1. Note that usually $w^\rho(x_i) \neq u(x_i)$. That is, the shape functions do not verify the Kronecker delta property:

$$N_j(x_i) \neq \delta_{ij}.$$

This is common for all particle methods (see figure 2.5 for MLS interpolant) and thus, in some cases, specific techniques are needed in order to impose essential boundary conditions (see section 2.2).

Remark 2.1.2. The dilation parameter ρ characterizes the support of the interpolation functions $N_i(x)$. It plays a role similar to the element size in the finite element method. An h -refinement in finite elements can be produced in mesh-free methods decreasing the value of ρ , this usually implies an increase in the number of particles (see Remark 2.1.3).

Remark 2.1.3. There is an optimal value for the ratio between the dilation parameter ρ and the distance between particles h . Figure 2.1 shows that for a fixed distribution of particles, h constant, the dilation parameter must be large enough in order to avoid the aliasing effect (high frequencies are present in the approximated solution). On the other hand, a too large ρ will produce too large errors, due to the bad approximation of de Dirac delta function in (2.1.1). Thus, in a refinement process it is usual to maintain dilation parameter ρ proportional with the distance between particles h .

Window functions

The weighting function, or window function, may be defined in various manners. For 1D the most common options are

Cubic spline:

$$\phi_{1D}(x) = 2 \begin{cases} \frac{2}{3} + 4(|x| - 1)x^2 & |x| \leq 0.5 \\ \frac{4}{3}(1 - |x|)^3 & 0.5 \leq |x| \leq 1 \\ 0 & 1 \leq |x|, \end{cases} \quad (2.1.3)$$

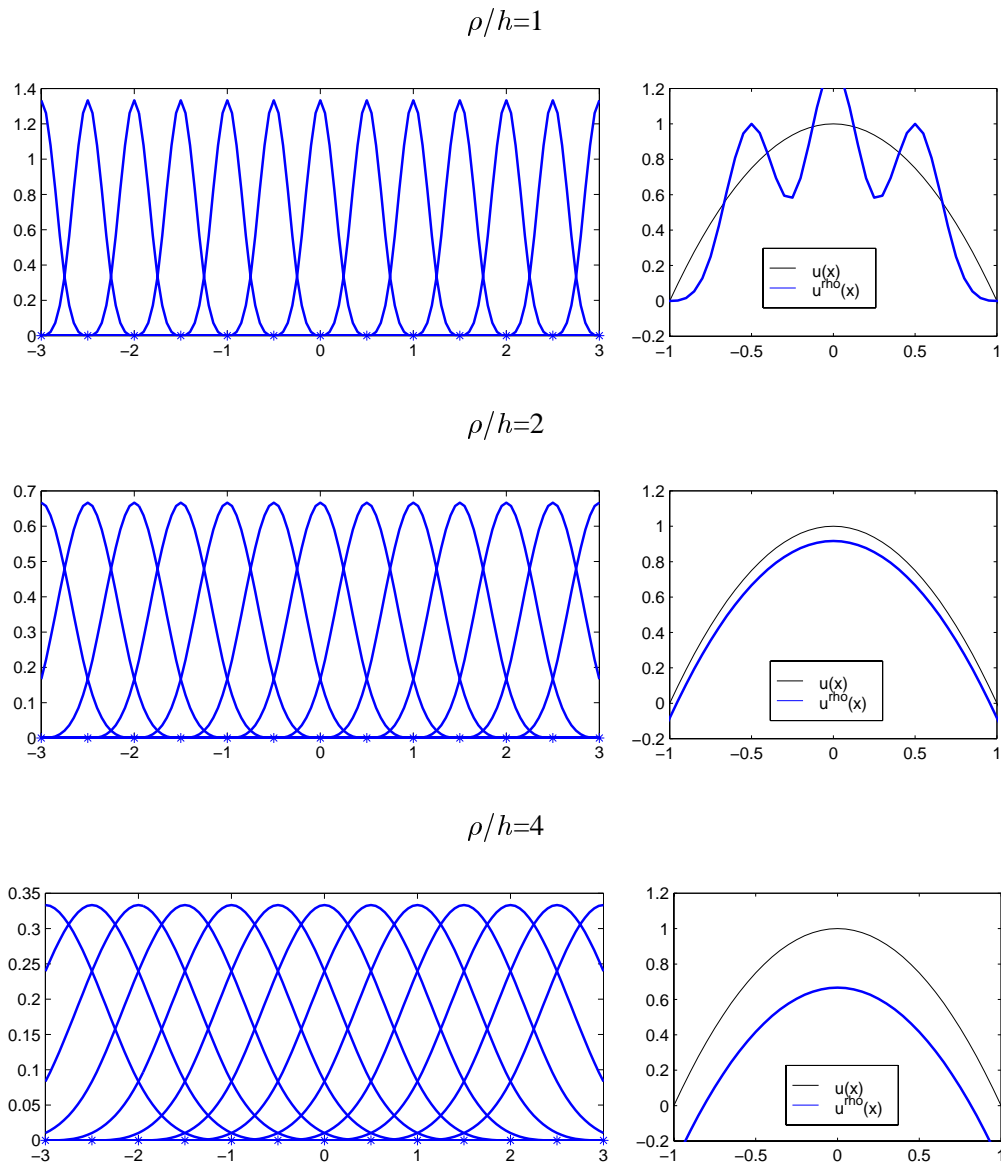


Figure 2.1: SPH interpolation functions and approximation of $u(x) = 1 - x^2$ with cubic spline window function, distance between particles $h = 0.5$ and quadrature weights $\omega_i = h$, for $\rho/h = 1, 2, 4$.

Gaussian:

$$\phi_{1D}(x) = \begin{cases} \frac{e^{-9x^2} - e^{-9}}{1 - e^{-9}} & |x| \leq 1 \\ 0 & |x| \geq 1. \end{cases} \quad (2.1.4)$$

The definition of the window function can be easily extended to higher dimensions. For example, in 2D the most common extensions are

Circular supported window function:

$$\phi(\mathbf{x}) = \phi_{1D}(\|\mathbf{x}\|),$$

Rectangular supported window function:

$$\phi(\mathbf{x}) = \phi_{1D}(|x_1|) \phi_{1D}(|x_2|)$$

where $\mathbf{x} = (x_1, x_2)$ and $\|\mathbf{x}\| = \sqrt{x_1^2 + x_2^2}$.

Remark 2.1.4. For simplicity, in the following, x (without boldface) can denote a point in \mathbb{R} or in \mathbb{R}^n , there is not an explicit distinction.

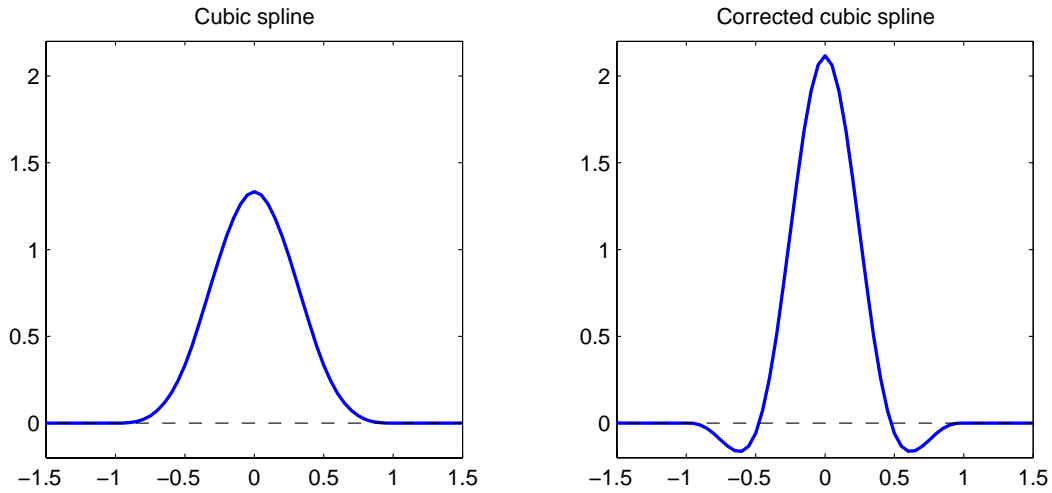


Figure 2.2: Cubic spline and corrected window function for polynomials of degree 2.

Remark 2.1.5 (Design of the window function). In the context of the continuous SPH interpolation (2.1.1), a window function ϕ can be easily modified to exactly reproduce a polynomial space \mathcal{P} in \mathbb{R} , i.e.

$$p(x) = \int C_\rho \phi\left(\frac{x-y}{\rho}\right) p(y) dy, \quad \forall p \in \mathcal{P}.$$

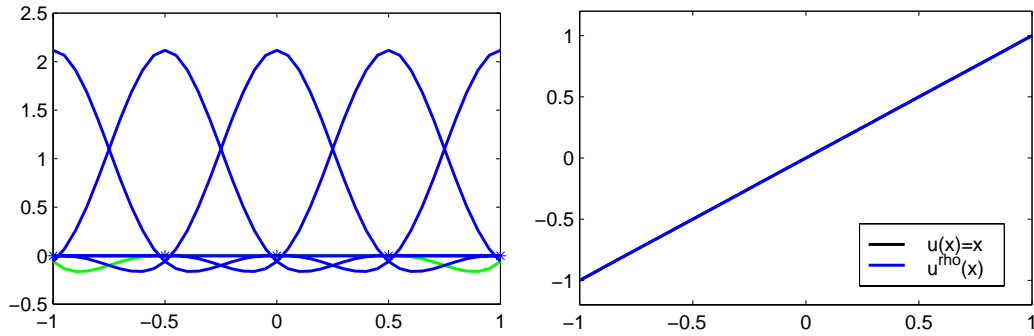


Figure 2.3: Modified cubic splines and particles, $h = 0.5$, and SPH discrete approximation for $u(x) = x$ with $\rho/h = 2$ in a “not bounded domain”.

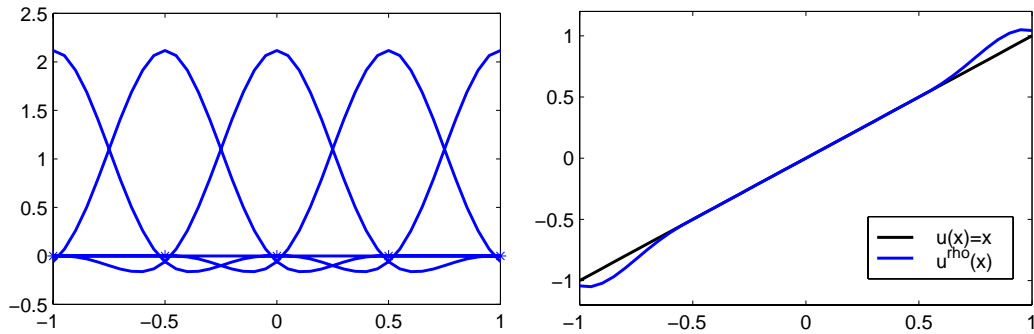


Figure 2.4: Modified cubic splines and particles, $h = 0.5$, and SPH discrete approximation for $u(x) = x$ with $\rho/h = 2$ in a bounded domain.

For example, the window function defined as

$$\tilde{\phi}(x) = \left[\frac{27}{17} - \frac{120}{17}x^2 \right] \phi(x), \quad (2.1.5)$$

where $\phi(x)$ is the cubic spline, reproduces the second degree polynomial base $\{1, x, x^2\}$. Figure 2.2 shows the cubic spline (2.1.3) and the corrected window function (2.1.5), see (Liu, Chen, Jun, Chen, Belytschko, Pan, Uras and Chang 1996) for details. However, the design of the window function is not so easy in the presence of boundaries or in the case of a discrete interpolation with no uniform distribution of particles (see section 2.1.2). Figure 2.3 shows the corrected cubic spline window functions associated to a uniform distribution of particles, with distance $h = 0.5$ between particles and $\rho = 2h$, and the discrete SPH approximation (2.1.2) of $u(x) = x$, for uniform weights $\omega_i = h$. The particles out from

$[-1, 1]$ are also considered in the interpolation, as in a not bounded domain (the corresponding translated window functions are depicted with green color). The linear monomial $u(x) = x$ is exactly interpolated. However, in a bounded domain, the interpolation is not so good near the boundaries when only the particles in the domain ($[-1, 1]$ in this example) are considered, see Figure 2.4.

Remark 2.1.6 (Consistency). If the interpolation reproduces exactly a basis of the polynomials of degree less or equal to m then the approximation is said to have m -order consistency.

Correcting the SPH method

The SPH interpolation can be used in the resolution of a PDE problem, usually through a collocation technique or point integration approaches (see (Vila 1999), (Bonet and Lok 1999) and section 2.2.1). Thus, it is necessary to compute accurate approximations of the derivatives. The original SPH method usually provides not so accurate approximations, and thus, it is necessary to improve the interpolation, or its derivatives, in some way.

Vila proposes a new approximation for the derivatives of the interpolation: the Renormalized Meshless Derivative (RMD), see (Vila 1999). The derivatives of a function u can be approximated as the derivatives of the SPH approximation (2.1.2)

$$\nabla u(x) \simeq \nabla u^\rho(x) = \sum_i C_\rho \nabla \left[\phi \left(\frac{x - x_i}{\rho} \right) \right] u(x_i) \omega_i.$$

However, this approximation is not accurate enough. The basic idea of the RMD approximation is to define a corrected derivative

$$D^\rho u(x) := \sum_i \mathbf{B} C_\rho \nabla \left[\phi \left(\frac{x - x_i}{\rho} \right) \right] u(x_i) \omega_i, \quad (2.1.6)$$

where the correction matrix \mathbf{B} is chosen such that $\nabla u(x) = D^\rho u(x)$ for all linear polynomials. In fact, in order to obtain a consistent and convergent method, this other symmetrized approximation for the derivatives is defined

$$D_\zeta^\rho u(x) := D^\rho u(x) - u(x) D^\rho 1(x), \quad (2.1.7)$$

where, by definition (2.1.6),

$$D^\rho 1(x) = \sum_i \mathbf{B}(x) C_\rho \nabla \left[\phi \left(\frac{x - x_i}{\rho} \right) \right] \omega_i.$$

Note that (2.1.7) interpolates exactly the derivatives when $u(x)$ is constant, and thus, the consistency condition $\nabla u(x) = D^\rho u(x)$ must be imposed only for linear monomials. This

condition leads to

$$\mathbf{B}(x) = \left[\sum_j x_j \nabla^T \left[\phi \left(\frac{x - x_i}{\rho} \right) \right] \omega_j \right]^{-1}.$$

If the ratio between the dilation parameter ρ and the distance between particles remains constant, there are *a priori* error bounds for the RMD, $D_S^\rho u$, similar to the linear finite element ones, where ρ plays the role of the element size in finite elements.

There are many other possibilities for the correction of the SPH method. Bonet and coworkers have presented corrected SPH methods in different situations. For each different problem, the correction of the SPH method is designed in order to obtain nice properties of the approximation. For example, in (Bonet and Lok 1999) a correction of the window function, as in the RKPM method (see section 2.1.2), and a correction of the gradient are combined in order to preserve angular momentum, with applications to free surface flow problems. The approximation of the velocity $u(x)$ is defined as

$$u^\rho(x) = \sum_i u(x_i) \tilde{\phi}_i(x) \omega_i$$

where the kernel functions $\tilde{\phi}_i(x)$ can be defined to verify the 0-order consistency condition (see remark 2.1.6), that is, to exactly interpolate constants,

$$\tilde{\phi}_i(x) = \frac{\phi \left(\frac{x - x_i}{\rho} \right)}{\sum_j \phi \left(\frac{x - x_j}{\rho} \right)},$$

where $\phi(x)$ is the window function. This approximation can be seen as a particular case of the RKPM interpolation (see section 2.1.2). In fact, in some applications the 1-order consistent kernel function is also considered. The derivatives can be computed as usually

$$\nabla u^\rho(x) = \sum_i u(x_i) \nabla \tilde{\phi}_i(x) \omega_i.$$

This approximation is able to preserve linear momentum, however, it usually fails to preserve angular momentum. In order to overcome this shortcoming a corrected gradient is defined:

$$\tilde{\nabla} u^\rho(x) = \mathbf{L}(x) \nabla u^\rho(x),$$

where the matrix $\mathbf{L}(x)$ is obtained after imposing preservation of angular momentum,

$$\mathbf{L}(x) = \left[\sum_j x_j \nabla^T \left[\tilde{\phi}_i(x) \right] \omega_j \right]^{-1}.$$

Note the similarities between the corrected gradient and the Renormalized Meshless Derivative. The definition of matrix $\mathbf{L}(x)$ coincides with the definition of matrix $\mathbf{B}(x)$, after substitution of the window function ϕ by the kernel function $\tilde{\phi}$. The most important difference is that in the RMD approach 0-order consistency is obtained through the definition of the symmetrized gradient (2.1.6), and with the corrected gradient $\tilde{\nabla}u^\rho$ the 0-order consistency is obtained through the kernel function $\tilde{\phi}$.

In (Bonet and Kulasegaram 2000) a correction of the window function and a integration corrected vector for the gradients is used in the resolution of problems of metal forming simulations. The approximation is used to discretize a Galerkin weak form with particle integration (see section 2.2.2), and thus, the gradient must be evaluated only at the particles. However, usually the particle integration is not accurate enough and the approximation fails to pass the patch test. In order to obtain a consistent approximation a corrected gradient is defined. At every particle x_k the corrected gradient is computed as

$$\tilde{\nabla}u^\rho(x_k) = \nabla u^\rho(x_k) + \gamma_k [u]_k$$

where $\gamma = (\gamma_k)_k$ is the correction vector and where the bracket $[u]_k$ is defined as $[u]_k = u(x_k) - u^\rho(x_k)$. After imposing the patch test a linear system of equations for γ is obtained, with dimension equal to the number of particles. That is, a linear system of equations must be solved to obtain the correction vector and define the derivatives of the approximation; after that, the approximation of u and its derivatives are used to solve the boundary value problem.

2.1.2 Moving Least Squares interpolants

As in the corrected SPH methods commented in the previous section, the interpolations based on a Moving Least Squares (MLS) development can be considered as an improvement of the SPH method. However, the MLS interpolations are usually used to discretize a Galerkin formulation, and thus, accuracy and consistency in both the interpolation and its derivatives are needed in all the domain.

Continuous Moving Least Squares

The objective of the Moving Least Squares (MLS) approach is to obtain an interpolation similar to the SPH one (2.1.1), with high accuracy even in a bounded domain. Let us consider a bounded, or unbounded, domain Ω . The basic idea of the MLS approach is to approximate $u(x)$, at a given point x , through a polynomial least-squares fitting of u in a

neighbourhood of x . That is, fixed $x \in \Omega$, for z near x , $u(z)$ can be approximated with a polynomial expression

$$u(z) \simeq \tilde{u}_x^\rho(z) = \mathbf{P}^T(z)\mathbf{c}(x) \quad (2.1.8)$$

where $\mathbf{P}(z) = \{p_0(z), p_1(z), \dots, p_l(z)\}^T$ is a complete polynomial basis, and the vector $\mathbf{c}(x)$ is obtained through least-squares fitting, with the scalar product

$$\langle f, g \rangle_x = \int_{\Omega} f(y)g(y)\phi\left(\frac{x-y}{\rho}\right) dy. \quad (2.1.9)$$

Remark 2.1.7. Note that, with the weighting function ϕ , the scalar product is centred at the point x and scaled with the dilation parameter ρ . In fact, the integration is done in a neighbourhood of radius ρ centred at x , that is, in the support of $\phi\left(\frac{x-y}{\rho}\right)$.

Remark 2.1.8 (Polynomial space). In one dimension, it is usual that $\mathcal{P}_l(x)$ coincides with the monomials x^i , and, in this particular case, $l = m$. For larger spatial dimensions two types of polynomial spaces are usually chosen: the set of polynomials, \mathcal{P}_m , of total degree $\leq m$, and the set of polynomials, \mathcal{Q}_m , of degree $\leq m$ in each variable. Both include a complete basis of the subspace of polynomials of degree m . This, in fact, characterizes the *a priori* convergence rate (Liu et al. 1997).

The vector $\mathbf{c}(x)$ is the solution of the linear system of equations

$$\mathbf{M}(x)\mathbf{c}(x) = \langle \mathbf{P}, u \rangle_x \quad (2.1.10)$$

with the Gram matrix

$$\mathbf{M}(x) = \int_{\Omega} \mathbf{P}(y)\mathbf{P}^T(y)\phi\left(\frac{x-y}{\rho}\right) dy. \quad (2.1.11)$$

After substitution of the solution of (2.1.10)

$$\mathbf{c}(x) = \mathbf{M}^{-1}(x) \langle \mathbf{P}, u \rangle_x$$

in (2.1.8), the least-squares approximation of u in a neighbourhood of x is obtained:

$$u(z) \simeq \tilde{u}_x^\rho(z) = \mathbf{P}^T(z)\mathbf{M}^{-1}(x) \int_{\Omega} u(y)\mathbf{P}(y)\phi\left(\frac{x-y}{\rho}\right) dy. \quad (2.1.12)$$

Particularization of (2.1.12) at $z = x$ leads to the MLS approximation of $u(x)$

$$u(x) \simeq \tilde{u}^\rho(x) := \tilde{u}_x^\rho(x) = \int_{\Omega} u(y)\mathbf{P}^T(x)\mathbf{M}^{-1}(x)\mathbf{P}(y)\phi\left(\frac{x-y}{\rho}\right) dy. \quad (2.1.13)$$

Equation (2.1.13) can be rewritten as

$$u(x) \simeq \tilde{u}^\rho(x) = \int_{\Omega} C_\rho(x, y)\phi\left(\frac{x-y}{\rho}\right) u(y) dy,$$

which is similar to the SPH approximation (2.1.1), with the scalar correction term

$$C_\rho(x, y) := \mathbf{P}^T(x)\mathbf{M}^{-1}(x)\mathbf{P}(y).$$

The function defined by the product of the correction and the window function ϕ ,

$$\tilde{\phi}_y(x) := C_\rho(x, y)\phi\left(\frac{x-y}{\rho}\right),$$

is usually called *kernel function*. The new correction term depends on the point x and the integration variable y , and provides an accurate approximation even in the presence of boundaries, see (Liu, Chen, Jun, Chen, Belytschko, Pan, Uras and Chang 1996) for more details. In fact, the approximation verifies the following consistency property:

Proposition 2.1.1 (Consistency/reproducibility property). *The definition of the correction term allows the MLS interpolation to exactly reproduce all the polynomials in \mathbf{P} . That is,*

$$\mathbf{P}(x) = \tilde{\mathbf{P}}^\rho(x) := \int_{\Omega} \mathbf{P}(y) [\mathbf{P}^T(x)\mathbf{M}^{-1}(x)] \mathbf{P}(y)\phi\left(\frac{x-y}{\rho}\right) dy.$$

(Recall that if \mathbf{P} contains a basis of the polynomials of degree less or equal to m then the approximation is said to have m -order consistency)

proof: Rearranging terms, and taking into account definition (2.1.11),

$$\tilde{\mathbf{P}}^\rho(x) = \underbrace{\left[\int_{\Omega} \mathbf{P}(y)\mathbf{P}^T(y)\phi\left(\frac{x-y}{\rho}\right) dy \right]}_{\mathbf{M}(x)} \mathbf{M}^{-1}(x)\mathbf{P}(x) = \mathbf{P}(x)$$

•

Reproducing Kernel Particle Method interpolation

Application of a numerical quadrature in (2.1.13) leads to the RKPM interpolation

$$u(x) \simeq \tilde{u}^\rho(x) \simeq u^\rho(x) := \sum_i u(x_i)\mathbf{P}^T(x)\mathbf{M}^{-1}(x)\mathbf{P}(x_i)\phi\left(\frac{x-x_i}{\rho}\right)\omega_i,$$

where x_i and ω_i are integration points (particles) and weights, respectively. This interpolation can be written as

$$u(x) \simeq u^\rho(x) = \sum_i u(x_i)N_i(x) \tag{2.1.14}$$

where the basis of interpolation functions is defined by

$$N_i(x) = \mathbf{P}^T(x)\mathbf{M}^{-1}(x)\mathbf{P}(x_i)\phi\left(\frac{x-x_i}{\rho}\right)\omega_i. \tag{2.1.15}$$

Remark 2.1.9. In order to preserve the consistency/reproducibility property, the matrix \mathbf{M} defined in (2.1.11) must be computed with the same quadrature used for the discretization of (2.1.13), see (Chen, Pan, Wu and Liu 1996) for details. That is, the matrix $\mathbf{M}(x)$ must be computed as

$$\mathbf{M}(x) = \sum_j \mathbf{P}(x_j) \mathbf{P}^T(x_j) \phi\left(\frac{x - x_j}{\rho}\right) \omega_i. \quad (2.1.16)$$

Remark 2.1.10. The sums in (2.1.14) and (2.1.16) only involve the indices j such that $\phi\left(\frac{x - x_j}{\rho}\right) \neq 0$, that is, particles x_j in a neighbouring of x . Thus, equations (2.1.14) and (2.1.16) can be rewritten as

$$u(x) \simeq u^\rho(x) = \sum_{i \in I_x^\rho} u(x_i) N_i(x)$$

and

$$\mathbf{M}(x) = \sum_{j \in I_x^\rho} \mathbf{P}(x_j) \mathbf{P}^T(x_j) \phi\left(\frac{x - x_j}{\rho}\right) \omega_i, \quad (2.1.17)$$

where the set of neighbouring particles is defined by the indices in

$$I_x^\rho := \{j \text{ such that } |x_j - x| \leq \rho\}. \quad (2.1.18)$$

Remark 2.1.11. The matrix $\mathbf{M}(x)$ in (2.1.17) must be regular at every point x in the domain. In (Liu et al. 1997) there is a discussion of the necessary conditions. In fact, this matrix can be viewed, see (Huerta and Fernández-Méndez 2000), as a Gram matrix defined with a discrete scalar product

$$\langle f, g \rangle_x = \sum_{j \in I_x^\rho} f(x_j) g(x_j) \phi\left(\frac{x - x_j}{\rho}\right) \omega_i.$$

If this scalar product is degenerated $\mathbf{M}(x)$ is singular. The regularity of $\mathbf{M}(x)$ is ensured by a sufficient amount of particles in the neighbourhood of every point x and located to avoid degenerated patterns, that is,

(i) $\text{card } I_x^\rho \geq l + 1$.

(ii) $\nexists F \in \langle p_0, p_1, \dots, p_l \rangle \setminus \{0\}$ such that $\forall i \in I_x^\rho, F(x_i) = 0$.

The second condition is easily verified. For instance, for $m = 1$ (linear interpolation) the particles cannot lay in the same straight line or plane for, respectively, 2D and 3D. In 1D, for any value of m , it suffices that different particles do not have the same position. Under these conditions one can compute the vector $\mathbf{P}^T(x) \mathbf{M}^{-1}(x)$ at each point and thus determine the shape functions, $N_j(x)$.

Discrete Moving Least Squares: EFG interpolation

The MLS development can be performed with a discrete formulation. As in the continuous case the idea is to approximate $u(x)$, at a given point x , through a polynomial least-squares fitting of u in a neighbourhood of x . That is, fixed $x \in \Omega$, for z near x , $u(z)$ is approximated with the polynomial expression

$$u(z) \simeq u_x^\rho(z) = \mathbf{P}^T(z)\mathbf{c}(x). \quad (2.1.19)$$

In the framework of the Element Free Galerkin method, the vector $\mathbf{c}(x)$ is obtained through a least-squares fitting with the discrete scalar product

$$\langle f, g \rangle_x = \sum_{i \in I_x^\rho} f(x_i)g(x_i)\phi\left(\frac{x-x_i}{\rho}\right). \quad (2.1.20)$$

where, I_x^ρ is the set of indices of neighbouring particles defined in (2.1.18). That is, $\mathbf{c}(x)$ is solution of the linear system of equations

$$\mathbf{M}(x)\mathbf{c}(x) = \langle \mathbf{P}, u \rangle_x \quad (2.1.21)$$

with the Gram matrix

$$\mathbf{M}(x) = \sum_{j \in I_x^\rho} \mathbf{P}(x_j)\mathbf{P}^T(x_j)\phi\left(\frac{x-x_j}{\rho}\right). \quad (2.1.22)$$

After substitution of the solution of (2.1.21) in (2.1.19), the least-squares approximation of u in a neighbourhood of x is obtained:

$$u(z) \simeq u_x^\rho(z) = \mathbf{P}^T(z)\mathbf{M}^{-1}(x) \sum_i u(x_i)\mathbf{P}(x_i)\phi\left(\frac{x-x_i}{\rho}\right). \quad (2.1.23)$$

Particularization of (2.1.23) at $z = x$ leads to the discrete MLS approximation of $u(x)$

$$u(x) \simeq u^\rho(x) := u_x^\rho(x) = \sum_i u(x_i)\mathbf{P}^T(x)\mathbf{M}^{-1}(x)\mathbf{P}(x_i)\phi\left(\frac{x-x_i}{\rho}\right). \quad (2.1.24)$$

This interpolation can be written as

$$u(x) \simeq u^\rho(x) = \sum_i u(x_i)N_i(x)$$

where the basis of interpolation functions is defined by

$$N_i(x) = \mathbf{P}^T(x)\mathbf{M}^{-1}(x)\mathbf{P}(x_i)\phi\left(\frac{x-x_i}{\rho}\right). \quad (2.1.25)$$

with the matrix \mathbf{M} defined in (2.1.22).

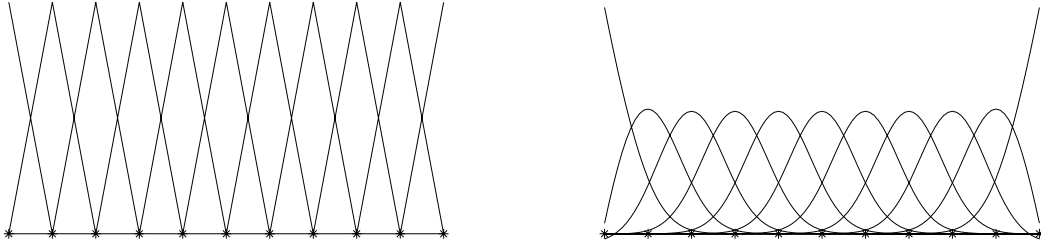


Figure 2.5: Interpolation functions with $\rho/h \simeq 1$ (similar to finite elements) and $\rho/h = 2.6$, with cubic spline and linear consistency.

Remark 2.1.12. Note that the EFG interpolation functions defined by (2.1.25) and (2.1.22), can be seen as a particular case of the RKPM interpolation functions defined by (2.1.15) and (2.1.17), taking the weights of the numerical quadrature $\omega_i = 1$ for all particles.

Remark 2.1.13. The interpolation is characterized by the order of consistency required, *i.e.* the basis of polynomials employed \mathbf{P} , and by the ratio between the dilation parameter and the particle distance, ρ/h . In fact, the bandwidth of the stiffness matrix increases with the ratio ρ/h (more particles lie inside the circle of radius ρ), see for instance Figure 2.5. Note that, for linear consistency, when ρ/h goes to 1, the linear finite element shape functions are recovered.

Remark 2.1.14 (Convergence). Liu, Li and Belytschko (Liu et al. 1997) proved convergence of the RKPM and, in particular, of EFG. The *a priori* error bound is very similar to the bound in finite elements. The parameter ρ plays the role of h , and m (the order of consistency) plays the role of the degree of the interpolation polynomials in the finite element mesh. Convergence properties depend on m and ρ . They do not depend on the distance between particles because usually this distance is proportional to ρ , *i.e.* the ratio between the particle distance over the dilation parameter is of order one, see (Liu et al. 1997).

Remark 2.1.15 (Continuity). If the weight function ϕ is C^k then the RKPM shape functions, and in particular the EFG shape functions, are C^k , see (Liu et al. 1997). Thus, if the cubic spline is used for the window function, as can be seen in figures 2.6 and 2.7, first and second derivatives of the shape functions are well defined in all the domain, even with linear consistency.

Consistency of the EFG interpolation

The expression of the EFG shape functions can be derived in a different way, which will ensure the consistency properties of the approximation. Consider a set of particles x_i and a

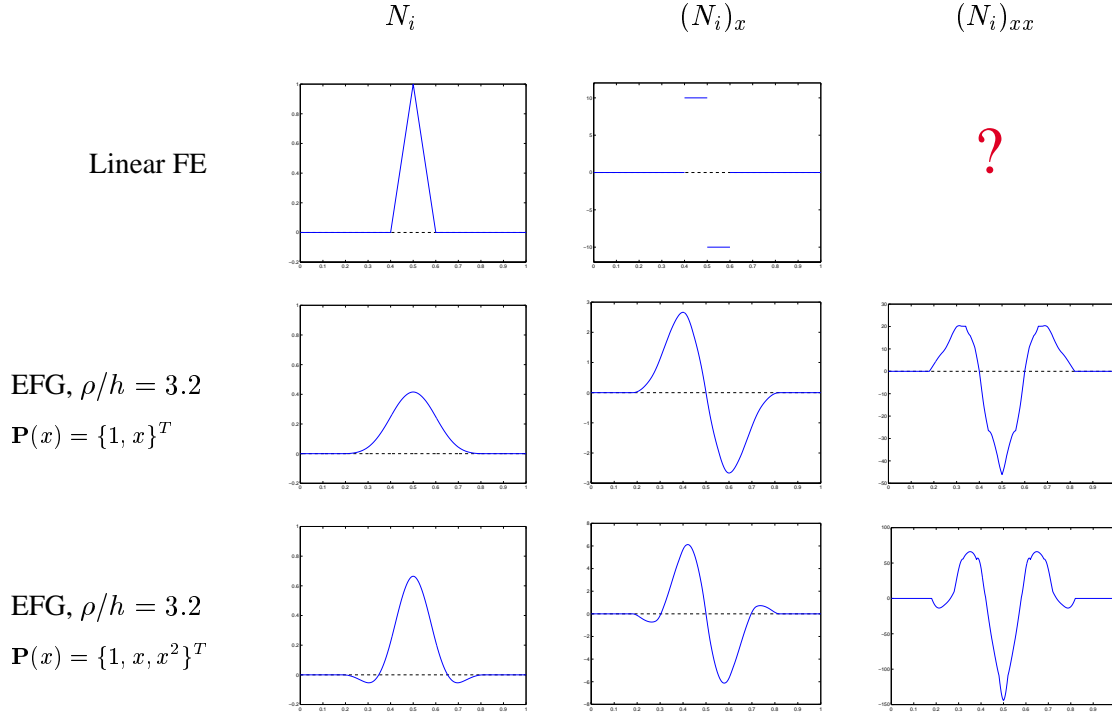


Figure 2.6: Shape function and derivatives for linear finite elements and the EFG interpolation.

complete polynomial base $\mathbf{P}(x)$. Let us assume an interpolation of the form

$$u(x) \simeq \sum_i u(x_i) N_i(x), \quad (2.1.26)$$

with interpolation functions defined as

$$N_i(x) = \boldsymbol{\alpha}^T(x) \mathbf{P}(x_i) \phi\left(\frac{x - x_i}{\rho}\right). \quad (2.1.27)$$

Now the vector $\boldsymbol{\alpha}(x)$ in \mathbb{R}^{l+1} is determined imposing the reproducibility/consistency condition. The reproducibility condition imposes that the interpolation proposed in (2.1.26) is exact for all the polynomials in \mathbf{P} , i.e.

$$\mathbf{P}(x) = \sum_j \mathbf{P}(x_j) \mathbf{N}_j(x). \quad (2.1.28)$$

After substitution of (2.1.27) in (2.1.28), the linear system of equations that determines $\boldsymbol{\alpha}(x)$ is obtained:

$$\mathbf{M}(x) \boldsymbol{\alpha}(x) = \mathbf{P}(x). \quad (2.1.29)$$

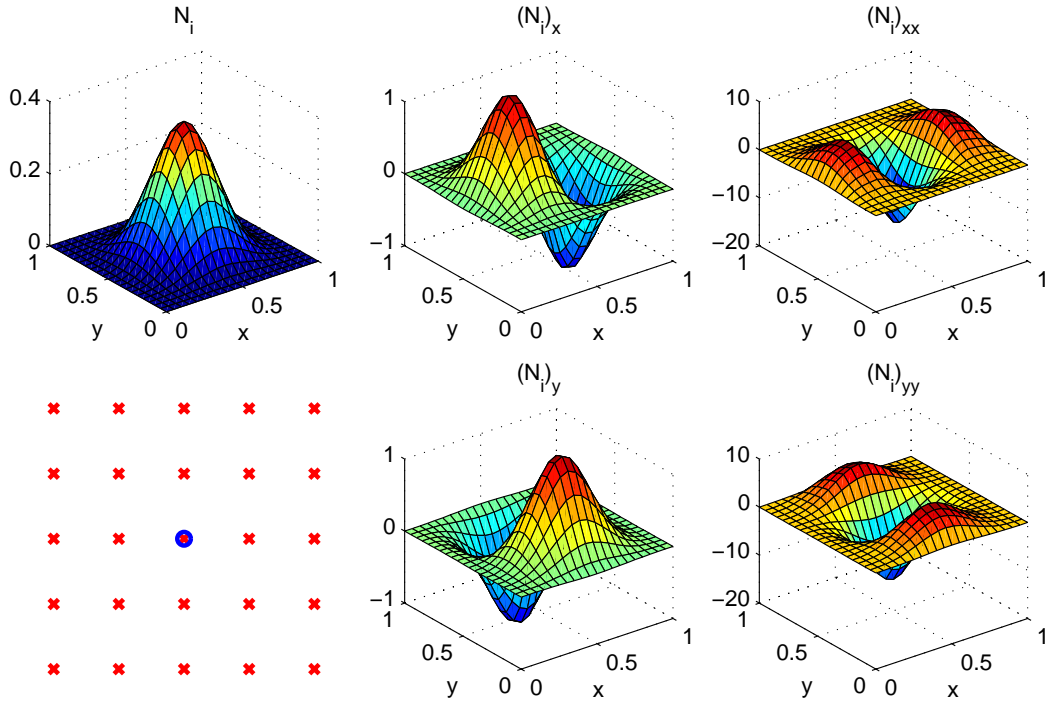


Figure 2.7: Distribution of particles, EFG interpolation function and derivatives, with $\rho/h \simeq 2.2$ with circular supported cubic spline and linear consistency.

That is,

$$\boldsymbol{\alpha}(x) = \mathbf{M}^{-1}(x)\mathbf{P}(x), \quad (2.1.30)$$

where $\mathbf{M}(x)$ is the same Gram matrix defined in (2.1.22). Finally, the approximation functions N_i in (2.1.26) are defined by (2.1.27) with (2.1.30) and (2.1.22). Note that after substitution of (2.1.30) in (2.1.27) the expression (2.1.25) for the EFG interpolation functions is recovered, and consistency is ensured by construction.

Section 2.2.4 is devoted to some implementation details of the EFG method: some details on the computation of derivatives are recalled.

EFG centred and scaled approach

For computational purposes, it is usual and preferable to centre in x_j and scale with ρ also the polynomials involved in the definition of the EFG interpolation functions, see (Liu et al. 1997) or (Huerta and Fernández-Méndez 2000). Thus, another expression for the EFG shape functions is employed:

$$\mathbf{N}_i(x) = \boldsymbol{\alpha}^T(x) \mathbf{P}\left(\frac{x - x_i}{\rho}\right) \phi\left(\frac{x - x_i}{\rho}\right), \quad (2.1.31)$$

which is similar to (2.1.27). The consistency condition becomes in this case:

$$\mathbf{P}(0) = \sum_i \mathbf{P}\left(\frac{x-x_i}{\rho}\right) \mathbf{N}_i(x), \quad (2.1.32)$$

which is equivalent to condition (2.1.28) when ρ is constant everywhere (see Remark 2.1.16 for non constant ρ). After substitution of (2.1.31) in (2.1.32) the linear system of equations that determines $\boldsymbol{\alpha}(x)$ is obtained:

$$\mathbf{M}(x) \boldsymbol{\alpha}(x) = \mathbf{P}(0), \quad (2.1.33)$$

with

$$\mathbf{M}(x) = \sum_j \mathbf{P}\left(\frac{x-x_j}{\rho}\right) \mathbf{P}^T\left(\frac{x-x_j}{\rho}\right) \phi\left(\frac{x-x_j}{\rho}\right). \quad (2.1.34)$$

Remark 2.1.16. The consistency conditions (2.1.28) and (2.1.32) are equivalent if the dilation parameter ρ is constant. When the dilation parameter varies at each particle another definition of the shape functions is recommended

$$N_j(x) = \boldsymbol{\alpha}^T(x) \mathbf{P}\left(\frac{x-x_j}{\rho}\right) \phi\left(\frac{x-x_j}{\rho_j}\right),$$

where ρ_j is the dilation parameter associated to particle x_j , and a constant ρ is employed in the scaling of the polynomials \mathbf{P} . Note that expression (2.1.31) is not directly generalized. The constant value ρ is typically chosen as the mean value of all the ρ_j . The consistency condition in this case is also (2.1.32). It also imposes the reproducibility of the polynomials in \mathbf{P} .

This centred expression for the EFG shape functions can also be obtained through a discrete Moving Least-Squares development with the discrete centred scalar product

$$\langle f, g \rangle_x = \sum_{j \in I_x^p} f\left(\frac{x-x_j}{\rho}\right) g\left(\frac{x-x_j}{\rho}\right) \phi\left(\frac{x-x_j}{\rho}\right). \quad (2.1.35)$$

The MLS development in this case is as follows: fixed x , for z near x , u is approximated as

$$u(z) \simeq u_x^\rho(x) = \mathbf{P}^T\left(\frac{z-x}{\rho}\right) \mathbf{c}(x) \quad (2.1.36)$$

where \mathbf{c} is obtained, as usual, through a least-squares fitting with the discrete centred scalar product (2.1.35).

Remark 2.1.17. With the centred MLS development and a proper definition of the polynomial space, \mathbf{P} , the coefficients in $\mathbf{c}(x)$ can be reinterpreted as approximations of u and

its derivatives at the fixed point x . For example, in 1D with consistency of order two, $\mathbf{P}(x) = \{1, \rho x, \frac{(\rho x)^2}{2}\}$ and (2.1.36) can be written as

$$u(z) \simeq u_x^\rho(x) = c_0(x) + c_1(x)(z - x) + c_2(x)(z - x)^2. \quad (2.1.37)$$

So, by derivation with respect to z and replacing z by x ,

$$u(x) \simeq c_0(x), \quad u'(x) \simeq c_1(x) \quad \text{and} \quad u''(x) \simeq c_2(x).$$

In fact, this centred approach corresponds with the Diffuse Element Method interpolation used, for instance, in (Breitkopf, Rassinoux and Villon 2001). Moreover, the Generalized Finite Difference interpolation or Meshless Finite Difference method, see (Orkisz 1998), coincides also with this MLS development. The only one difference between the GFD interpolation and the EFG centred interpolation is the definition of the set of neighbouring particles I_x^ρ .

Partition of the unity methods

The set of MLS interpolation functions can be seen as a partition of unity: the interpolation verifies, at least, the 0-order consistency condition (reproducibility of the constant polynomial $p(x) = 1$)

$$\sum_i N_i \cdot 1 = 1.$$

This viewpoint leads to several new approximations for mesh-free methods. Based on the idea of the Partition of the Unity Finite Element Method in (Babuška and Melenk 1995), Duarte and Oden (Duarte and Oden 1996) use the concept of partition of unity in a more general manner by constructing it from the MLS interpolation functions with consistency of order $k \geq 1$. They called their method *h-p clouds*. The proposed approximation was

$$u(x) \simeq u^\rho(x) = \sum_i N_i(x)u_i + \sum_i \sum_{I=1}^{n_i} b_{iI} [N_i(x)q_{iI}(x)],$$

where $N_i(x)$ are the MLS interpolation functions, q_{iI} are n_i polynomials of degree greater than k associated to each particle x_i , and u_i, b_{iI} are coefficients to determine. Note that the polynomials $q_{iI}(x)$ increase the order of the interpolation space. These polynomials can be different from particle to particle, thus facilitating the hp-adaptivity.

Remark 2.1.18. As commented in (Belytschko, Krongauz, Organ, Fleming and Krysl 1996), the concept of an extrinsic base, $q_{iI}(x)$, is essential for obtaining p -adaptivity. In MLS approximations, the intrinsic base \mathbf{P} cannot vary from particle to particle without introducing a discontinuity.

2.2 Implementation details

All the interpolation functions described in section 2.1 can be used in the resolution of a PDE boundary value problem. Usually SPH methods are combined with a collocation or point integration technique, while the interpolations based on a MLS development are usually combined with a Galerkin formulation.

In the following sections some concepts of collocation techniques and Galerkin formulations are recalled; with special attention on the Galerkin formulations and, in particular, on the Element Free Galerkin method. The model boundary value problem

$$\Delta u - u = -f \quad \text{in } \Omega \quad (2.2.1)$$

$$u = u_D \quad \text{on } \Gamma_D \quad (2.2.2)$$

$$\frac{\partial u}{\partial \mathbf{n}} = q_N \quad \text{on } \Gamma_N \quad (2.2.3)$$

is considered, where Δ is the Laplace operator in 2D, $\Delta = \frac{\partial^2}{\partial x^2} + \frac{\partial^2}{\partial y^2}$, \mathbf{n} is the unitary outward normal vector in $\partial\Omega$, $\frac{\partial}{\partial \mathbf{n}} = n_1 \frac{\partial}{\partial x} + n_2 \frac{\partial}{\partial y}$, $\bar{\Gamma}_D \cup \bar{\Gamma}_N = \partial\Omega$, and f , u_D and q_N are known.

2.2.1 Collocation methods

Consider an approximation, based on a set of particles $\{x_i\}$, of the form

$$u(x) \simeq u^p(x) = \sum_i u_i N_i(x).$$

The shape functions $N_i(x)$ can be SPH shape functions (section 2.1.1), or MLS shape functions (section 2.1.2), and u_i are coefficients to be determined.

In collocation methods, see (Oñate and Idelsohn 1998), the PDE (2.2.1) is imposed at each particle in the interior of the domain Ω , the boundary conditions (2.2.2) and (2.2.3) are imposed at each particle of the corresponding boundary. In the case of the model problem, this leads to the linear system of equations for the coefficients u_i :

$$\begin{aligned} \sum_i u_i [\Delta N_i(x_J) - N_i(x_J)] &= -f(x_J) & \forall x_J \in \Omega, \\ \sum_i u_i N_i(x_J) &= u_D(x_J) & \forall x_J \in \Gamma_D, \\ \sum_i u_i \frac{\partial N_i}{\partial \mathbf{n}}(x_J) &= q_N(x_J) & \forall x_J \in \Gamma_N. \end{aligned}$$

Note that, the shape functions must be \mathcal{C}^2 , and thus, a \mathcal{C}^2 window function must be used.

In this case the solution at particle x_J is approximated by

$$u(x_J) \simeq u^\rho(x_J) = \sum_i u_i N_i(x_J),$$

which in general differs from the coefficient u_J (see remark 2.1.1). There are other possibilities. In the context of the RMD (Vila 1999), the coefficient u_J is considered as the approximation at the particle x_J and only the derivative of the solution is approximated through the Renormalized Meshless Derivative (2.1.7). Thus, the linear system to be solved becomes

$$\begin{aligned} \sum_i u_i \Delta N_i(x_J) - u_J &= -f(x_J) & \forall x_J \in \Omega, \\ u_J &= u_D(x_J) & \forall x_J \in \Gamma_D, \\ \sum_i u_i \frac{\partial N_i}{\partial \mathbf{n}}(x_J) &= q_N(x_J) & \forall x_J \in \Gamma_N. \end{aligned}$$

Both possibilities are slightly different from the SPH method by Monaghan (Monaghan 1988) or from SPH methods based on particle integration techniques (Bonet and Kulasegaram 2000).

2.2.2 Methods based on a Galerkin weak form

The mesh-free shape functions can also be used in the discretization of the weak integral form of the boundary value problem.

In the case of the model problem (2.2.1), the typical weak form (used in the finite element method) is

$$\int_{\Omega} \nabla v \nabla u \, d\Omega + \int_{\Omega} v u \, d\Omega = \int_{\Omega} v f \, dv + \int_{\Gamma_N} v q_N \, d\Gamma, \quad \forall v,$$

where v vanishes at Γ_D and $u = u_D$ at Γ_D . However, this weak form can not be directly discretized with a standard mesh-free interpolation. The shape functions do not verify the Kronecker delta property (see remark 2.1.1) and thus, it is difficult to select v such that $v = 0$ at Γ_D and to impose that $u^\rho = u_D$ at Γ_D . Specific techniques are needed in order to impose Dirichlet boundary conditions. Section 2.2.3 is devoted to the treatment of essential boundary conditions in mesh-free methods.

There are to other important topics in the implementation of a mesh-free method:

- how to evaluate the integrals in the weak form (there is not the concept of finite element, with a numerical quadrature in each element), and

- how to localize the neighbouring particles, that is, given a point x where the shape functions must be computed, identify which particles have a non-zero shape function at this point (x_i such that $\phi(\frac{x-x_i}{\rho}) \neq 0$) and which particles are present in the definition of the shape functions (usually the same particles).

In order to localize the neighbouring particles a regular mesh of squares or cubes (cells) is usually used, see figure 2.8. The cells must cover all the computation domain Ω . For every cell, the indices of the particles inside the cell are stored. The regular structure of the cell mesh allows to, given a point x , find the cell where x is located and find the neighbouring particles just looking in the neighbouring cells.

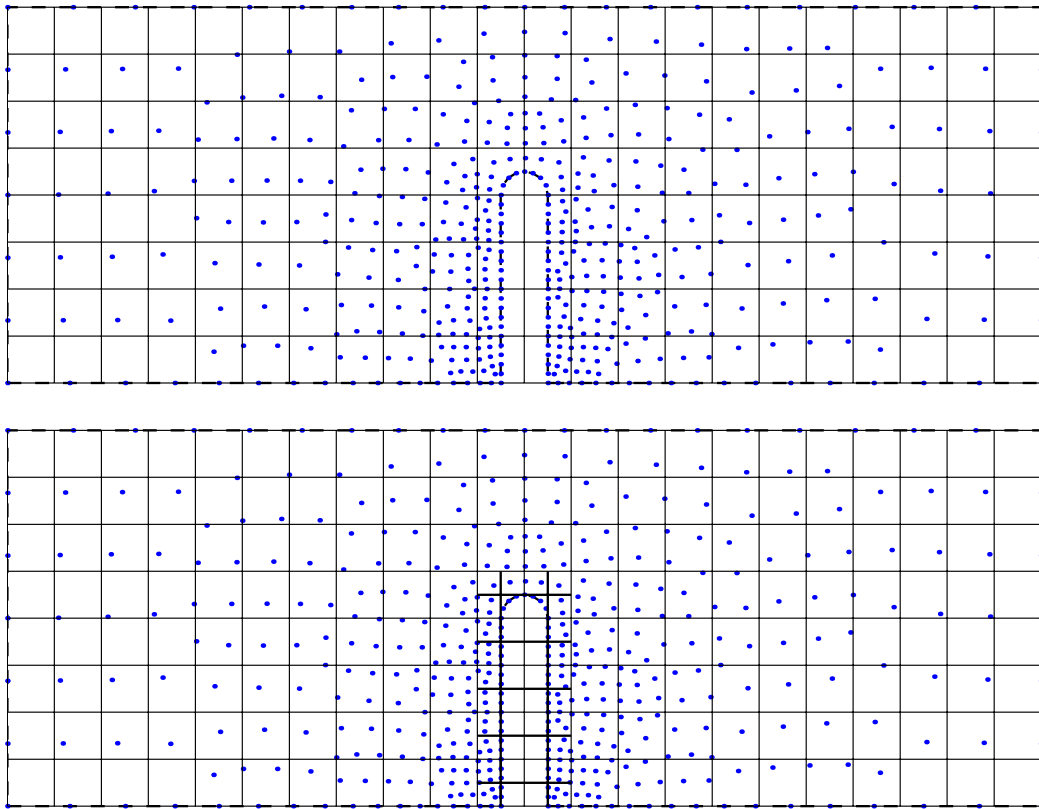


Figure 2.8: Particle distribution (in blue) and two possible cell structures. The first one is simpler; however, the second one is adapted to the geometry in a more efficient way.

Several possibilities can be considered to evaluate integrals in the weak form: (1) the integral can be evaluated taking the particles as integration points of the numerical quadrature (**particle integration**), (2) a regular cell structure (that can be the same used for the localization of particles) can be used with a numerical quadrature in each cell (**cell integration**,

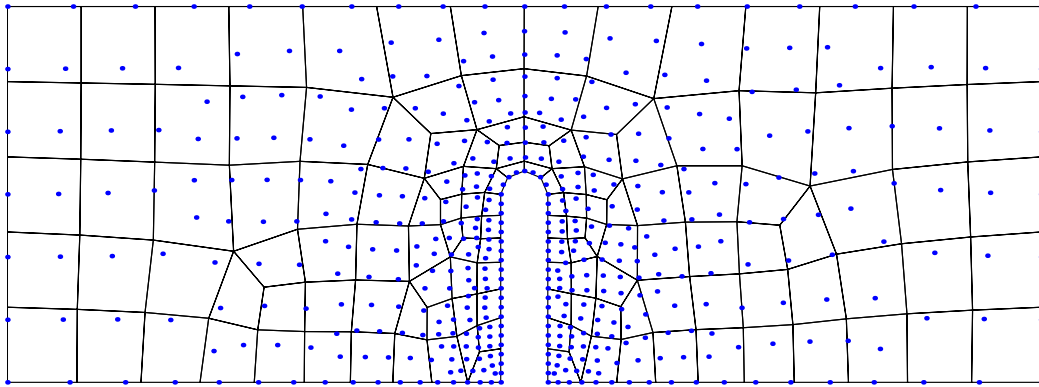


Figure 2.9: Particle distribution (in blue) and underground mesh.

see figure 2.8) or (3) a, not necessary regular, **background mesh** can be used to compute integrals, see figure 2.9. The first possibility (particle integration) is the fastest one, but as in collocation methods there can be instabilities in the solution and an accurate solution is not ensured. Recently, many possibilities have been proposed in order to obtain accurate and stable results with particle integration, see (Bonet and Kulasegaram 2000) for recent developments. The other two possibilities present the disadvantage that the resulting method is not considered a truly mesh-free method by some authors (Oñate and Idelsohn 1998). However, it is important to note that the cell structure, or the background mesh, does not need to be compatible with the particle distribution, and can be easily generated. In fact, a background cell structure is needed in all mesh-free methods, even with collocation or particle integration methods, in order to localize the neighbouring particles. This same cell structure may be used to compute integrals. However, in the presence of a complex domain, the boundary of the domain will not coincide with the boundaries of the cells, and a background finite element mesh will probably give more accurate results.

Maybe the best possibility is to use a background cell structure for the localization of neighbouring particles, and to use a background finite element mesh for the computation of integrals. Note that, the background element mesh can be as simple as you need and, since it will only be used for the numerical quadrature, it can even include non conforming elements. Moreover, in a refinement process, the background mesh can remain constant and only the particle distribution must be refined.

2.2.3 Essential boundary conditions

Many specific techniques have been developed in the recent years in order to impose essential boundary conditions in mesh-free methods. Some possibilities are: (1) use Lagrange multipliers (Belytschko et al. 1994), (2) modified variational principles (Belytschko et al. 1994), (3) penalty methods (Zhu and Atluri 1998), (4) perturbed Lagrangian (Chu and Moran 1995), (5) coupling to finite elements (Belytschko, Organ and Krongauz 1995, Huerta and Fernández-Méndez 2000, Wagner and Liu 2001), or (6) specially modified shape functions (Gosz and Liu 1996, Günter and Liu 1998, Wagner and Liu 2000), among others.

The Lagrange multiplier method allows us to impose essential boundary conditions in a simple and accurate way. This method will be commented in detail later. One possible disadvantage of this method is that, in the resolution of a self-adjoint problem, the discrete equations leads to a not positive-definite and not banded matrix. The variational principle provides a banded matrix but with poor accuracy in the boundary conditions.

On the other hand, Liu and coworkers have developed other techniques based on a suitable definition of the shape functions near the Dirichlet boundaries. The shape functions can be enforced to conform at essential boundaries (Gosz and Liu 1996). That is,

$$N_i(x_J) = \delta_{iJ}, \quad \forall x_J \text{ in } \Gamma_D,$$

and thus, essential boundary conditions can be easily imposed as in standard finite elements. By introducing an extension of the dilation parameter at each particle x_j near the essential boundary, termed a dilation function $\rho_j(x)$, the shape functions associated to particles out of Γ_D are made to vanish at the essential boundary. However, the definition of the dilation function can be difficult in the presence of complex domains, and the computation of the derivatives of the shape functions becomes a little more difficult due to the dependence of ρ_j on x .

In (Günter and Liu 1998) the d'Alembert's principle is developed for mesh-free methods with both linear or non linear equations and boundary conditions. A mesh-free interpolation is considered for the solution u (for instance displacements), and the virtual variables δu (virtual displacements),

$$u \simeq \sum_i N_i(x) d_i = \mathbf{N}^T \mathbf{d}, \quad \delta u \simeq \sum_i N_i(x) \delta d_i = \mathbf{N}^T \delta \mathbf{d},$$

where $\mathbf{N}^T = \{N_1, N_2 \dots\}$. In the linear case, the essential boundary conditions can be written in terms of linear combination,

$$\mathbf{G}^T \mathbf{d} = \mathbf{g}, \quad \mathbf{G}^T \delta \mathbf{d} = \mathbf{0}. \quad (2.2.4)$$

Orthogonality of \mathbf{G} is assumed and a Jacobian matrix \mathbf{J} such that $\mathbf{J}^T \mathbf{G} = \mathbf{0}$ and $\mathbf{J}^T \mathbf{J} = \mathbf{I}$ is then considered in order to express \mathbf{d} and $\delta \mathbf{d}$ using generalized variables \mathbf{y} and generalized virtual variations $\delta \mathbf{y}$,

$$\mathbf{d} = \mathbf{J}\mathbf{y} + \mathbf{G}\mathbf{g}, \quad \delta \mathbf{d} = \mathbf{J}\delta \mathbf{y}.$$

The constraints (2.2.4) are satisfied for all \mathbf{y} and $\delta \mathbf{y}$. The approximation can then be written as

$$u(x) \simeq [\mathbf{N}^J]^T \mathbf{y} + [\mathbf{N}^G]^T \mathbf{g},$$

with $\mathbf{N}^J = \mathbf{J}\mathbf{N}$ and $\mathbf{N}^G = \mathbf{G}\mathbf{N}$. This can be interpreted as splitting the shape functions \mathbf{N} into the interior set \mathbf{N}^J and the boundary set \mathbf{N}^G . The final interpolation resembles the boundary condition treatment in finite elements. However, when \mathbf{G} is obtained by a collocation technique, an inconsistency of this method is pointed out in (Wagner and Liu 2000) and a corrected collocation method must be considered.

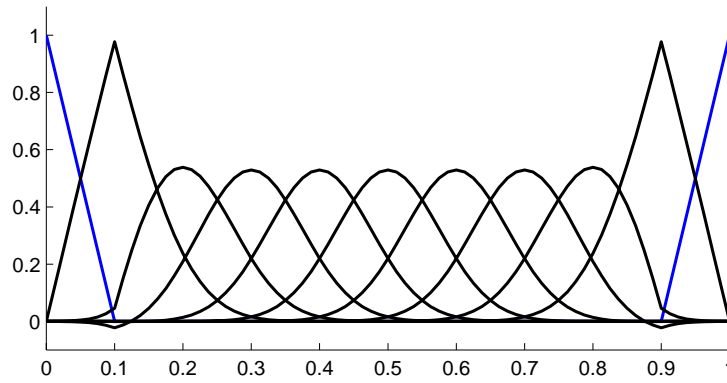


Figure 2.10: Mixed interpolation with linear finite element nodes near the boundary and particles in the interior of the domain, with $\rho/h = 3.2$, cubic spline and linear consistency in all the domain.

In the recent years, some authors have developed mixed interpolations that combine finite elements and mesh-free methods. This mixed interpolations can be useful for imposing essential boundary conditions. The idea is to discretize the domain using finite elements in a neighbourhood of the Dirichlet boundary and a mesh-free interpolation in the rest of the domain. Thus, the essential boundary conditions can be imposed as in standard finite elements. In (Belytschko et al. 1995) a mixed interpolation is defined in the transition area (from the finite elements region to the particles region). This mixed interpolation requires the substitution of finite element nodes by particles and the definition of ramp functions. Thus, the transition is of the size of one element and the interpolation is linear. Following

this idea, (Huerta and Fernández-Méndez 2000) proposes a more general mixed interpolation, with any order of interpolation, suppressing the ramp functions and with no substitution of nodes by particles. This is done preserving consistency and continuity of the solution. Figure 2.10 shows an example of this mixed interpolation in 1D: two finite element nodes are considered at the boundary of the domain, with their corresponding shape functions in blue, and the mesh-free shape functions are modified in order to preserve consistency, in black. Chapter 4 is devoted to this mixed interpolation, its properties, and its applications in enrichment and refinement processes. Recently (Wagner and Liu 2001) have developed a new mixed interpolation with many similarities with the approach in (Huerta and Fernández-Méndez 2000).

Lagrange multipliers

The Lagrange multiplier method is one of the most accurate methods for imposing essential boundary conditions. For the model problem defined by (2.2.1), (2.2.2) and (2.2.3) the weak form can be written as

$$\int_{\Omega} \nabla v \nabla u \, d\Omega + \int_{\Omega} v u \, d\Omega + \int_{\Gamma_D} v \lambda = \int_{\Omega} v f \, dv + \int_{\Gamma_N} v q_N \, d\Gamma, \quad \forall v, \quad (2.2.5)$$

$$\int_{\Gamma_D} \gamma (u - u_D) = 0 \quad \forall \gamma, \quad (2.2.6)$$

where $\lambda(x)$ is the Lagrange multiplier and $\gamma(x)$ is the associated virtual variable. The Lagrange multiplier must be interpolated in the essential boundary Γ_D . In order to interpolate λ many possibilities can be considered.

Collocation techniques correspond to the interpolation defined by

$$\lambda(x) \simeq \sum_{i \in I_D} \delta(x - x_i) \lambda_i,$$

where I_D is the set of indices of particles on the essential boundary, $I_D = \{i \mid x_i \in \Gamma_D\}$, $\delta(x)$ is the Dirac delta function, and λ_i are the coefficients of the linear combination. With this interpolation, the essential boundary conditions are exactly imposed at the particles in Γ_D . This is a very easy and popular approach, but can suffer from instabilities (Wagner and Liu 2000).

The essential boundary conditions can also be imposed in weak form, with a continuous interpolation of the Lagrange multiplier. Some possibilities are

- (i) $\lambda(x) \simeq \sum_{i \in I_D} N_i(x) \lambda_i$, where $N_i(x)$ are mesh-free shape functions associated to particles on the essential boundary,

- (ii) $\lambda(x) \simeq \sum_{i \in \tilde{I}_D} N_i(x) \lambda_i$, where $N_i(x)$ are mesh-free shape functions associated to particles whose supports intersect the essential boundary, $\tilde{I}_D = \{i \mid \text{supp}(N_i) \cap \Gamma_D \neq \emptyset\}$,
- (iii) $\lambda(x) \simeq \sum_{i \in \tilde{I}_{FE}} N_i^{FE}(x) \lambda_i$, where the multiplier is interpolated with finite element shape functions, $N_i^{FE}(x)$, associated to a finite element mesh which discretizes only the essential boundary.

The approximation in (i) is not consistent, in the sense that the approximation of the Lagrange multiplier in Γ_D does not reproduce even a constant multiplier (0-order consistency). In order to interpolate $\lambda(x)$ in a consistent way, all mesh-free shape functions must be considered, even those associated with particles outside the boundary; this corresponds to option (ii). However, usually this interpolation does not verify the LBB inf-sup condition by Ladyzenskaya-Babuska-Brezzi and the resulting matrix of equations becomes singular. The third possibility allows used to interpolate the Lagrange multiplier in a consistent and easy way. Note that the construction of the finite element mesh in the essential boundary usually does not represent a difficult problem: in 2D problems the FE mesh is a 1D finite element mesh, and in 3D problems only a part of the 2D boundary must be discretized. In fact, in most applications, all the boundary must be discretized in order to define the geometry and the discretization of the essential boundary does not imply an increase in the computational cost. However, there must be an agreement between the particle discretization in the interior of the domain and the finite element discretization of the essential boundary, in order to satisfy the LLB inf-sup condition, avoiding singular matrices, and obtain an accurate interpolation of the solution in the essential boundary.

2.2.4 EFG implementation details: computation of EFG interpolation functions and derivatives

In order to compute the EFG shape functions and its derivatives in a efficient way, expressions (2.1.27), (2.1.29) and (2.1.22) can be considered (see (Belytschko, Krongauz, Organ, Fleming and Krysl 1996) and (Belytschko, Krongauz, Fleming, Organ, and Liu 1996)).

Let us assume $x \in \mathbb{R}$ (for higher dimensions the same process can be performed for each component of x). The derivative of the shape function (2.1.27) can be written as

$$\frac{dN_i}{dx}(x) = \alpha_x^T(x) \mathbf{P}(x_i) \phi\left(\frac{x-x_i}{\rho}\right) + \alpha^T(x) \mathbf{P}(x_i) \frac{1}{\rho} \phi_x\left(\frac{x-x_i}{\rho}\right), \quad (2.2.7)$$

where ϕ_x is the derivative of the window function and vector α_x is the derivative of vector α . An expression for α_x can be obtained by implicit derivation of (2.1.29),

$$\mathbf{M}_x \alpha + \mathbf{M} \alpha_x = \mathbf{P}_x,$$

where \mathbf{P}_x is the derivative of vector \mathbf{P} . That is, $\alpha_x(x)$ is the solution of the linear system of equations

$$\mathbf{M}(x) \alpha_x(x) = \mathbf{P}_x(x) - \mathbf{M}_x(x) \alpha(x),$$

where matrix \mathbf{M}_x is the derivative of matrix \mathbf{M} ,

$$\mathbf{M}_x(x) = \sum_j \mathbf{P}(x_j) \mathbf{P}^T(x_j) \frac{1}{\rho} \phi_x \left(\frac{x - x_j}{\rho} \right).$$

and the vector $\alpha(x)$ has been computed previously. Note that the product $\mathbf{M}_x(x) \alpha(x)$ can be computed in an efficient way as

$$\mathbf{M}_x(x) \alpha(x) = \frac{1}{\rho} \sum_j \mathbf{P}(x_j) [\mathbf{P}^T(x_j) \alpha(x)] \phi_x \left(\frac{x - x_j}{\rho} \right),$$

involving only vector operations. The same process can be done for higher order derivatives.

The same development can be done for the centred and scaled approach defined in the previous section. The derivative of the shape function defined by (2.1.31), (2.1.33) and (2.1.34), can be computed as

$$\begin{aligned} \frac{d\mathbf{N}_i}{dx}(x) &= \frac{1}{\rho} \mathbf{P}_x^T \left(\frac{x - x_i}{\rho} \right) \alpha(x) \phi \left(\frac{x - x_i}{\rho} \right) + \mathbf{P}^T \left(\frac{x - x_i}{\rho} \right) \alpha_x(x) \phi \left(\frac{x - x_i}{\rho} \right) \\ &\quad + \mathbf{P}^T \left(\frac{x - x_i}{\rho} \right) \alpha(x) \frac{1}{\rho} \phi_x \left(\frac{x - x_i}{\rho} \right), \end{aligned}$$

where vector α_x can be obtained as the solution of the linear system of equations

$$\mathbf{M}(x) \alpha_x(x) = -\mathbf{M}_x(x) \alpha(x).$$

The vector $\alpha(x)$ has been computed previously and the matrix \mathbf{M}_x is obtained by derivation of (2.1.34),

$$\begin{aligned} \mathbf{M}_x(x) &= \sum_j \frac{1}{\rho} \mathbf{P}_x \left(\frac{x - x_j}{\rho} \right) \mathbf{P}^T \left(\frac{x - x_j}{\rho} \right) \phi \left(\frac{x - x_j}{\rho} \right) + \sum_j \mathbf{P} \left(\frac{x - x_j}{\rho} \right) \frac{1}{\rho} \mathbf{P}_x^T \left(\frac{x - x_j}{\rho} \right) \phi \left(\frac{x - x_j}{\rho} \right) \\ &\quad + \sum_j \mathbf{P} \left(\frac{x - x_j}{\rho} \right) \mathbf{P}^T \left(\frac{x - x_j}{\rho} \right) \frac{1}{\rho} \phi_x \left(\frac{x - x_j}{\rho} \right). \end{aligned}$$

The expression for higher order derivatives of the shape functions can be obtained in a similar way.

Chapter 3

Locking in the incompressible limit for the Element Free Galerkin method

3.1 Introduction

Locking in finite elements has been a major concern since its early developments. It appears because poor numerical interpolation leads to an over-constrained system. This chapter studies locking of the Element Free Galerkin (EFG) method near the incompressible limit, *i.e.* the so-called volumetric locking. In particular, its behaviour is compared with standard finite elements, bilinear and biquadratic, which are recalled in Sections 3.2.2 and 3.2.3.

Locking of standard finite elements has been extensively studied. It is well known that bilinear finite elements lock in some problems and that biquadratic elements have a better behaviour (Hughes 1987, Armero 1999). Moreover, locking has also been studied for increasing polynomial degrees in the context of an hp adaptive strategy, see (Suri 1996). However, locking in mesh-free methods is still an open topic. Originally, see (Belytschko et al. 1994, Zhu and Atluri 1998), it was claimed that the EFG method did not exhibit volumetric locking. Now it is clear that this is not true. For instance, Dolbow and Belytschko use the numerical inf-sup condition to analyze the EFG method. Moreover, some authors (Askes et al. 1999, Dolbow and Belytschko 1999, Chen, Yoon, Wang and Liu 2000) claim that increasing the dilation parameter locking phenomena in mesh-free methods can be suppressed, or at least attenuated. Their argument is based on numerical examples (Askes et al. 1999, Dolbow and Belytschko 1999) or on the heuristic constraint ratio (Chen et al. 2000) proposed by Hughes (Hughes 1987). Finally they introduce new formulations to remedy this problem in (Dolbow and Belytschko 1999, Chen et al. 2000).

Here, a modal analysis (an eigenvector and eigenvalue analysis), see Section 3.3, is performed in order to clarify this issue. That is, the influence of the dilation parameter on the locking behaviour of EFG near the incompressible limit is determined studying the fundamental modes (base of the solution space) and their corresponding energy (eigenvalue). Moreover, the influence of the order of the approximation is also analyzed. Finally standard linear and nonlinear tests are performed in order to illustrate and confirm the conclusions of the modal analysis.

3.2 Volumetric locking in standard finite elements

3.2.1 Preliminaries

Before going into the locking analysis of mesh-free methods some preliminary notions of locking will be recalled in order to introduce the notation and the approach employed in following sections. This approach is restricted to a very particular case.

Only small deformations are considered, namely $\nabla^s \mathbf{u}$, where \mathbf{u} is the displacement and ∇^s the symmetric gradient, *i.e.* $\nabla^s = \frac{1}{2}(\nabla^T + \nabla)$. Moreover, linear elastic isotropic materials under plane strain conditions are considered. Dirichlet boundary conditions are imposed on Γ_D , a traction \mathbf{h} is prescribed along the Neumann boundary Γ_N and there is a body force \mathbf{f} . Thus, the problem that needs to be solved may be stated as: solve for $\mathbf{u} \in [H_{\Gamma_D}^1]^2$ such that

$$\begin{aligned} \frac{E}{1+\nu} \int_{\Omega} \nabla^s \mathbf{v} : \nabla^s \mathbf{u} d\Omega + \frac{E}{(1+\nu)(1-2\nu)} \int_{\Omega} (\nabla \cdot \mathbf{v})(\nabla \cdot \mathbf{u}) d\Omega \\ = \int_{\Omega} \mathbf{f} \cdot \mathbf{v} d\Omega + \int_{\Gamma_N} \mathbf{h} \cdot \mathbf{v} d\Gamma \quad \forall \mathbf{v} \in [H_{0,\Gamma_D}^1]^2. \end{aligned} \quad (3.2.1)$$

In this equation, the standard vector subspaces of H^1 are employed for the solution \mathbf{u}

$$[H_{\Gamma_D}^1]^2 := \{ \mathbf{u} \in [H^1]^2 \mid \mathbf{u} = \mathbf{u}_D \text{ on } \Gamma_D \}$$

(Dirichlet conditions, \mathbf{u}_D , are automatically satisfied) and for the test functions \mathbf{v}

$$[H_{0,\Gamma_D}^1]^2 := \{ \mathbf{v} \in [H^1]^2 \mid \mathbf{v} = \mathbf{0} \text{ on } \Gamma_D \}$$

(zero values are imposed along Γ_D).

This equation, as discussed in (Suri 1996), shows the inherent difficulties of the incompressible limit. The standard *a priori* error estimate emanating from (3.2.1) and based on

the energy norm, which is induced by the LHS of (3.2.1), is

$$\|\mathbf{u} - \mathbf{u}_h\| \leq \inf_{\mathbf{w} \in \mathcal{S}_h} \|\mathbf{u} - \mathbf{w}\| \leq C_{\mathbf{u}, \nu, p} h^{f(p)} \quad (3.2.2)$$

where \mathcal{S}_h is the finite dimensional subspace of $[H_{\Gamma_D}^1]^2$ in which the approximation \mathbf{u}_h is sought, $C_{\mathbf{u}, \nu, p}$ is a constant independent of h (characteristic size of the mesh) and p (degree of the polynomials used for the interpolation), and $f(p)$ is a positive monotone function of p . The subindices of the constant C indicate that it depends on the Poisson ratio, the order of the interpolation and the exact solution itself.

From (3.2.1) one can observe the difficulties of the energy norm to produce a small infimum in (3.2.2) for values of ν close to 0.5. In fact, in order to have finite values of the energy norm the divergence-free condition must be enforced in the continuum case, *i.e.* $\nabla \cdot \mathbf{u} = 0$ for $\mathbf{u} \in [H_{\Gamma_D}^1]^2$, and also in the finite dimensional space, *i.e.* $\nabla \cdot \mathbf{u}_h = 0$ for $\mathbf{u}_h \in \mathcal{S}_h \subset [H_{\Gamma_D}^1]^2$. In fact, locking will occur when the approximation space \mathcal{S}_h is not rich enough for the approximation to verify the divergence-free condition.

Under these conditions, it is evident that locking may be studied from the LHS of (3.2.1). This is the basis for the modal analysis of locking. The discrete eigenfunctions (the eigenvectors) corresponding to the LHS of (3.2.1) are computed because they completely describe, in the corresponding space, the behaviour of the bilinear operator induced by this LHS.

In computational mechanics it is standard to write the strain, $\boldsymbol{\varepsilon}$, and the stress, $\boldsymbol{\sigma}$, tensors in vector form. Moreover, under the assumptions already discussed, they are related as

$$\boldsymbol{\varepsilon} = \mathbf{B}\mathbf{d}, \quad \boldsymbol{\sigma} = \mathbf{C}\boldsymbol{\varepsilon}, \quad \mathbf{C} = \frac{E}{(1+\nu)(1-2\nu)} \begin{pmatrix} 1-\nu & \nu & 0 \\ \nu & 1-\nu & 0 \\ 0 & 0 & \frac{1-2\nu}{2} \end{pmatrix}.$$

Where \mathbf{d} is the vector of nodal displacements (the coefficients corresponding to the approximation \mathbf{u}_h in the base of \mathcal{S}_h), and \mathbf{B} is the standard matrix relating displacements and strains. Then, the stiffness matrix can be computed as usual,

$$\mathbf{K} = \int_{\Omega} \mathbf{B}^T \mathbf{C} \mathbf{B} \, d\Omega.$$

The modal analysis presented in the following is based on \mathbf{K} , which is naturally related to the energy norm in the finite dimensional interpolation space, \mathcal{S}_h , defined by the finite elements employed (and characterized by \mathbf{B}).

3.2.2 Bilinear finite elements (Q1)

The modal analysis of the bilinear (Q1) finite element is performed here. In particular, the incompressible limit is studied by evaluating the eigenvalues associated to each mode as the Poisson ratio, ν , tends to 0.5, see (Armero 1999).

Figures 3.1, 3.2 and 3.3 present the modes of a bilinear element and the evolution of the eigenvalues as ν goes to 0.5. The logarithm of the eigenvalue is plotted as a function of the logarithm of $0.5 - \nu$. The three rigid body modes have not been plotted because they do not have any interest in this study. One can easily recognize in these figures the shear, the stretch, the volumetric and the two hourglass modes. They are classified, as usual, see (Armero 1999), in three groups: (1) modes that do not present any locking behaviour, (2) modes that do have physical locking —the eigenvalue goes to infinity because it is a volumetric mode—, and (3) modes associated to non-physical locking —in this case, the hourglass modes—.

The first group, Figure 3.1, presents modes with eigenvalues that do not present an unbounded growth as ν goes to 0.5. In the incompressible limit, $\nu \simeq 0.5$, the displacement field determined by the eigenvalue can be obtained with a bounded force field. On other hand, the modes that do present locking, see Figures 3.2 and 3.3, have eigenvalues that go to infinity when ν approaches 0.5. That is, in the incompressible limit, the force field must be infinite in order to induce the displacements described by the eigenvector. However, such a behaviour is only expected for the volumetric modes and for the others it is non-physical.

Figure 3.2 shows the second stretch mode (a volumetric mode), which presents the expected physical locking. The displacement field of this mode does not conserve the area and, consequently, in the incompressible limit it must have an infinite stiffness (infinite eigenvalue). That is, if $\nu = 0.5$ the component of the solution associated to this mode must be zero.

However, the hourglass modes shown in Figure 3.3 do conserve the total area but suffer from non-physical locking. The interpolation space is not rich enough to ensure the divergence-free condition. In fact the hourglass modes do verify that

$$\int_{\square} \nabla \cdot \mathbf{u}_h \, d\mathbf{x} = 0,$$

but do not comply with the local divergence-free condition. This is clearly a non-physical locking behaviour. Figure 3.4 shows the difference between a divergence-free displacement field and its projection on the bilinear interpolation space. A larger approximation space, for instance biquadratic, may verify the divergence-free condition.

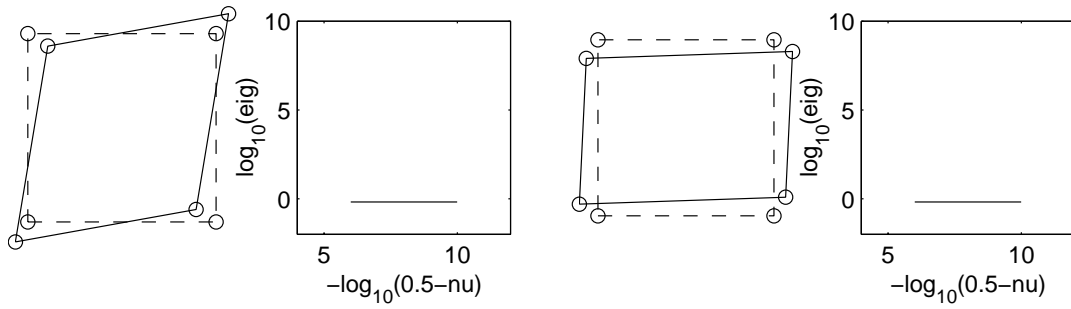


Figure 3.1: Non locking modes for one bilinear element (Q1)

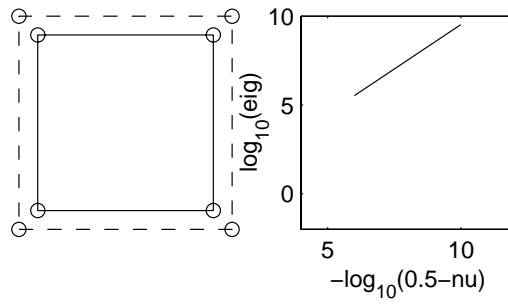


Figure 3.2: Physical locking mode for one bilinear element (Q1)

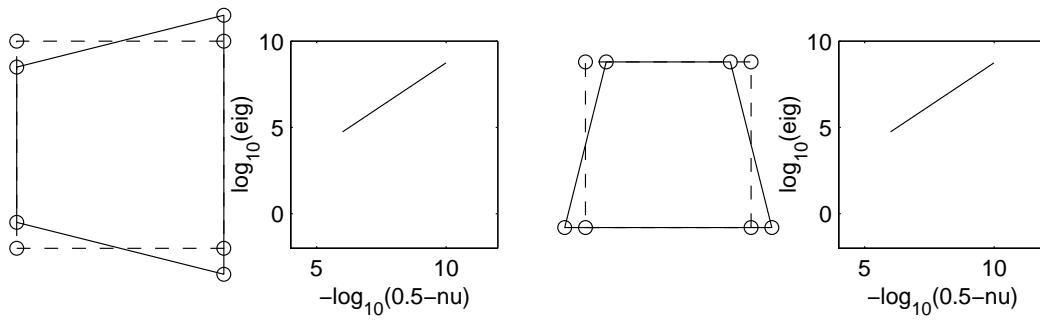


Figure 3.3: Non-physical locking modes for one bilinear element (Q1)

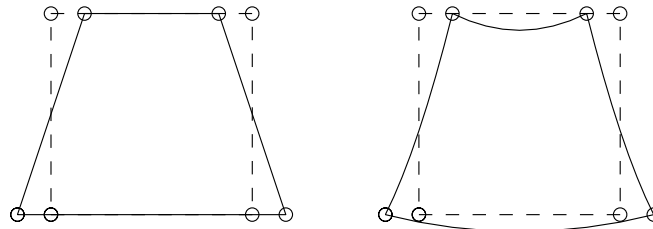


Figure 3.4: Comparison between the hourglass mode and a divergence-free bending field

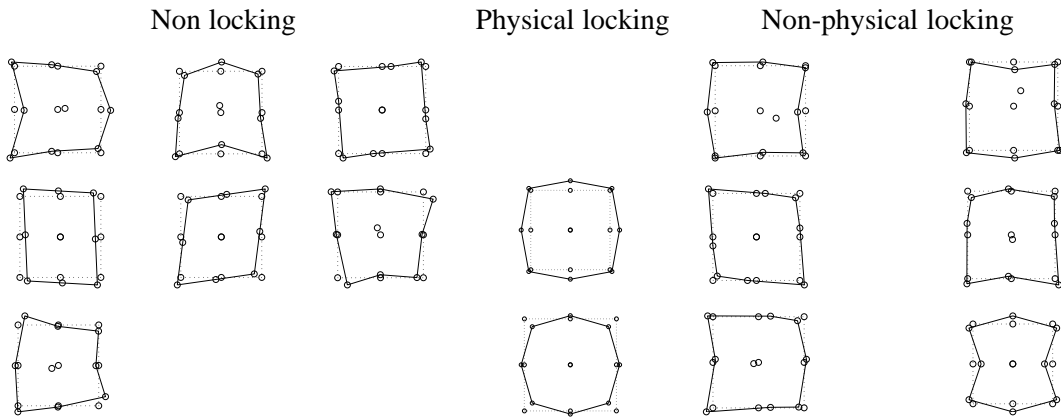


Figure 3.5: Modes for the Q2 element (9 nodes)

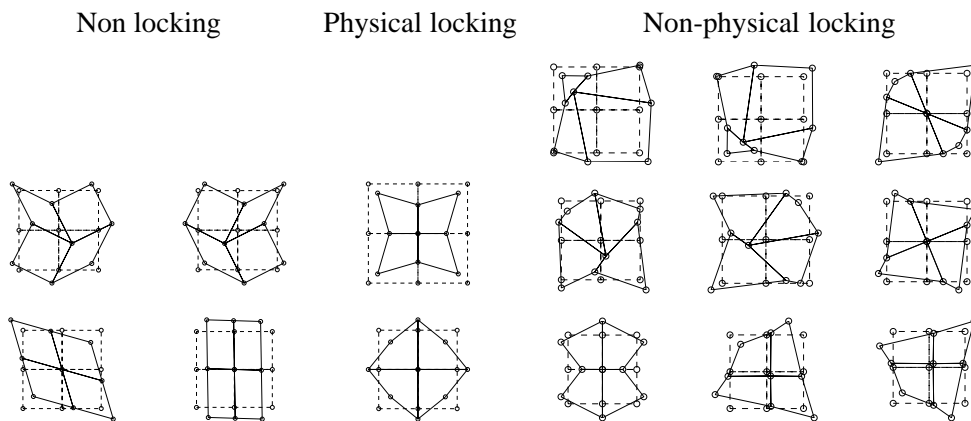


Figure 3.6: Modes of four Q1 elements (9 nodes)

In the following section a richer space is chosen: biquadratic finite elements. One expects that in this space the locking behavior is eliminated, or at least decreased, since displacement fields closer to a correct one shown in Figure 3.4 can be obtained.

3.2.3 Biquadratic finite elements (Q2)

Here the modes for the standard biquadratic element are shown. Moreover, these modes are compared with those of the previous bilinear element with an equivalent distribution of nodes. This comparison, standard in finite elements, will be extended to the mesh-free method.

Figure 3.5 shows the different modes (the rigid ones are again not shown) for the standard nine node element. Note that as expected, see (Suri 1996), there are still some non-physical locking modes. That is, some nodal displacements, which induce global conservation of area, are not able to reproduce a divergence-free field. Nevertheless, most of the standard academic tests (Askes et al. 1999, Dolbow and Belytschko 1999, Chen et al. 2000) do perform correctly with the biquadratic element. This simply indicates, and can easily be verified, that the solution field has a zero (or almost zero) coefficient associated to those non-physical locking modes.

Remark 3.2.1. In Figure 3.5, as well as in the following ones, the modes are ordered in each group (non locking, physical locking and non-physical locking) from large to smaller eigenvalue (left to right).

To further illustrate the importance of the interpolation space the modes of the Q2 element are compared with those of four Q1 elements. Note that both approximation spaces have the same dimension. Nevertheless, from Figures 3.5 and 3.6 one can notice that one Q2 element has less non-physical locking modes than the four Q1 elements. Three of the nine non-physical locking modes present in the Q1 elements (see Figure 3.6) have now, with one Q2, bounded eigenvalues as ν goes to 0.5. Thus a richer space does not necessarily mean a larger space, here both approximation spaces do have the same dimension.

This comparison suggests however two important issues that can influence the incompressible limit locking. The first one is related to the bandwidth. For the same number of nodes (the same space dimension) Q2 elements present a larger bandwidth. And the second one is the obvious difference between Q1 and Q2 elements: the order of the polynomials in the approximation space. Mesh-free methods allow to study these two phenomena independently; this is the objective of the following section.

3.3 Volumetric locking in element free Galerkin methods

In the previous section two alternative procedures were suggested in order to enrich the interpolation space: (i) increase the bandwidth or (ii) increase the order of the polynomial base.

Meshfree methods, and in particular the EFG method, see section 2.1.2, are specially suited for independently checking both alternatives: (i) the bandwidth can be increased by simply increasing the dilation parameter, which defines the support of the interpolation functions, keeping the consistency (order of the polynomial approximation) constant; (ii) for

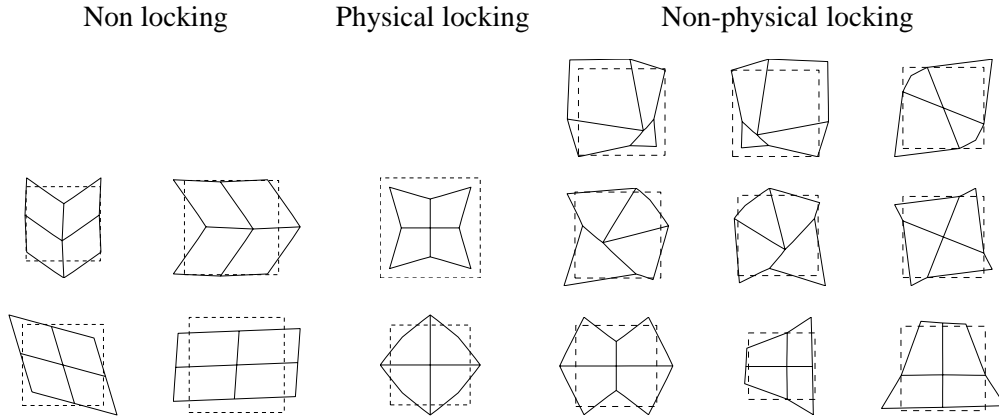


Figure 3.7: Modes for a 3×3 distribution of particles with Q_1 and $\rho/h = 1.2$.

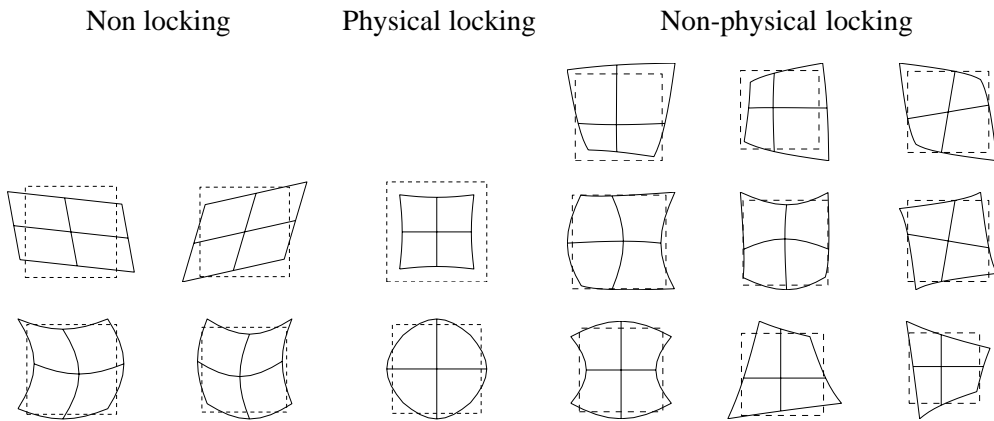


Figure 3.8: Modes for a 3×3 distribution of particles with Q_1 and $\rho/h = 2.2$.

large values of the dilation parameter the consistency can be also increased independently.

In the following, the polynomial spaces introduced in remark 2.1.8, \mathcal{P}_m and \mathcal{Q}_m , are considered. The behaviour of the EFG interpolation generated by the \mathcal{Q}_m polynomial space will be discussed in detail in order to compare with the finite element spaces presented previously, see Sections 3.2.2 and 3.2.3. However, two tables summarizing the locking properties are presented for the \mathcal{P}_m space. For simplicity, a rectangular support is chosen for the weighting function: $\phi(\mathbf{x}) = \phi_{1D}(|x_1|) \phi_{1D}(|x_2|)$ where ϕ_{1D} is the cubic spline in one dimension. However similar results can be obtained with Gaussian weighting functions or with circular supports.

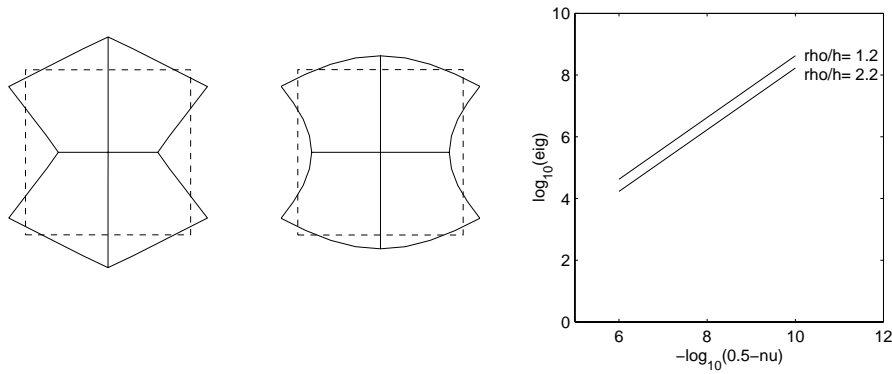


Figure 3.9: Evolution of the eigenvalue as ν goes to 0.5 for the same non-physical locking mode obtained with $\rho/h = 1.2$, and 2.2.

3.3.1 Locking for bilinear consistency

In order to compare the results of EFG with the previous ones obtained with finite elements, see Sections 3.2.2 and 3.2.3, a distribution of 3×3 particles is employed. Bilinear consistency corresponds to the polynomial space \mathcal{Q}_1 , namely $\mathbf{P} = \{1, x, y, xy\}^T$. Figures 3.7 and 3.8 show the modes already classified for two different dilation parameters, $\rho/h = 1.2$ and 2.2.

As expected the case of $\rho/h = 1.2$ does coincide with the Q1 element, see Figure 3.6. Recall that at the Gauss points the shape functions of the Q1 finite element and the interpolation functions for EFG with $\rho/h = 1.2$ are almost identical, see remark 2.1.13, thus the eigenvalue analysis should give similar results.

By increasing ρ/h up to 2.2 with the same consistency requirement the bandwidth of the matrix is increased. Nevertheless, the same number of non-physical locking modes is obtained. Notice however that an increase of the dilation parameter improves the smoothness of the approximation. The same modes are obtained but the interpolation of the displacements is smoother. This clearly indicates that an increase of the dilation parameter does not preclude locking. In fact the same modes will still present locking.

This conclusion does not contradict previous numerical experiments (Askes et al. 1999, Dolbow and Belytschko 1999, Chen et al. 2000). In Figure 3.9 the evolution of eigenvalue as ν goes to 0.5 is plotted for the same non-physical locking mode obtained first with $\rho/h = 1.2$ and then with 2.2. As noticed before the shape of the mode is improved increasing the dilation parameter. This is a clear indication that at a given point \mathbf{x} more particles interact and a better interpolation is obtained. This better approximation does not preclude locking

Table 3.1: Mode classification for a distribution of 4×4 particles/nodes

| | Q1 | Q2 | $\rho/h = 2.2$ Q ₁ | $\rho/h = 3.2$ Q ₁ | $\rho/h = 2.2$ Q ₂ | $\rho/h = 3.2$ Q ₂ | $\rho/h = 3.2$ Q ₃ |
|----------------------|----|----|----------------------------------|----------------------------------|----------------------------------|----------------------------------|----------------------------------|
| Non locking | 6 | - | 6 | 6 | 9 | 9 | 14 |
| Physical locking | 4 | - | 4 | 4 | 4 | 4 | 4 |
| Non-physical locking | 19 | - | 19 | 19 | 16 | 16 | 11 |

Table 3.2: Mode classification for a distribution of 5×5 particles/nodes

| | Q1 | Q2 | $\rho/h = 2.2$ Q ₁ | $\rho/h = 3.2$ Q ₁ | $\rho/h = 2.2$ Q ₂ | $\rho/h = 3.2$ Q ₂ | $\rho/h = 3.2$ Q ₃ |
|----------------------|----|-----------|----------------------------------|----------------------------------|----------------------------------|----------------------------------|----------------------------------|
| Non locking | 8 | 16 | 8 | 8 | 11 | 11 | 16 |
| Physical locking | 6 | 6 | 6 | 6 | 6 | 6 | 6 |
| Non-physical locking | 33 | 25 | 33 | 33 | 30 | 30 | 25 |

but reduces its effect by decreasing the eigenvalue. As ν goes to 0.5 the energy needed grows unbounded but for a constant ν as ρ/h increases the eigenvalue decreases. Thus volumetric locking is not suppressed when the dilation parameter increases but, as noticed in (Askes et al. 1999, Dolbow and Belytschko 1999, Chen et al. 2000) its effect is attenuated.

If the patch of particles is increased, in order to use larger dilation parameters, similar conclusions are drawn:

1. The number of non-physical locking modes is independent of the ratio ρ/h .
2. An increase of the dilation parameter decreases the eigenvalue (amount of energy) of the locking mode attenuating, but not suppressing, the volumetric locking (in the incompressible limit the same problems will occur).

Figures 3.10, 3.11 and 3.12 show the modes for a 4×4 particle distribution. This patch can be compared with nine Q1 elements. Bilinear consistency is still imposed, $\mathbf{P} = \{1, x, y, xy\}^T$, and the ratios studied correspond to $\rho/h = 1.2, 2.2$ and 3.2 . Table 3.1 presents a summary of these results. Moreover, Figure 3.13 compares the evolution of the eigenvalue associated to the same non-physical locking mode for the previously indicated ratios.

The same conclusions are obtained with a larger number of particles, Table 3.2 presents a summary of the results.

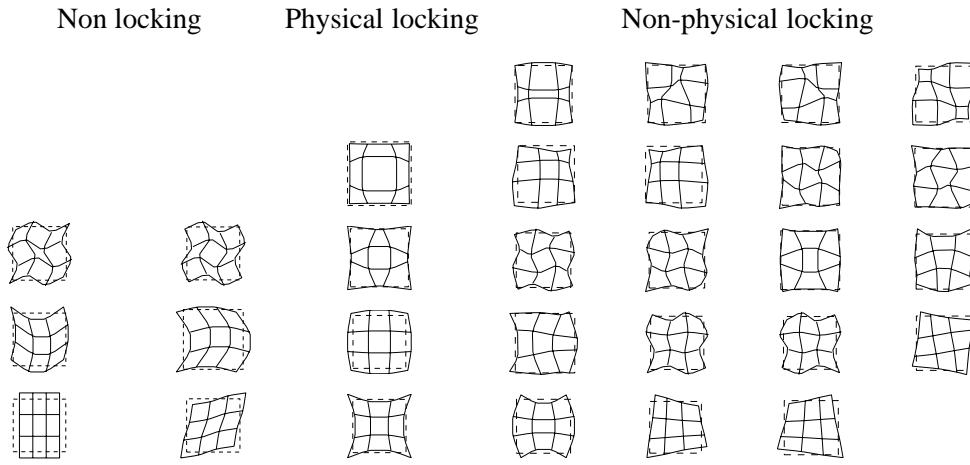


Figure 3.10: Modes for a 4×4 distribution of particles with Q_1 and $\rho/h = 1.2$.

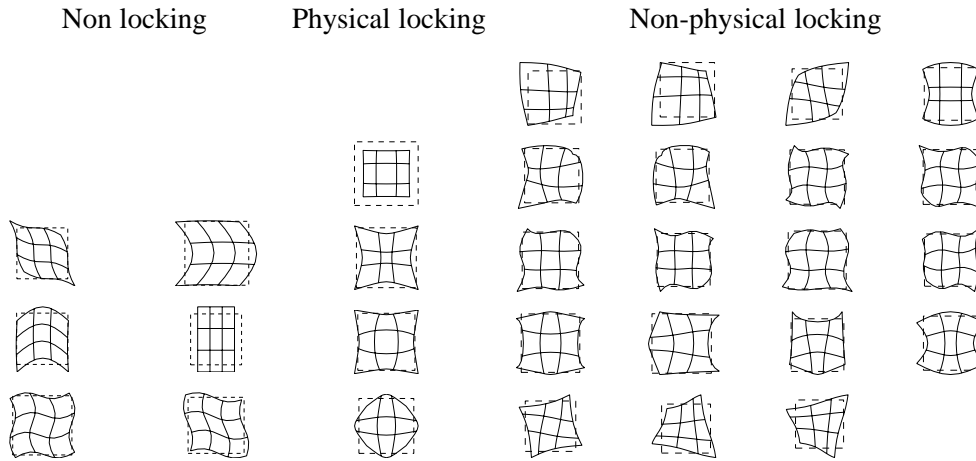


Figure 3.11: Modes for a 4×4 distribution of particles with Q_1 and $\rho/h = 2.2$.

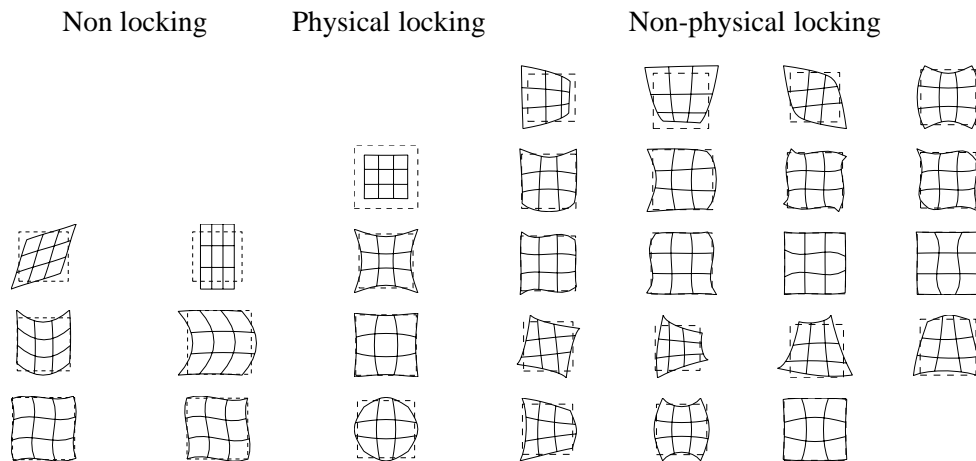


Figure 3.12: Modes for a 4×4 distribution of particles with Q_1 and $\rho/h = 3.2$.

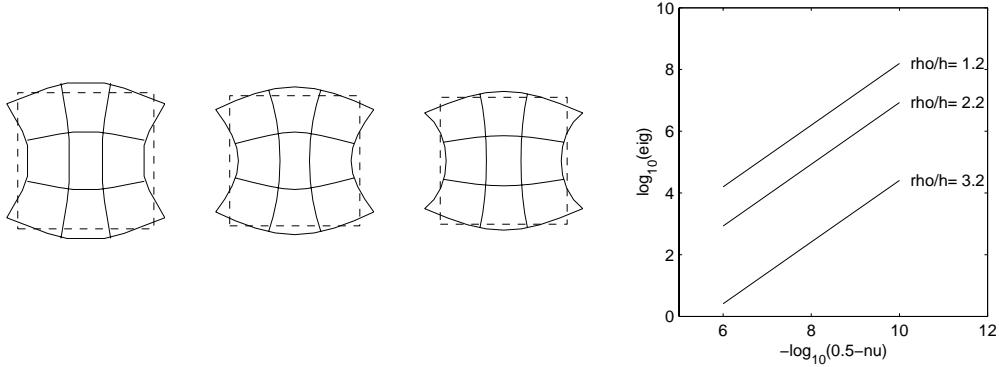


Figure 3.13: Evolution of the eigenvalue as ν goes to 0.5 for the same non-physical locking mode obtained with $\rho/h = 1.2, 2.2,$ and 3.2 .

Remark 3.3.1. At this point it seems important to notice that although the modal analysis suggests that increasing the dilation parameter locking is alleviated, in practice the dilation parameter can not be taken arbitrarily large. Recall that the EFG method is based on a MLS approximation. The local nature of such approximation will be lost for arbitrarily large ρ . In fact, for large enough values of ρ a global least-squares approach is recovered. The numerical examples shown in Section 3.4 corroborate this issue.

Remark 3.3.2. Non-physical or physical locking modes are determined depending on the conservation or not of the area. In order to verify the conservation of area and to preclude numerical errors two techniques are used: (1) numerical integration of the divergence of the displacement and (2) computation of the displacement flux along the edges. Both methods give the same results with a clear threshold (several orders of magnitude) between constant or variable area.

3.3.2 Locking for biquadratic consistency

In finite elements when the order of consistency is increased volumetric locking is alleviated, and in some cases suppressed (Suri 1996). As previously done for finite elements, quadratic consistency is studied. First, the results previously obtained with the Q2 element are reproduced with the EFG method. Thus a domain defined with a distribution of 3×3 particles is employed with consistency in \mathcal{Q}_2 , *i.e.* $\mathbf{P} = \{1, x, y, xy, x^2, y^2, x^2y, xy^2, x^2y^2\}^T$. Figure 3.14 shows the modes in this case, which, as expected, do coincide with the modes of the Q2 element, see Figure 3.5. The ratio ρ/h is in this case 2.2. Every point in the

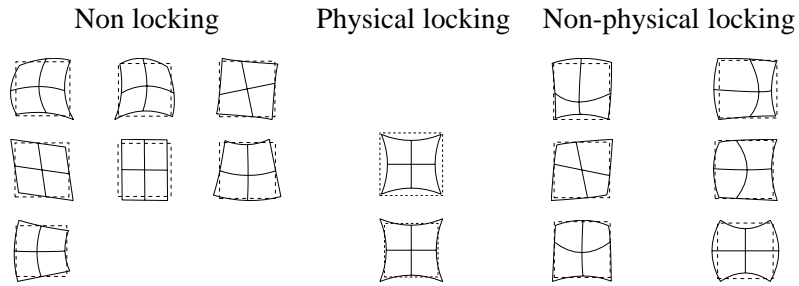


Figure 3.14: Modes for a 3×3 distribution of particles with Q_2 and $\rho/h = 2.2$.

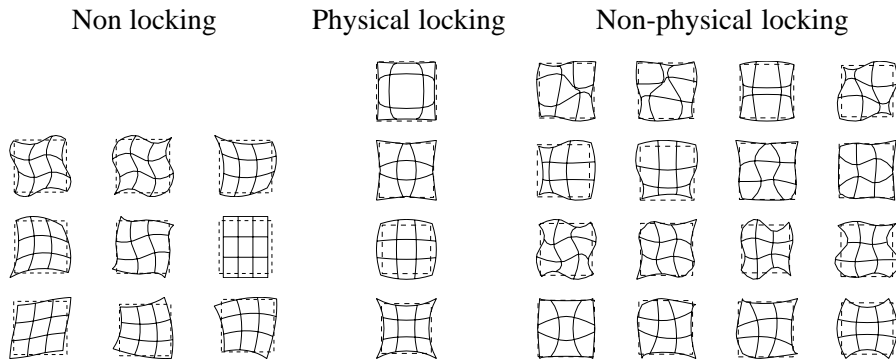


Figure 3.15: Modes for a 4×4 distribution of particles with Q_2 and $\rho/h = 2.2$.

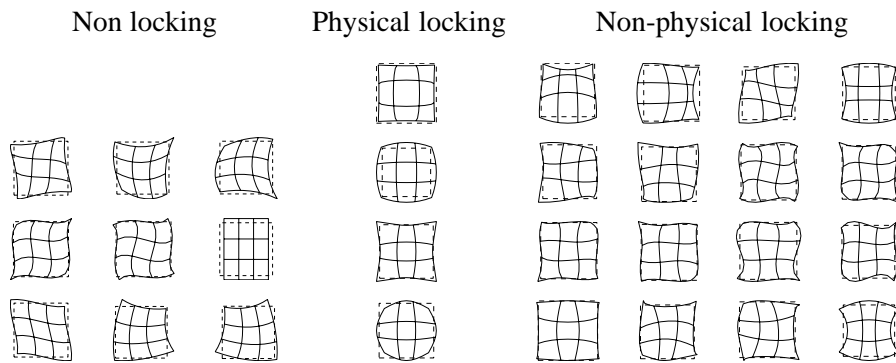


Figure 3.16: Modes for a 4×4 distribution of particles with Q_2 and $\rho/h = 3.2$.

Table 3.3: Mode classification for a distribution of 4×4 particles/nodes

| | P1 | P2 | \mathcal{P}_1 | \mathcal{P}_2 | \mathcal{P}_3 |
|----------------------|----|----|-----------------|-----------------|-----------------|
| Non locking | 11 | - | 6 | 8 | 11 |
| Physical locking | 6 | - | 4 | 4 | 3 |
| Non-physical locking | 12 | - | 19 | 17 | 15 |

Table 3.4: Mode classification for a distribution of 5×5 particles/nodes

| | P1 | P2 | P4 | \mathcal{P}_1 | \mathcal{P}_2 | \mathcal{P}_3 | \mathcal{P}_4 |
|----------------------|----|----|----|-----------------|-----------------|-----------------|-----------------|
| Non locking | 15 | 23 | 27 | 8 | 10 | 13 | 17 |
| Physical locking | 10 | 7 | 6 | 6 | 6 | 5 | 6 |
| Non-physical locking | 22 | 17 | 14 | 33 | 31 | 29 | 24 |

domain is under the influence of the nine particles. In fact, second order consistency can not be obtained with $\rho/h = 1.2$ because the first necessary condition presented in Remark 2.1.11 is not satisfied.

This reduction in the number of non-physical locking modes is also observed when a 4×4 distribution of particles is used. See Figures 3.15 and 3.16 which should compare with Figures 3.10, 3.11 and 3.12. A summary of these results is shown in Table 3.1. This reduction of non-physical modes due to an increase in the order of consistency is not affected when the dilation parameter is modified. These results can not be compared with the Q2 element because it is not possible with biquadratic elements to obtain a distribution of 4×4 nodes.

If a distribution of 5×5 particles is chosen, results may be compared between EFG, Q1 and Q2 finite elements. The results are presented in Table 3.2. Again, the number of non-physical modes is reduced compared with the linear order of consistency. However, compared with the Q2 element, the EFG method has more non-physical locking modes than the biquadratic finite element. Recall that in EFG all approximation functions are identical. This is not the case for finite elements, midside nodes have different shape functions than corner nodes.

Finally, for completeness, Tables 3.3 and 3.4 show, for the same 4×4 and 5×5 particle distribution, a comparison between the complete set of polynomials \mathcal{P}_m (degree $\leq m$), see Remark 2.1.8, and their corresponding finite elements. Notice that similar conclusions can be drawn.

3.4 Numerical examples

In this section three standard academic examples are used to illustrate the previously obtained results.

3.4.1 The cantilever beam

A beam with linear isotropic material, under plane strain conditions and with a parabolic traction applied to the free end is considered, as shown in Figure 3.17. Displacements in

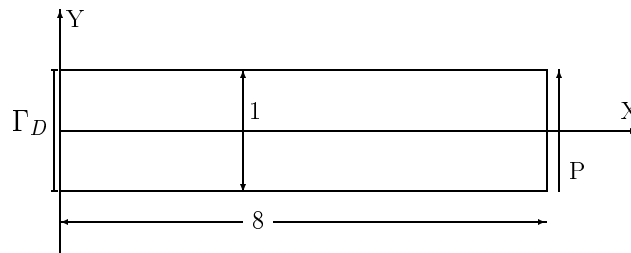


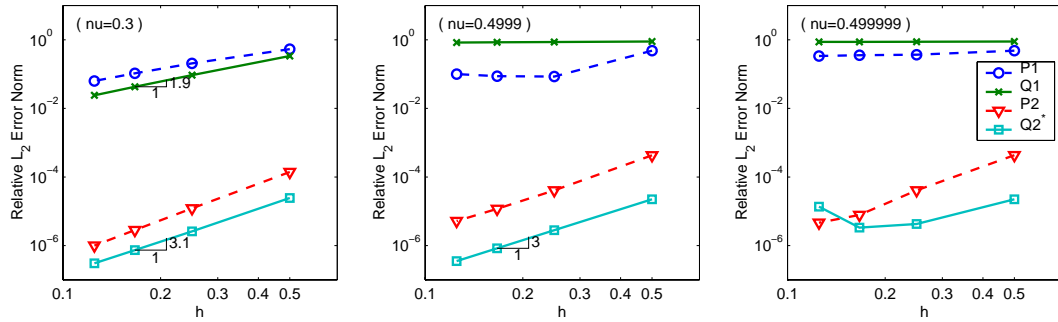
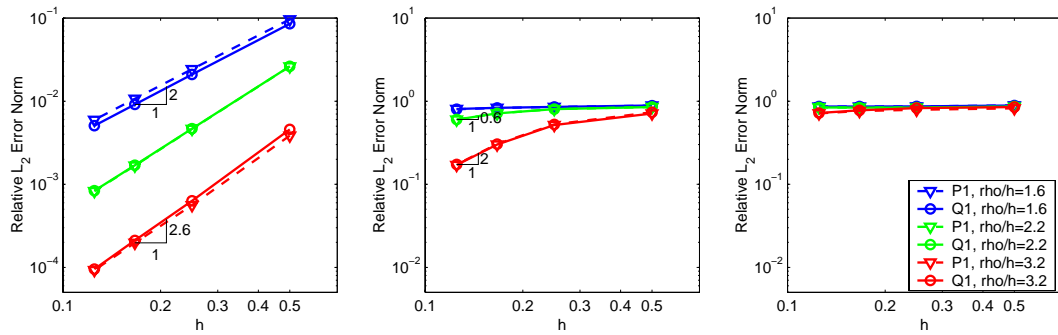
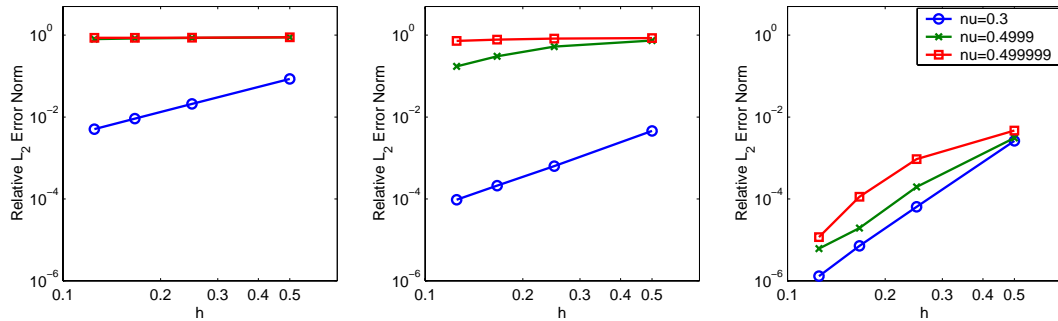
Figure 3.17: Cantilever beam problem

both directions are prescribed at Γ_D . The prescribed displacements and the applied traction are such that the solution is known in closed form (Hughes 1987, Dolbow and Belytschko 1999):

$$\begin{aligned}
 u_x &= -\frac{2E}{1-\nu^2}y \left[(48-3x)x + \left(2 + \frac{\nu}{1-\nu}\right)(y^2 - 0.25) \right], \\
 u_y &= \frac{2E}{1-\nu^2} \left[3\frac{\nu}{1-\nu}y^2(8-x) + \left(4 + 5\frac{\nu}{1-\nu}\right)\frac{x}{4} + (24-x)x^2 \right] \\
 \sigma_{xx} &= -12y(8-x), \quad \sigma_{yy} = 0, \quad \sigma_{xy} = 6(0.25 - y^2)
 \end{aligned}$$

The problem is solved with uniform distributions of nodes, when FE are used, or particles, when EFG is used.

Figure 3.18 shows the relative L_2 error in displacements for $\nu = 0.3, 0.4999$ and 0.499999 . Results are shown for 3-noded linear FE (P1), 4-noded bilinear FE (Q1), 6-noded quadratic FE (P2) and 8-noded FE (Q2*). The typical convergence rates are obtained when $\nu = 0.3$, but, as expected, results degrade as ν gets closer to the incompressible limit 0.5. All interpolations suffer from volumetric locking. However, the best results are obtained with interpolations of order two, where locking effects are negligible when $\nu = 0.4999$ and good results are still obtained when $\nu = 0.499999$.

Figure 3.18: Relative L_2 error with FE and $\nu = 0.3, 0.4999, 0.499999$ Figure 3.19: Relative L_2 error with EFG and $\nu = 0.3, 0.4999, 0.499999$ Figure 3.20: Relative L_2 error with Q_1 and $\rho/h = 1.6$ (left), with Q_1 and $\rho/h = 3.2$ (centre) and with Q_2 and $\rho/h = 3.2$ (right).

Similar results are shown for EFG in Figures 3.19 and 3.20. The cubic spline weighting function with circular support is used to define the EFG shape functions and Lagrange multipliers are used in order to impose the prescribed displacements.

Interpolations with consistency of order one, \mathcal{P}_1 and Q_1 , are considered in Figure 3.19 with three different values of the ratio ρ/h . Note that, for a given ρ/h , similar behaviours are obtained with the \mathcal{P}_1 and Q_1 interpolations, as the modal analysis showed. Far from the incompressible limit, when $\nu = 0.3$, the convergence is as expected or even better. The best solutions are always obtained when $\rho/h = 3.2$. However, near the incompressible

limit the solution suffers from locking for all values of ρ/h : the solution degrades as ν gets closer to the incompressible limit as can be seen in Figure 3.20. Figure 3.20 also shows the results obtained with a Q_2 interpolation. In this example, with consistency imposed in Q_2 , locking effects are small since the solution has an almost zero projection in the subspace of non-physical locking modes.

3.4.2 The plate with a hole

The stress field of an infinite plate with a hole subject to a far-field unit traction in the x direction is (Timoshenko and Goodier 1987, Dolbow and Belytschko 1999):

$$\begin{aligned}\sigma_{xx} &= 1 - \frac{a^2}{r^2} \left(\frac{3}{2} \cos(2\theta) + \cos(4\theta) \right) + \frac{3a^4}{2r^4} \cos(4\theta) \\ \sigma_{yy} &= -\frac{a^2}{r^2} \left(\frac{1}{2} \cos(2\theta) - \cos(4\theta) \right) - \frac{3a^4}{2r^4} \cos(4\theta) \\ \sigma_{xy} &= -\frac{a^2}{r^2} \left(\frac{1}{2} \sin(2\theta) + \sin(4\theta) \right) + \frac{3a^4}{2r^4} \sin(4\theta)\end{aligned}$$

where $a = 1$ is the hole radius, $r = \sqrt{x^2 + y^2}$ and $\theta = \arctan(y/x)$. The bounded upper quadrant shown in Figure 3.21 is used to solve the problem. Symmetry conditions are imposed in $x = 0$ and $y = 0$ and the tractions of the exact solution are considered in Γ .

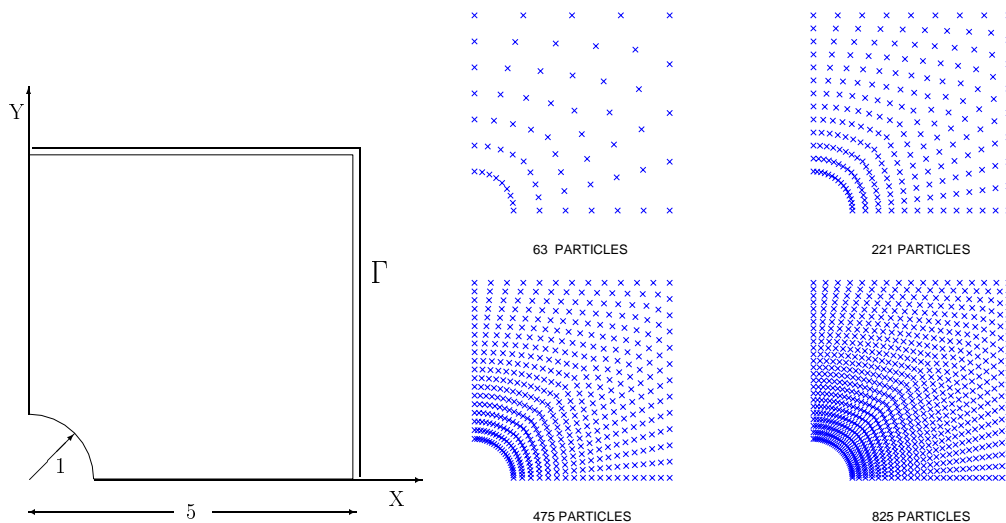
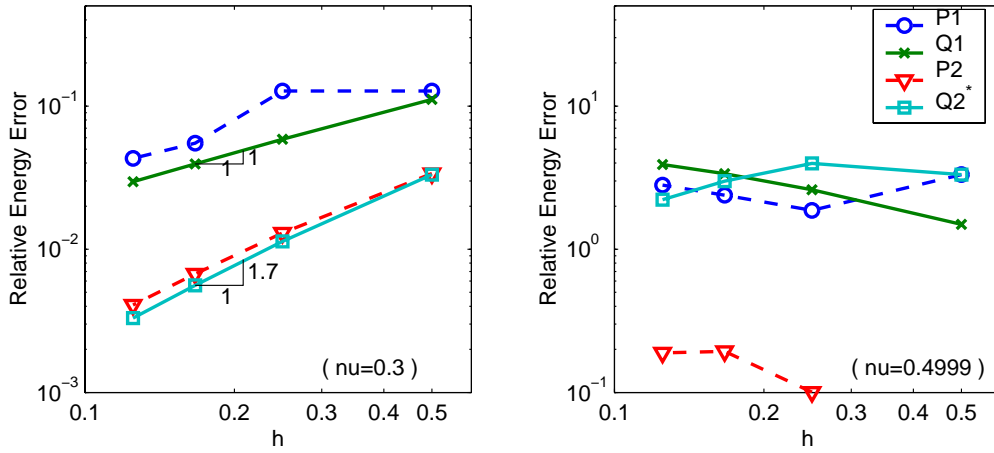
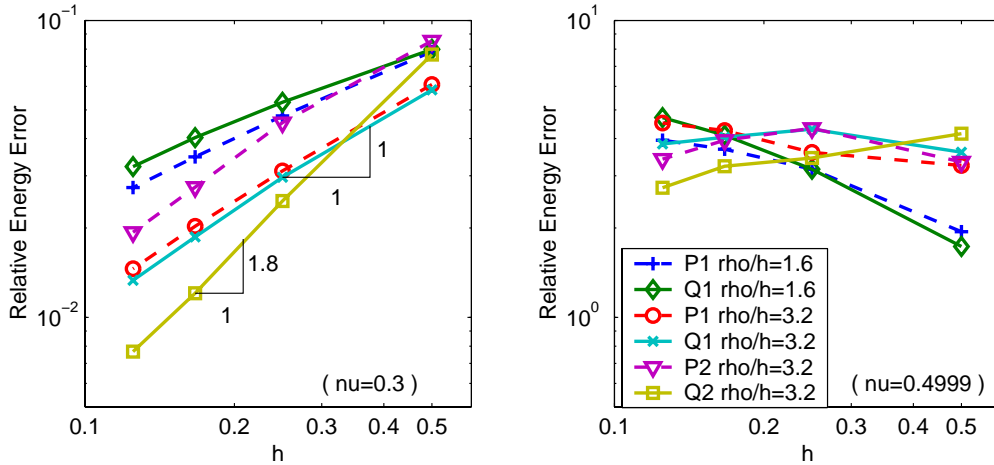


Figure 3.21: Problem statement for the plate with hole and discretizations.

Figure 3.22 shows the relative energy error with FE and $\nu = 0.3, 0.4999$. When $\nu = 0.3$ typical convergence results are obtained with all interpolations. However, all the FE interpolations, even the eight-noded FE (Q_2^*), suffer from locking when $\nu = 0.4999$. In this

Figure 3.22: FE, $\nu = 0.3$ (left) and $\nu = 0.4999$ (right)Figure 3.23: EFG, $\nu = 0.3$ (left) and $\nu = 0.4999$ (right)

example, there is a non-negligible projection of the solution in the space of non-physical locking modes, even for the $Q2^*$ FE. Similar results are obtained with EFG imposing consistency with several polynomial spaces. Two values of ρ/h are considered for the Q consistency. Again, the behaviour is independent of ρ/h . Better results are obtained with large ρ/h but locking effects are important in all cases. Near the incompressible limit, as in FE, good results can not be obtained with any of the interpolations.

3.4.3 The Prandtl's punch test

In this section a non-linear example is considered, the so-called *Prandtl's punch test* (Askes et al. 1999). A bilinear perfect elastoplastic material is considered and plane strain condi-

tions are assumed. The domain is shown in Figure 3.24.

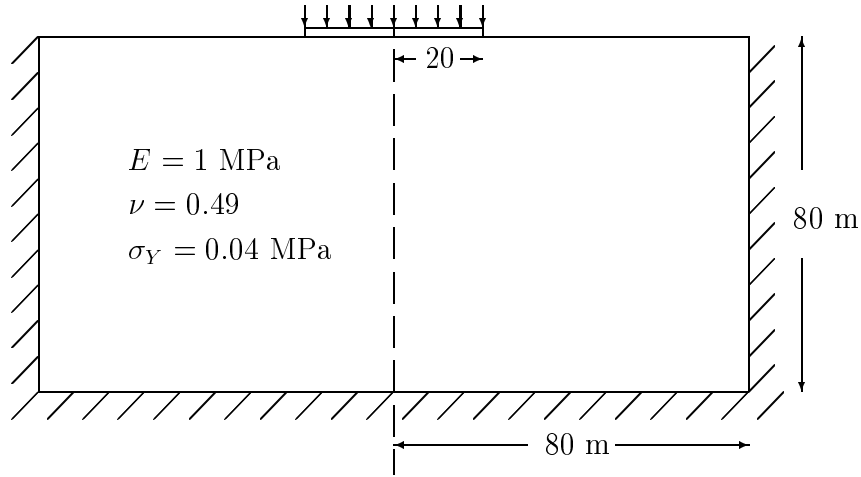


Figure 3.24: Prandtl's punch test: problem statement

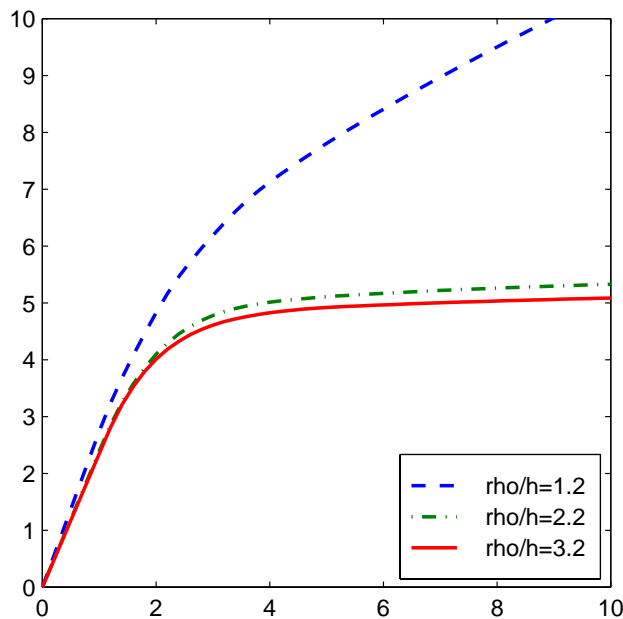


Figure 3.25: Load *versus* displacement with 9×9 particles, $m = 1$ and $\nu = 0.49$.

It has one axis of symmetry and only a half of the domain is discretized. The prescribed displacements are depicted in the same figure. The cubic spline is used for the weighting functions with rectangular supports. Lagrange multipliers have been used to impose the essential boundary conditions. Figures 3.25, 3.26, 3.27 and 3.28 show the evolution of the reaction force against the imposed displacement. The reaction force is normalized by the yield stress σ_Y and the area.

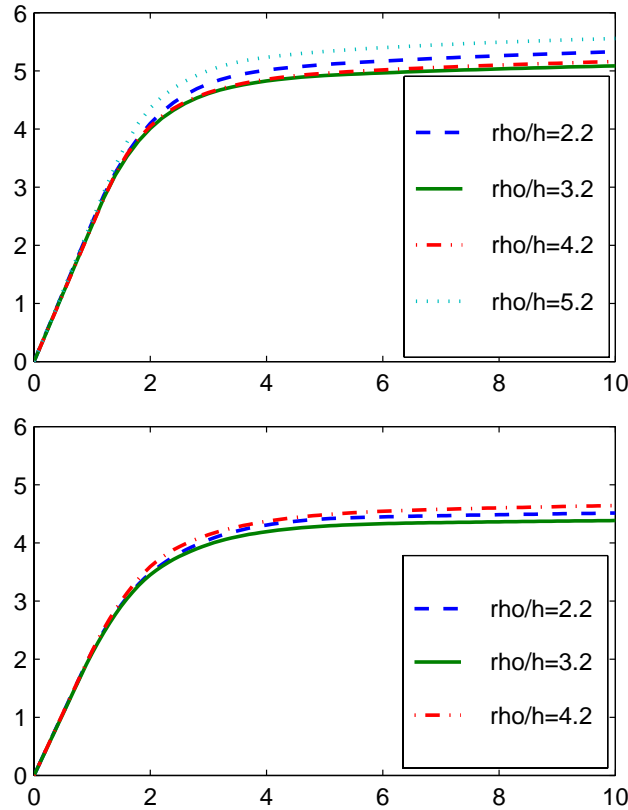


Figure 3.26: Load *versus* displacement with 9×9 (up) and 17×17 (down) particles, $m = 1$ and $\nu = 0.49$.

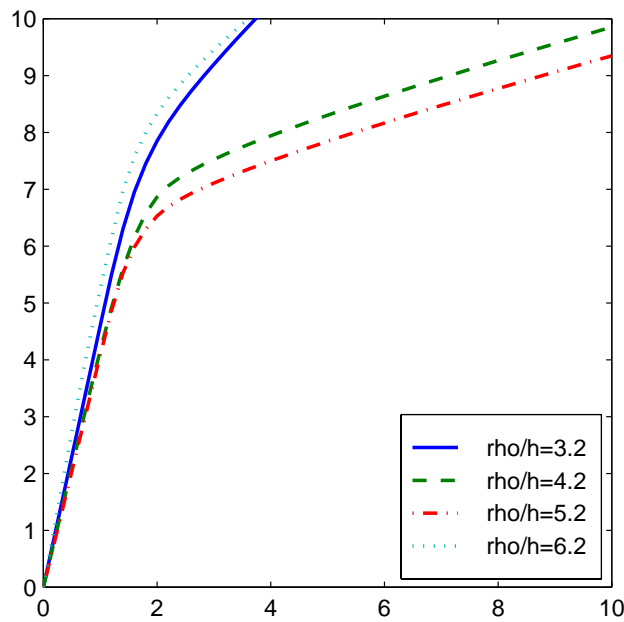
Figure 3.25 shows the solution obtained with EFG, imposing consistency in Q_1 , with a uniform distribution of 9×9 particles. As noted in (Askes et al. 1999), locking alleviates as ρ/h increases. Locking effects drastically degrade the solution when $\rho/h = 1.2$ (similar to Q1 FE), but a good solution can be obtained with $\rho/h = 3.2$. With these results, one could conclude: (1) there are no locking effects when ρ/h is large enough, and (2) locking effects decrease as ρ/h increases. Both conclusions would be false.

Figure 3.26 shows the results with several values of ρ/h . The best result is obtained still with $\rho/h = 3.2$ but locking effects increase if the ratio ρ/h is increased further. Similar results are obtained with a distribution of 17×17 particles. In both cases there are particles with no interaction with the boundary. Note that the solution is enhanced with the refinement due to the convergence of the interpolation. However, one can observe again an optimal value for the dilation parameter at $\rho/h = 3.2$. A summary of these results is shown in Table 3.5. Optimal values for ρ/h are emphasized with bold face.

Table 3.5 also includes the results obtained with a Poisson coefficient $\nu = 0.49999$.

Table 3.5: Load at the final displacement for the Prandtl's punch test.

| | 9 × 9 particles $\nu = 0.49$ | 17 × 17 particles $\nu = 0.49$ | 9 × 9 particles $\nu = 0.49999$ |
|----------------|---------------------------------|-----------------------------------|------------------------------------|
| $\rho/h = 2.2$ | 5.329 | 4.514 | 17.855 |
| $\rho/h = 3.2$ | 5.087 | 4.385 | 16.078 |
| $\rho/h = 4.2$ | 5.163 | 4.642 | 9.856 |
| $\rho/h = 5.2$ | 5.558 | 4.638 | 9.348 |
| $\rho/h = 6.2$ | 5.583 | 4.768 | 14.754 |

Figure 3.27: Reaction force vs displacement with 9 × 9 particles and $\nu = 0.49999$

The evolution of the reaction force *versus* the displacement close to the incompressible limit is shown in Figure 3.27. Now the optimal value for the dilation parameter is in the neighbourhood of $\rho/h = 5.2$. Nevertheless, the solution is excessively bad because of the locking effects for all values of ρ . The discretization must be refined in order to obtain an acceptable solution.

That is, an increase in the dilation parameter ρ can alleviate locking. However, it is not advisable to arbitrary increase the dilation parameter. An increase in the ratio ρ/h will induce a larger band-width with its corresponding increase in the computational cost. Moreover, in the examples, there is an optimal value for ρ/h that gives the best result: the solution degrades when ρ/h is larger than this optimal value. However, even at this optimal

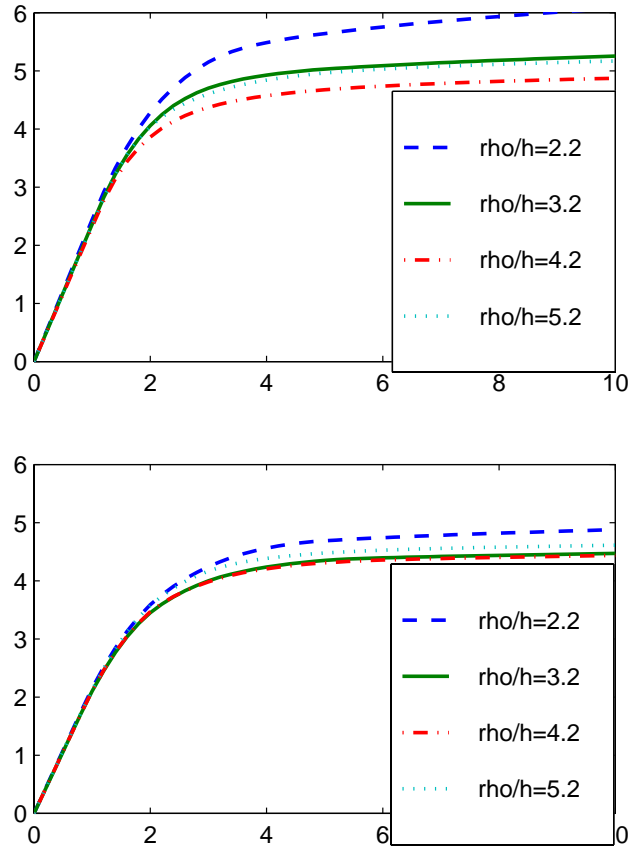


Figure 3.28: Load *versus* displacement with 9×9 (up) and 17×17 (down) particles, \mathcal{Q}_2 consistency and $\nu = 0.49$.

value the solution can be useless because of locking effects.

On the other hand, in this example, an increase in the order of consistency does not improve enough the solution. The non-physical locking modes for the \mathcal{Q}_2 consistency have an important component in the solution. Figure 3.28 shows the reaction force against the displacement with $\nu = 0.49$ and several values of ρ/h . Again there is an optimal value for the ratio ρ/h , now in the neighbourhood of $\rho/h = 4.2$.

3.5 Conclusions

A modal analysis has been used to study volumetric locking in EFG. The number of non-physical locking modes has been compared with equivalent finite element formulations. The influence of the ratio between the dilation parameter and the distance between particles, ρ/h has been studied independently of the consistency required. Finally some numerical exam-

ples have been used to corroborate the results of the modal analysis. The major conclusions are:

1. The number of non-physical locking modes is independent of the ratio ρ/h .
2. An increase of the dilation parameter decreases the eigenvalue (amount of energy) of the locking mode attenuating, but not suppressing, the volumetric locking (in the incompressible limit the same problems will occur).
3. An increase in the order of consistency decreases the number of non-physical locking modes.
4. The decrease in these non-physical locking modes is slower than in finite elements. Thus EFG will not improve the properties of FEM (from a volumetric locking viewpoint) when p or h - p refinement is enforced. However, for practical purposes and as in finite elements, in EFG an hp strategy will also suppress locking. Moreover, note that EFG incorporates an hp strategy in a simpler and more natural manner.

Chapter 4

Enrichment and Coupling of the Finite Element and Mesh-free Methods

4.1 Introduction

Mesh-free or particle methods have nowadays proven their applicability in computational mechanics, see Chapter 2 or (Liu, Belytschko and Oden 1996) for a general presentation. They do not require to generate a mesh (a connectivity matrix) and thus, they are specially suited for certain problems, for instance adaptive refinement computations or discontinuous field problems, i.e. crack propagation problems (Belytschko and Tabbara 1996). Moreover, the interpolation functions in mesh-free methods are particularly attractive in the presence of high gradients, concentrated forces, and large deformations.

On the other hand, from a practical point of view, finite elements are less costly, implement Dirichlet boundary conditions in a simple way (no need for Lagrange multipliers), and, above all, they are widely used and trusted by practitioners. However, the relative cost of the mesh generation process is, for some problems, very large. In particular, the cost of remeshing in adaptive refinement problems is clearly not negligible.

Several authors have already proposed to use mixed finite elements and mesh-free interpolations. The objective is always to use the advantages of each method. Belytschko et al. already show how to couple finite elements near the Dirichlet boundaries and element-free Galerkin in the interior of the computational domain, see (Belytschko et al. 1995). This simplifies considerably the prescription of essential boundary conditions. They do a mixed interpolation in the transition region: area where both finite elements and particles have an influence. This mixed interpolation requires the substitution of finite element nodes by

particles and the definition of ramp functions. Thus the transition is of the size of one finite element and the interpolation is linear. With the same objectives Hegen couples the finite element domain and the mesh-free region with Lagrange multipliers, see (Hegen 1996). Here a new formulation is proposed. It follows the ideas of Belytschko et al., generalizes them for any order of interpolation, suppresses the ramp functions, and does not require the substitution of nodes by particles. That is, as many particles as needed can be added where they are needed independently of the adjacent finite element mesh. This is done preserving the continuity of the solution and enforcing uniform consistency for the mixed interpolation.

Liu et al. propose a mixed interpolation with other goals and different formulations, see (Liu, Uras and Chen 97). They suggest to enrich the finite element approximation with particle methods. In fact, the following adaptive process seems attractive: (1) compute an approximation with a coarse finite element mesh, (2) do an *a posteriori* error estimation, and (3) improve the solution with particles without any remeshing process. Mesh-free methods are ideal for such a procedure.

In this chapter a unified and general formulation for mixed interpolations in both cases (coupling and enrichment) is presented. The formulation is developed for the EFG method. However, its generalization to other particle methods is straightforward.

In the following sections the formulation is developed, the applicability conditions are discussed and the convergence properties are presented. Finally several examples are presented to illustrate the advantages of such a mixed approximation.

4.2 A hierarchical mixed approximation: finite elements with EFG

Suppose, as discussed in the introduction, that the interpolation of $u(x)$ in Ω , $\Omega \subset \mathbb{R}^n$, is done with both finite elements and EFG. The domain must include a set of nodes $\{x_i\}_{i \in I^h}$ with their associated shape functions $N_i^h(x)$, that are going to take care of the finite element contribution, $u^h(x)$, to $u(x)$, namely,

$$u^h(x) = \sum_{i \in I^h} u(x_i) N_i^h(x). \quad (4.2.1)$$

There is also a set of particles $\{x_j\}_{j \in I^\rho}$ with their associated interpolation functions $N_j^\rho(x)$, that are going to take care of the mesh-free contribution,

$$u^\rho(x) = \sum_{j \in I^\rho} u(x_j) N_j^\rho(x). \quad (4.2.2)$$

In the more general case, the domain Ω is the union of two non-disjoint subdomains, $\Omega = \Omega^h \cup \Omega^\rho$, where Ω^h denotes the subdomain where the N_i^h have an influence in the approximation,

$$\Omega^h = \{x \in \Omega / \exists i \in I^h \quad N_i^h(x) \neq 0\},$$

and where Ω^ρ is the subdomain where at least one N_j^ρ is non zero,

$$\Omega^\rho = \{x \in \Omega / \exists j \in I^\rho \quad N_j^\rho(x) \neq 0\}.$$

In the region where only finite elements are present, $\Omega^h \setminus \Omega^\rho$, a standard, and thus consistent, finite element approximation is considered:

$$u(x) \simeq u^h(x).$$

In the region where only particles have an influence, $\Omega^\rho \setminus \Omega^h$, the standard, and thus consistent, EFG approximation is considered:

$$u(x) \simeq u^\rho(x).$$

However, in the area where both interpolations have an influence, $\tilde{\Omega} := \Omega^h \cap \Omega^\rho$, a mixed interpolation must be defined

$$u(x) \simeq u^h(x) + u^\rho(x). \quad (4.2.3)$$

The objective now is to develop a mixed functional interpolation, such as (4.2.3), with the desired consistency in $\tilde{\Omega}$, without any modification of the finite element shape functions N_i^h and such that $u^\rho(x)$ is hierarchical. That is, an EFG contribution which should be zero at the finite element nodes, must be added to the standard finite element interpolation. Obviously, such a contribution must verify consistency conditions similar to those of standard mesh-free methods see section 2.1.2

In the following sections this mixed interpolation is developed and discussed. In particular, the admissible particle distribution is detailed. Moreover, *a priori* convergence is studied when the number of particles is increased, when the number of nodes is increased, and when both particles and nodes are increased.

Moreover, two cases will be considered with the same formulation. The first one (**Coupled Finite Element and Element-Free Galerkin**) requires that $\Omega^h \neq \Omega$ and $\Omega^\rho \neq \Omega$. That is, in a region of Ω only finite elements will be used, in another region only EFG are employed, and finally in a mixed area, $\tilde{\Omega}$, the solution is approximated using (4.2.3). In the second case, $\Omega = \Omega^h$ and $\tilde{\Omega} = \Omega^\rho$. That is, there is a complete finite element basis

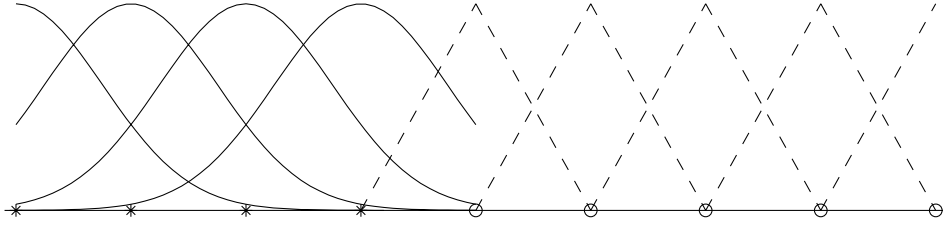


Figure 4.1: Coupled Finite Element and Element-Free Galerkin

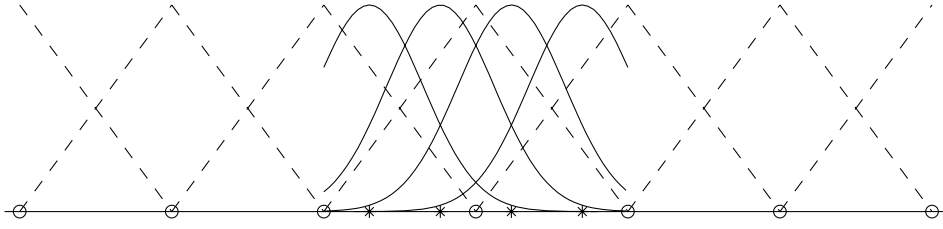


Figure 4.2: Finite Element Enrichment with Element-Free Galerkin

all over Ω . Only in a reduced area, $\tilde{\Omega}$, particles are added to improve the interpolation (**Finite Element Enrichment with Element-Free Galerkin**). Both situations are depicted in figures 4.1 and 4.2, and developed in sections 4.3 and 4.4.

4.2.1 Evaluation of the mesh-free shape functions N_j^ρ

In $\tilde{\Omega}$ the expression of the interpolation function is obtained after substitution of (4.2.1) and (4.2.2) into (4.2.3), namely

$$u(x) \simeq \sum_{i \in I^h} u(x_i) N_i^h(x) + \sum_{j \in I^\rho} u(x_j) N_j^\rho(x). \quad (4.2.4)$$

Where $N^\rho(x)$ is defined, as in standard EFG:

$$N_j^\rho(x) = \boldsymbol{\alpha}^T(x) \mathbf{P}\left(\frac{x-x_j}{\rho}\right) \phi\left(\frac{x-x_j}{\rho}\right), \quad (4.2.5)$$

The vector of unknown functions, $\boldsymbol{\alpha}(x)$, is determined using the consistency condition. Now the reproducibility conditions impose that (4.2.4) must interpolate exactly a complete basis of polynomials of order less or equal to m . That is,

$$\mathbf{P}(0) = \sum_{j \in I^\rho} \mathbf{P}\left(\frac{x-x_j}{\rho}\right) N_j^\rho(x) + \sum_{i \in I^h} \mathbf{P}\left(\frac{x-x_i}{\rho}\right) N_i^h(x), \quad (4.2.6)$$

which is the natural extension of (2.1.32). Note that, if ρ is constant everywhere, equation (4.2.6) can be rewritten as

$$\mathbf{P}(x) = \sum_{j \in I^\rho} \mathbf{P}(x_j) N_j^\rho(x) + \sum_{i \in I^h} \mathbf{P}(x_i) N_i^h(x), \quad (4.2.7)$$

which shows more clearly the desired reproducibility condition. The linear system of equations that determines α is obtained once the definition of $N^\rho(x)$, equation (4.2.5), is substituted in (4.2.6).

$$\mathbf{M}(x) \alpha(x) = \mathbf{P}(0) - \sum_{i \in I^h} \mathbf{P}\left(\frac{x - x_i}{\rho}\right) N_i^h(x). \quad (4.2.8)$$

The least squares matrix is identical to the matrix employed in the standard EFG method, Eq. (2.1.34).

Remark 4.2.1. The particle shape functions N_j^ρ are hierarchical. Note that at any node x_k , $k \in I^h$, the right hand side of (4.2.8) is zero,

$$\mathbf{P}(0) - \sum_{i \in I^h} \mathbf{P}\left(\frac{x_k - x_i}{\rho}\right) N_i^h(x_k) = \mathbf{P}(0) - \sum_{i \in I^h} \mathbf{P}\left(\frac{x_k - x_i}{\rho}\right) \delta_{ik} = \mathbf{0}.$$

Thus, the solution of (4.2.8) is trivial, $\alpha(x_k) = \mathbf{0}$. And therefore, from the definition of the particle shape functions, (4.2.5), it is easy to verify that the $N_j^\rho(x)$ are hierarchical, i.e. $N_j^\rho(x_k) = 0 \quad \forall j \in I^\rho, k \in I^h$.

Remark 4.2.2 (Admissible particle distributions). As in standard EFG, matrix $\mathbf{M}(x)$ must be regular (invertible) everywhere, i.e. at each point $x \in \tilde{\Omega}$. Only the right hand side of (4.2.8) differs from the EFG system of equations, Eq. (2.1.33). Thus, as in EFG, the number of particles, their position and their related dilation parameters can not be taken arbitrarily. The restrictions presented in remark 2.1.11 for the particle distribution in EFG, are also valid for possible distributions of particles in a mixed interpolation. For instance, in a one-dimensional domain with an order one consistency (linear interpolation) a finite element node can not be replaced by a single particle, see figure 4.3. Two particles, with dilation parameters large enough, are needed in order to ensure that everywhere in $\tilde{\Omega}$ the scalar product, (2.1.35), does not degenerate. Figures 4.3 and 4.4 depict these situations. For each particle, its corresponding weighting function $\phi\left(\frac{x-x_i}{\rho}\right)$ is plotted. Figure 4.5 also shows a non admissible distribution of particles. In the region where both particle and finite element interpolations have an influence, $\tilde{\Omega}$, there are not enough particles (only one is present) to ensure the regularity of $\mathbf{M}(x)$. An obvious solution for this problem, maintaining the same particle distribution, is to chose a dilation parameter large enough, see figure 4.6.

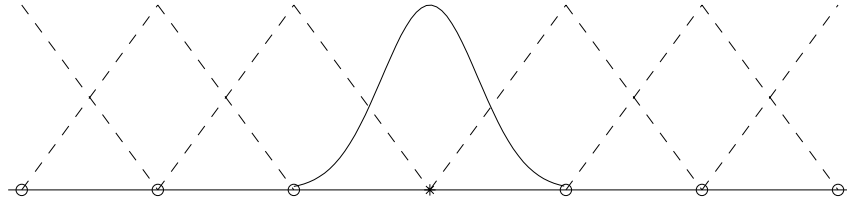


Figure 4.3: Substitution of a finite element node by one particle. Non admissible distribution.

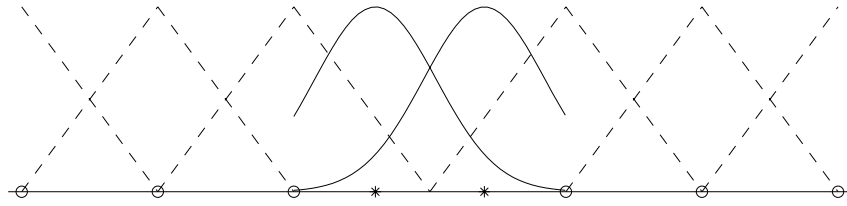


Figure 4.4: Substitution of a finite element node by two particles. Admissible distribution.

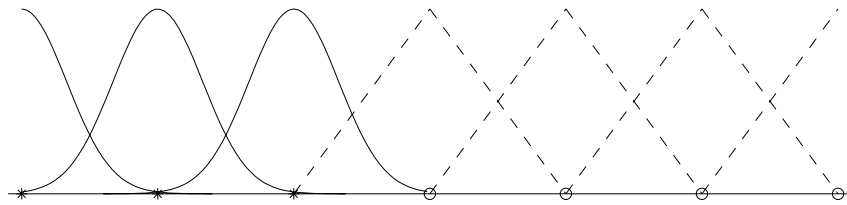


Figure 4.5: Non admissible distribution. $\tilde{\Omega}$ is under the influence of only one particle.

Remark 4.2.3. The shape functions N_j^p are hierarchical. Thus, in one dimension, the weighting functions $\phi(\frac{x-x_i}{\rho})$ can be truncated outside Ω^p and continuity of $N_j^p(x)$ is preserved, see figures 4.4 and 4.6. This property can not be generalized to higher dimensions. In fact sections 4.3 and 4.4 discuss this issue.

Remark 4.2.4. As previously indicated for EFG, in section 2.1.2, the interpolation functions could be defined using (2.1.27) instead of (4.2.5). However, it is preferable to scale the polynomials $\mathbf{P}(x)$ as done previously, because Gram matrices, such as \mathbf{M} , are easily ill-conditioned, specially with the trivial basis of polynomials. In general, with the translation to x and the scaling with ρ , Gram matrices have lower condition numbers.

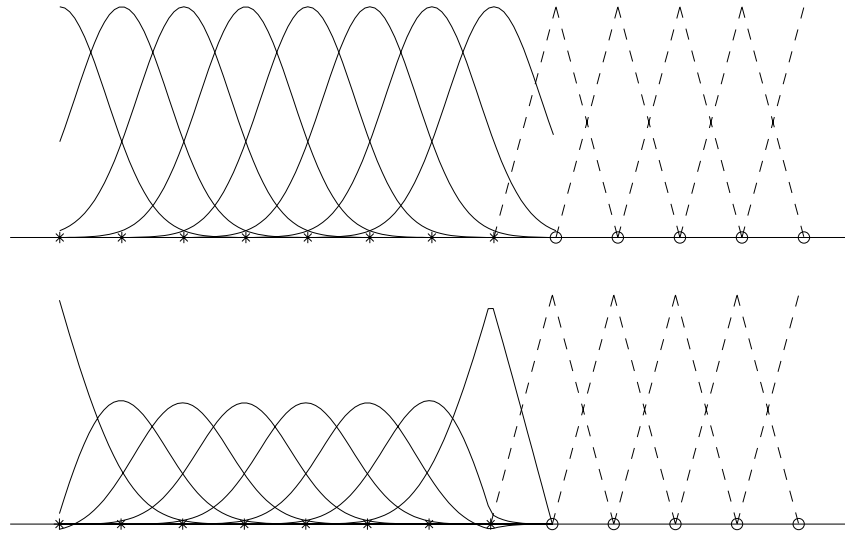


Figure 4.6: Approximation functions before and after imposing the consistency condition of order one.

4.3 Coupled Finite Element and Element-Free Galerkin

In this section, a new formulation, which generalizes the coupled formulation proposed by Belytschko et al. (1995) is presented. This coupling between finite elements and EFG maintains both continuity and consistency everywhere, in particular, in the transition area. The major differences with the previously cited reference are: (1) there is no need to replace nodes by particles, and (2) no ramp functions must be defined.

In fact, the generalization proposed here can be used for any order of consistency (it can go beyond linear elements and order one consistency). Moreover, this method allows to introduce as many particles as desired in the last element that defines the transition area, see figures 4.7 and 4.8.

The computational domain Ω is divided in three non disjoint regions: one where finite elements have an influence, Ω^h , another where particles have an influence, Ω^p , and finally, one region, $\tilde{\Omega}$, for the transition. In the latter, both particles and nodes define the interpolation, see figure 4.1. Such a situation may be of interest if a computation with finite elements of degree p needs to be refined in a region Ω^p without remeshing. The nodes of the original finite element mesh are removed in Ω^p but as many particles as needed are added in that region (see the crack propagation examples in the papers by Belytschko and coworkers (Belytschko et al. 1995, Belytschko and Organ 1997, Belytschko and Tabbara 1996, Organ, Fleming, Terry and Belytschko 1996)).

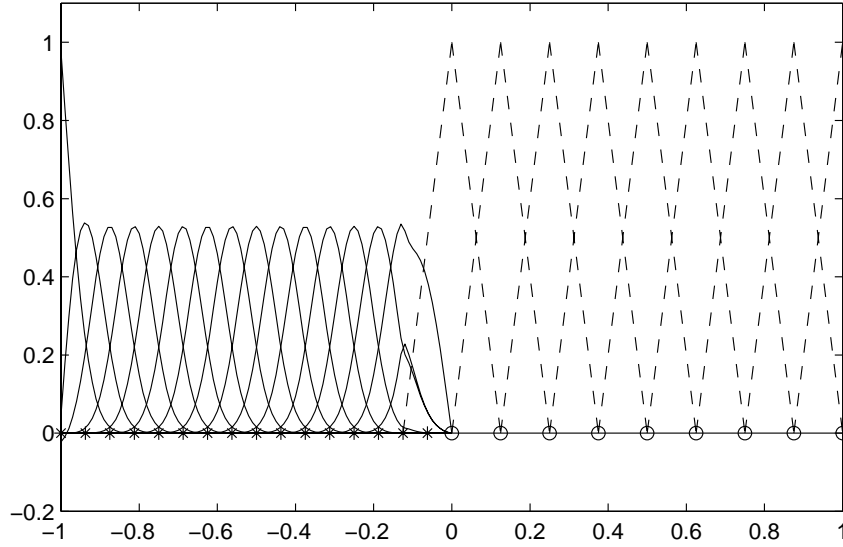


Figure 4.7: Coupled approximation functions with consistency of order one and two particles in the transition region $\tilde{\Omega}$.

It is important to notice that the approximation $u^h + u^p$ is continuous everywhere in Ω if the following conditions are met. First, the same order of consistency is imposed all over Ω (i.e. for both finite elements and particles), namely, $m = p$. And second, the domain of influence of particles, Ω^p , coincides exactly with the region where finite elements do not have a complete basis. That is, no particles are added in “complete” finite elements (i.e. elements where no node has been suppressed). Moreover, weighting functions ϕ are chopped off in those “complete” finite elements, see figure 4.6. In other words, Ω^p is the union of elements where at least one node has been removed.

The approximation $u^h + u^p$ is continuous as long as the shape functions N_j^p are continuous. In spite of chopping off the weighting functions outside Ω^p the approximation maintains its regularity. This is due to the fact that $N_j^p(x) = 0$ over $\Omega^h \cap \partial\Omega^p$, with absolute independence of the fact that $\phi(\frac{x-x_i}{\rho}) \neq 0$ over $\Omega^h \cap \partial\Omega^p$.

In $\Omega^h \setminus \Omega^p$ the finite element interpolation is complete and of order m . In particular, over $\Omega^h \cap \partial\Omega^p$ polynomials of degree less or equal to m are interpolated exactly. Thus, it is easy to verify that

$$\mathbf{P}(0) - \sum_{i \in I^h} \mathbf{P}\left(\frac{x-x_i}{\rho}\right) N_i^h(x) = \mathbf{0} \quad \text{over } \Omega^h \cap \partial\Omega^p.$$

Recalling (4.2.8), the previous equation implies that $\alpha(x) = \mathbf{0}$, and consequently, $N_j^p(x) = 0$ for $x \in \Omega^h \cap \partial\Omega^p$, see equation (4.2.5). Note that the previous rationale is independent

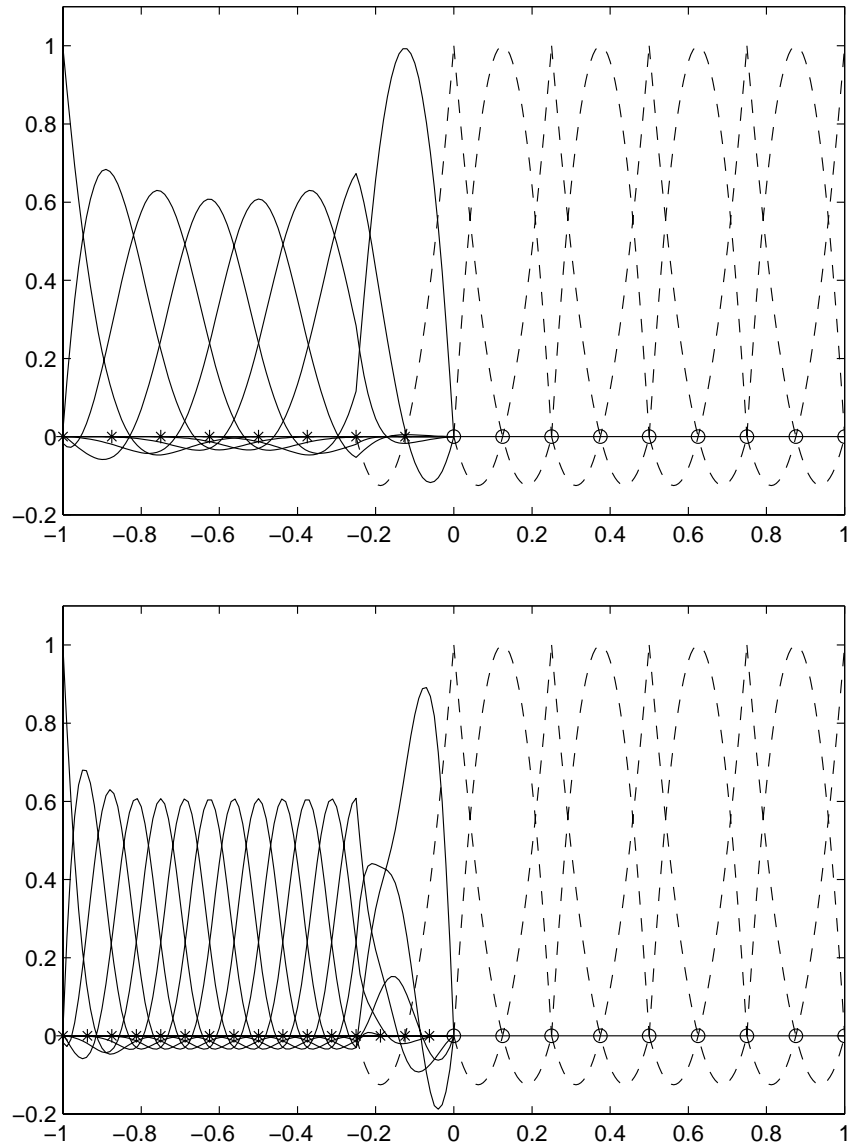


Figure 4.8: Coupled approximation functions with consistency of order two and two different distributions of particles.

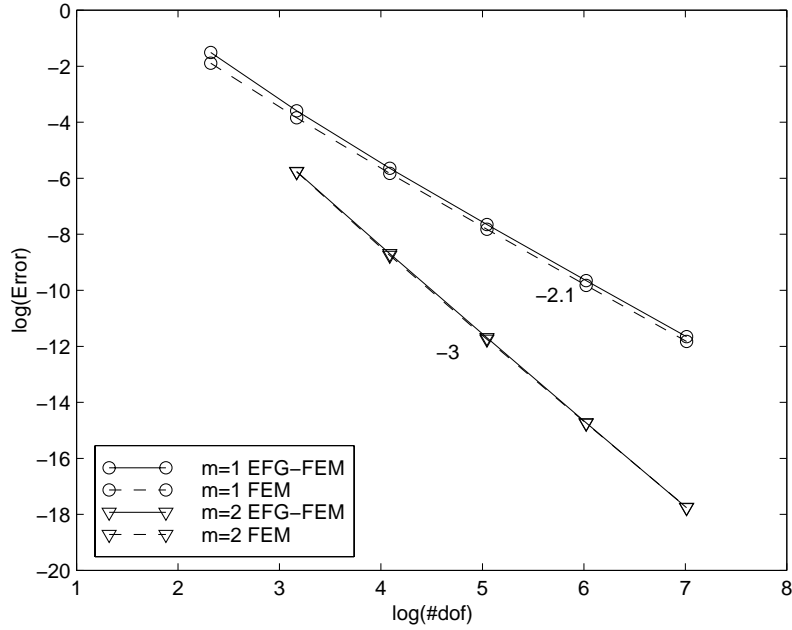


Figure 4.9: Convergence of FEM and coupled FEM-EFG for a distribution of elements and particles shown in figure 4.6.

of the spatial dimensions. Thus, in 1D, 2D or 3D, the shape functions N_j^ρ are continuous independently of the truncation of the weighting functions $\phi(\frac{x-x_i}{\rho})$, see figure 4.6.

Remark 4.3.1. In $\Omega^\rho \setminus \Omega^h$ finite elements have no influence,

$$\mathbf{P}(0) - \sum_{i \in I^h} \mathbf{P}\left(\frac{x-x_i}{\rho}\right) N_i^h(x) = \mathbf{P}(0).$$

In this region, shape functions N_j^ρ are identical to the standard EFG ones.

Convergence analysis. It is easy to verify that the mixed interpolation proposed preserves the convergence rate of FEM and EFG. Function

$$u(x) = x^4 + 2x^3 \quad \text{is interpolated for } x \in \bar{\Omega} = [-1, 1].$$

The three regions of influence of finite elements, particles and the mixed interpolation are: $\Omega^h = [-h, 1]$, $\Omega^\rho = [-1, 0]$ and $\tilde{\Omega} = [-h, 0]$, where h is the size of finite elements, see figure 4.6.

Figure 4.9 shows the convergence rate —logarithm of the error in $L^2([-1, 1])$ versus the total number of degrees of freedom— in two cases: standard linear finite elements and a coupled finite element–EFG approximation of order one. With this distribution of particles and with consistency of order one, this approach gives the same results as the one proposed

by Belytschko et al. (1995). Similar conclusions can be drawn with other distributions of particles and order of consistency, see in the same figure the convergence results obtained with $m = 2$ and a particle distribution of figure 4.8.

4.4 Finite Element enrichment with Element-Free Galerkin

A finite element approximation can be improved (enriched) without any need of remeshing by adding particles. Particle methods have demonstrated their advantages in adaptive computations and their suitability to capture large gradients, concentrated loads and large deformations. Thus enrichment of finite elements with mesh-free methods of the desired order seems a attractive option in these problems.

In this case, the region $\tilde{\Omega}$ where particles are added also maintains the original complete finite element interpolation, see figure 4.2. In $\tilde{\Omega}$, the consistency of the mixed interpolation m must be larger than the order of the finite element interpolation p . If consistency is set equal to p , finite elements can reproduce exactly polynomials up to degree p , thus

$$\mathbf{P}(0) - \sum_{i \in I^h} \mathbf{P}\left(\frac{x - x_i}{\rho}\right) N_i^h(x) = \mathbf{0} \quad \forall x \in \tilde{\Omega},$$

and the solution of (4.2.8) is the trivial one, $\alpha = \mathbf{0}$. Consequently, the interpolation functions related to the particles N_j^p are identically zero everywhere. Thus $\mathbf{P}(x)$ must include at least one polynomial not reproducible by the finite element interpolation, i.e. $m > p$.

As previously seen in section 4.2 the shape functions N_j^p are hierarchical. Thus the interpolation is continuous in one dimensional problems irrespectively of the truncation of the weighting functions, $\phi(x)$ outside $\tilde{\Omega}$. In higher dimensions, continuity is not preserved as soon as the order of consistency is not constant and uniform everywhere in Ω . In fact, the increase in consistency just mentioned in $\tilde{\Omega}$ will induce discontinuities in the approximation along $\partial\tilde{\Omega}$: functions N_j^p are hierarchical but do not go to zero everywhere on $\partial\tilde{\Omega}$. If the approximation must be continuous a region surrounding $\tilde{\Omega}$ must be defined in which the interpolation functions N_j^p go to zero with continuity. However, if $\partial\tilde{\Omega}$ coincides with an area where finite elements capture accurately the solution, those discontinuities due to the enrichment are going to be small.

Remark 4.4.1. Linear elements in 1D reproduce exactly polynomials of degree less or equal to one. In this case the first two equations of the system of equations (4.2.8) are the consistency conditions:

$$\sum_{j \in I^p} N_j^p(x) = 0, \quad \sum_{j \in I^p} x_j N_j^p(x) = 0.$$

Which correspond to the first two equations in (4.2.7). This implies that all the interpolation functions N_j^p must verify these relations and, thus, they are no longer linearly independent. If every interpolation function is used in the resolution of the boundary value problem, the “stiffness” matrix would be singular (two of its eigenvalues are zero). Thus, once the shape functions are evaluated, i.e. after (4.2.8) is solved, two of those interpolation functions are eliminated. Then, a linear set of interpolation functions is recovered and the “stiffness” matrix remains regular. In general, it is necessary to suppress a N_j^p (i.e. a particle) of the interpolation set for each polynomial in $\mathbf{P}(x)$ that finite elements are able to capture exactly.

Convergence analysis. A parametric analysis of convergence rates for this proposed method is shown next. The same function used previously is also used here,

$$u(x) = x^4 + 2x^3 \quad x \in \bar{\Omega} = [-1, 1]$$

with particles and finite elements everywhere. Finite elements are enriched everywhere adding particles and increasing the order of consistency. As before, p is the degree of the finite element interpolation, and m is the order of consistency obtained with the added particles. The increment of consistency q is defined as

$$q := m - p.$$

The error is evaluated in the $L^2(\Omega)$ norm. In figure 4.10 the logarithm of the error is plotted against the logarithm of the number of degrees of freedom for different values of p and q . Here, both finite element and mesh-free approximations are refined simultaneously (maintaining h/ρ constant). Note that the order of the method is $\mathcal{O}(h^{m+1})$. It is the same order that can be obtained with standard finite elements of degree $m = p + q$, or standard EFG with consistency of order m .

Figure 4.11 shows convergence results when the number of particles is kept constant but elements are refined. The order of the method is $\mathcal{O}(h^{p+1})$ (identical to the order of finite elements alone) if the constant ρ is large (four particles in Ω). However, when the number of particles increases (256 particles in Ω), i.e. small ρ , the order becomes $\mathcal{O}(h^{m+1})$. Thus, if the density of particles is large, a refinement in finite elements of degree p induces an order of convergence similar to finite elements of degree $m = p + q$.

Finally, figure 4.12 shows the rate of convergence when refinement is only based on particles. That is, the finite element mesh is kept constant. If the element size, h , is small, the order observed is $\mathcal{O}(\rho^p)$, but when the element size is large (four elements in Ω) the mixed approximation does not converge as ρ goes to zero.

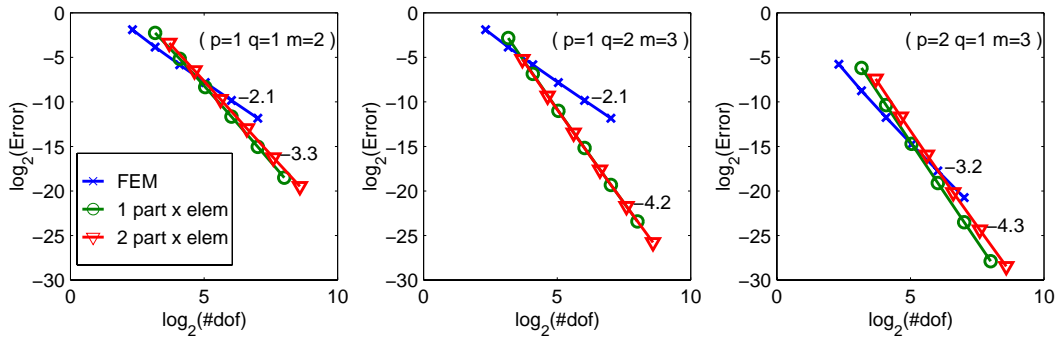


Figure 4.10: Convergence for a mesh and mesh-free refinement: constant h/ρ and $h \rightarrow 0$

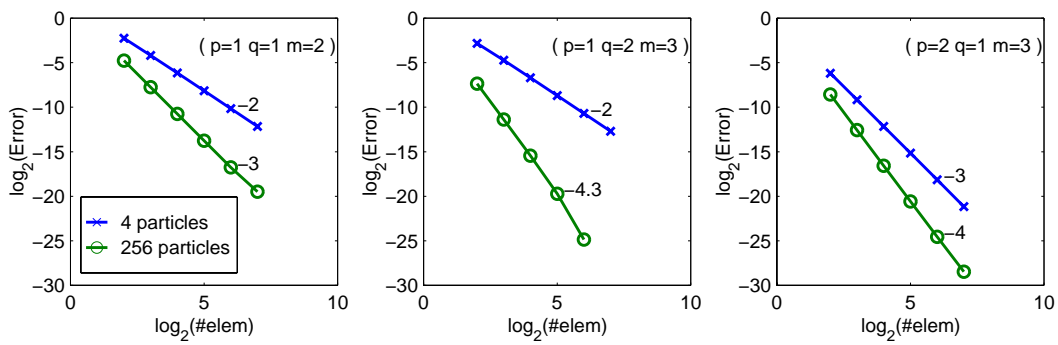


Figure 4.11: Convergence for a mesh refinement: constant ρ and $h \rightarrow 0$

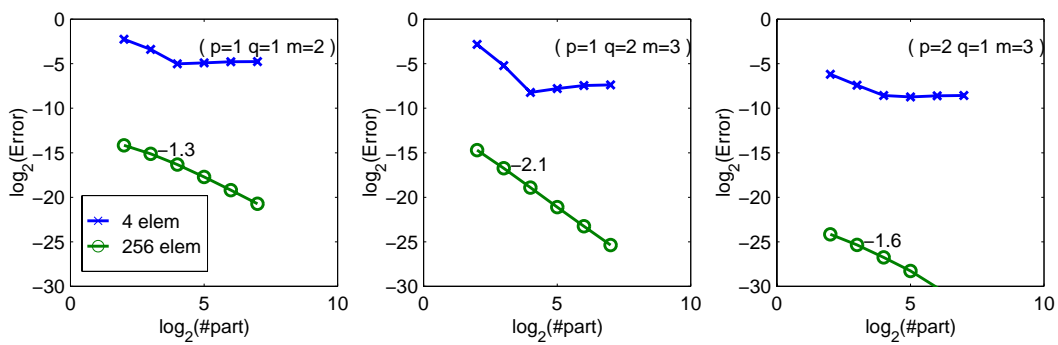


Figure 4.12: Convergence for a mesh-free refinement: constant h and $\rho \rightarrow 0$

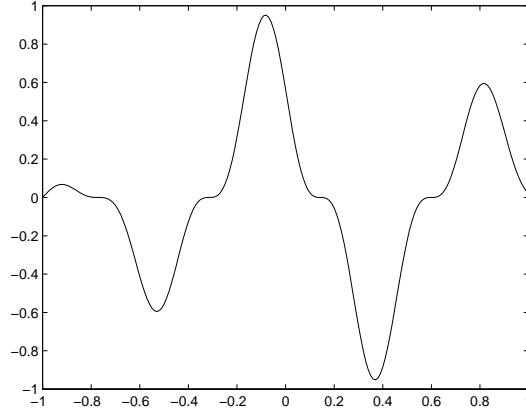


Figure 4.13: Function $u(x)$ defined in (4.4.1)

Remark 4.4.2. Note that this convergence rates are also obtained with functions other than polynomials. In particular, similar results are obtained with the following function

$$u(x) = \sin\left(\frac{7}{6}\pi(x+1)\right) \cos^3\left(\frac{35}{6}\pi(x+1)\right) \quad (4.4.1)$$

which is plotted in figure 4.13.

In fact, this convergence analysis can be further exploited. An *a priori* error estimate can be obtained for the mixed approximation proposed in this section.

Theorem 4.4.1. *Let m be the order of consistency of the mixed approximation $u^h + u^\rho$, such that $m = p + q$, where p is the order of the finite element approximation, u^h , and $q > 0$ is the order increment due to u^ρ . Suppose the following regularity conditions hold for the exact solution, u , and the weighting function, ϕ : $u \in C^{m+1}(\overline{\Omega})$ and $\phi \in C^0(\overline{\Omega})$, where Ω is bounded and $\partial\Omega$ is smooth. Finally, assume that the element size is small enough, i.e.*

$$\frac{h}{\rho} \leq \min_{p+1 \leq r \leq m} \binom{r}{p+1}^{\frac{-1}{r-(p+1)}}.$$

Then,

$$\|u - (u^h + u^\rho)\|_{\mathcal{L}^\infty} \leq h^{p+1} [C_1 h^q + C_2 \rho^q] |u|_{\mathcal{W}_\infty^{m+1}} \quad (4.4.2)$$

where C_1 and C_2 are independent of the finite element size, h , and the dilation parameter, ρ , of the mesh-free approximation.

Note that on the left hand side of the inequality the standard infinite norm over Ω is used, whereas on the right hand side the seminorm $|\cdot|_{\mathcal{W}_\infty^{m+1}}$ is employed. For the sake of

clarity, multi-index notation is introduced: given the n -tuple $\alpha = (\alpha_1, \alpha_2, \dots, \alpha_n) \in \mathbb{N}^n$ and the non-negative integer $|\alpha| := \alpha_1 + \alpha_2 + \dots + \alpha_n$ then, by definition,

$$|u|_{\mathcal{W}_{\infty}^{m+1}} = \sum_{|\alpha|=m+1} \max_{x \in \bar{\Omega}} \left| \frac{\partial^{|\alpha|} u}{\partial x_1^{\alpha_1} \partial x_2^{\alpha_2} \dots \partial x_n^{\alpha_n}} \right|.$$

It is important to remark that the error bound in (4.4.2) coincides with the convergence results shown in figures 4.10, 4.11 and 4.12. That is, when both h and ρ decrease simultaneously, the order of convergence is $p+q+1 = m+1$. When h goes to zero while ρ is kept constant, the order is either $p+1$ if $C_1 h^q < C_2 \rho^q$ or $m+1$ when $C_1 h^q \gg C_2 \rho^q$. And finally, convergence is ensured at a rate of q when ρ goes to zero provided that $C_1 h^q \ll C_2 \rho^q$.

The previous theorem introduces a restriction on the element size which can be relaxed at a prize of obtaining a new error bound not as sharp.

Theorem 4.4.2. *Under the same assumptions of **Theorem 4.4.1** but with no restriction on the element size, the a priori error bound becomes:*

$$\|u - (u^h + u^\rho)\|_{\mathcal{L}_{\infty}} \leq h^{p+1} [C_1 h^q + C_2 \rho^q] |u|_{\mathcal{W}_{\infty}^{m+1}},$$

where C_1 and C_2 are independent of the finite element size, h , and the dilation parameter, ρ , of the mesh-free approximation.

See appendix A for a detailed proof of the previous theorems. Moreover, following the ideas exposed in (Liu et al. 1997) **Theorem 4.4.1** can be extended to the standard form in finite element analysis.

Theorem 4.4.3. *Let m be the order of consistency of the mixed approximation $u^h + u^\rho$, such that $m = p+q$, where p is the order of the finite element approximation, u^h , and $q > 0$ is the order increment due to u^ρ . Given ℓ such that $0 \leq \ell \leq p$, suppose the following regularity conditions hold for the exact solution, u , and the weighting function, ϕ : $u \in C^{m+1}(\bar{\Omega})$ and $\phi \in C^{\ell}(\bar{\Omega})$, where Ω is bounded and $\partial\Omega$ is smooth. Finally, assume that the element size is small enough, i.e.*

$$h/\rho \leq \min_{0 \leq k \leq \ell} Q_k$$

where

$$Q_k := \begin{cases} 1 & \text{for } m = p+1, \\ \min_{r=p+2, \dots, m} \left(\frac{\lambda_{k,p+1}}{\lambda_{k,r}} \right)^{\frac{1}{r-(p+1)}} & \text{for } m > p+1. \end{cases}$$

and

$$\lambda_{k,r} := \frac{r!}{(r-k)!} \sum_{l=\max\{k-r+p+1,0\}}^k \binom{k}{l} \binom{r-k}{p+1-l}.$$

Then, for $k = 0, \dots, \ell$

$$\|u - (u^h + u^\rho)\|_{\mathcal{W}_\infty^k} \leq h^{p+1-k} [C_1 h^q + C_2 \rho^q] |u|_{\mathcal{W}_\infty^{m+1}} \quad (4.4.3)$$

where C_1 and C_2 are independent of the finite element size, h , and the dilation parameter, ρ , of the mesh-free approximation.

The standard definition of the norm $\|\cdot\|_{\mathcal{W}_\infty^k}$ is used, namely

$$\|u\|_{\mathcal{W}_\infty^k} = \sum_{s=0}^k |u|_{\mathcal{W}_\infty^s} = \sum_{s=0}^k \sum_{|\alpha|=s} \max_{x \in \tilde{\Omega}} \left| \frac{\partial^{|\alpha|} u}{\partial x_1^{\alpha_1} \partial x_2^{\alpha_2} \dots \partial x_n^{\alpha_n}} \right|.$$

4.5 Numerical examples

4.5.1 Coupled EFG-FEM

In this section a coupled FE-EFG approximation is employed with a simple example, the interpolation of $u(x) = \sin(\pi x)$ in $\Omega = [-1, 1]$. Linear elements are employed ($p = 1$) and the nodes in $\Omega^\rho = [-1, 0)$ are replaced by particles. Consistency of order one is enforced everywhere.

Figure 4.14 shows, on the left, the interpolation functions. The shape functions, N^ρ , associated to particles, denoted by asterisks, are plotted with a solid line. The finite element interpolation functions, N^h , are depicted with dashed lines and the position of the nodes by circles. The transition region $\tilde{\Omega}$ is $[-0.25, 0]$. Figure 4.14 also shows, on the right, the result of such an interpolation. The approximation $u^h + u^\rho$ is plotted with a solid line and the error, $u - (u^h + u^\rho)$, with a dashed line. It is important to notice the special profile adopted by the shape function associated to the first particle (particle at $x = -0.25$): on the left it is similar to the particle positioned at the boundary of the domain, while in $\tilde{\Omega}$ it looks like a standard linear finite element interpolation function.

In this case the approximation is similar to the one proposed in (Belytschko et al. 1995). However, here there is no need to define any ramp function. Moreover, the same formulation can be employed with a particles distribution such that the transition region $\tilde{\Omega}$ includes more than one particle. For instance, figure 4.15 shows both the shape functions and the interpolation with its associated error for a different distribution of particles. In particular,

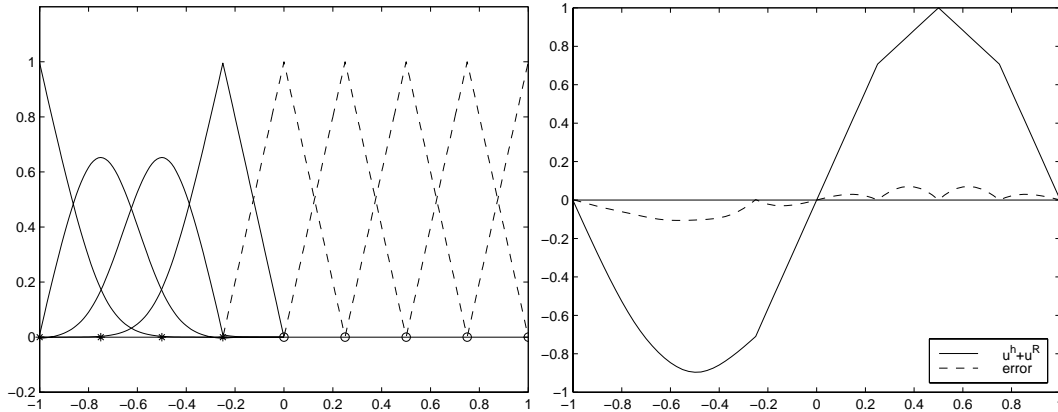


Figure 4.14: Approximation functions —4 particles and 5 nodes— (left) and interpolation result, $u^h + u^R$, with error distribution (right).

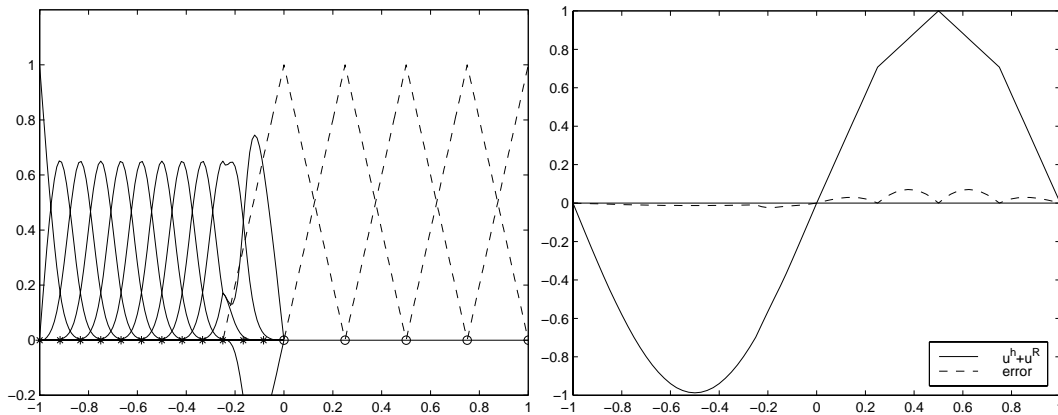


Figure 4.15: Approximation functions —12 particles and 5 nodes— (left) and interpolation result, $u^h + u^R$, with error distribution (right).

now the transition region includes 3 particles (one on its boundary and two in the interior of $\tilde{\Omega}$). The larger number of particles (with their associated smaller dilation parameter) induces a better approximation in $\Omega^p = [-1, 0]$.

4.5.2 Coupled and Enriched EFG-FEM

Coupling and enrichment can be employed together. In this case, particles are added and element removed without any particular restriction. Function $u(x) = \sin(2\pi x)$ in $\bar{\Omega} = [-1, 1]$ is interpolated. As shown in figure 4.16 four different regions are present: in $[-1, -0.5]$ only particles have an influence, in $[-0.5, 0]$ particles and a non complete basis of finite elements are present, in $[0, 0.5]$ both particles and complete finite elements are used, fi-

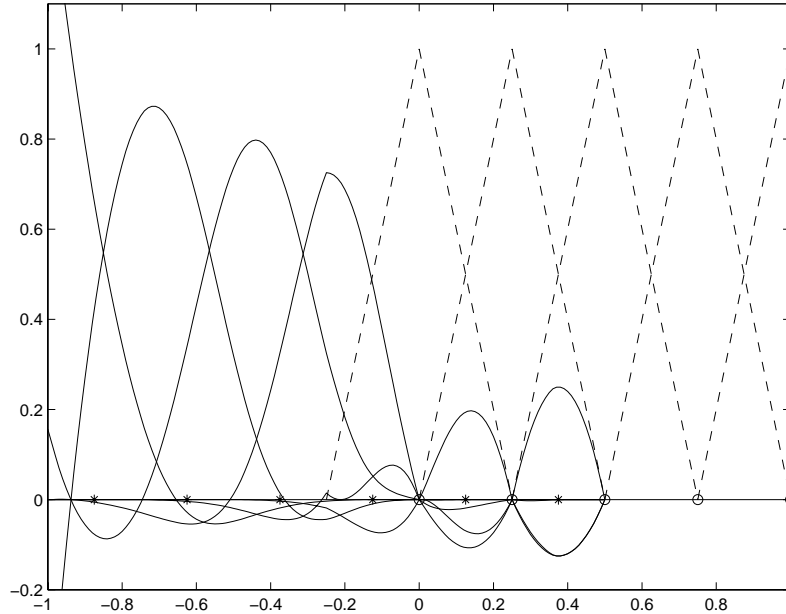


Figure 4.16: Approximation functions: 6 particles and 5 nodes

| | $[-1, -0.5]$ | $[-0.5, 0]$ | $[0, 0.5]$ | $[0.5, 1]$ |
|--------------------------|--------------|-------------|------------|------------|
| Error in L_2 norm | 0.059 | 0.098 | 0.073 | 0.107 |
| Error in L_∞ norm | 0.124 | 0.194 | 0.160 | 0.209 |
| DOF EFG+FEM | 2+0 | 2+1 | 2+3 | 0+3 |

Table 4.1: Measures of error for 6 particles and 5 nodes.

nally, in $[0.5, 1]$ only finite elements have an influence. Consistency is not uniform in this case, in $\overline{\Omega} \setminus \Omega^p = [0.5, 1]$ the finite element interpolation controls the order of consistency, $m = p = 1$. But in the mesh-free area of influence, i.e. $\overline{\Omega^p} = [-1, 0.5]$, the order of consistency required is $m = 2$.

Figure 4.17 shows the interpolation results obtained with the particle distribution of figure 4.16. Six particles and five nodes have been used, their associated shape functions are shown in figure 4.16. It is important to note that, as expected, the interpolation functions are hierarchical. The error in each region can be found in Table 4.1.

| | $[-1, -0.5]$ | $[-0.5, 0]$ | $[0, 0.5]$ | $[0.5, 1]$ |
|--------------------------|--------------|-------------|------------|------------|
| Error in L_2 norm | 0.015 | 0.027 | 0.036 | 0.107 |
| Error in L_∞ norm | 0.048 | 0.052 | 0.088 | 0.209 |
| DOF EFG+MEF | 4+0 | 3+1 | 3+3 | 0+3 |

Table 4.2: Measures of error for 11 particles and 5 nodes.

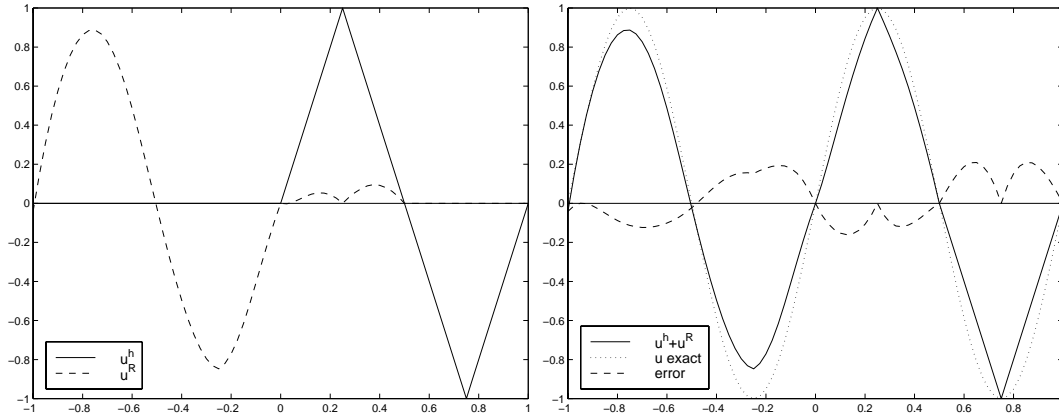


Figure 4.17: Mixed interpolation with 6 particles and 5 nodes

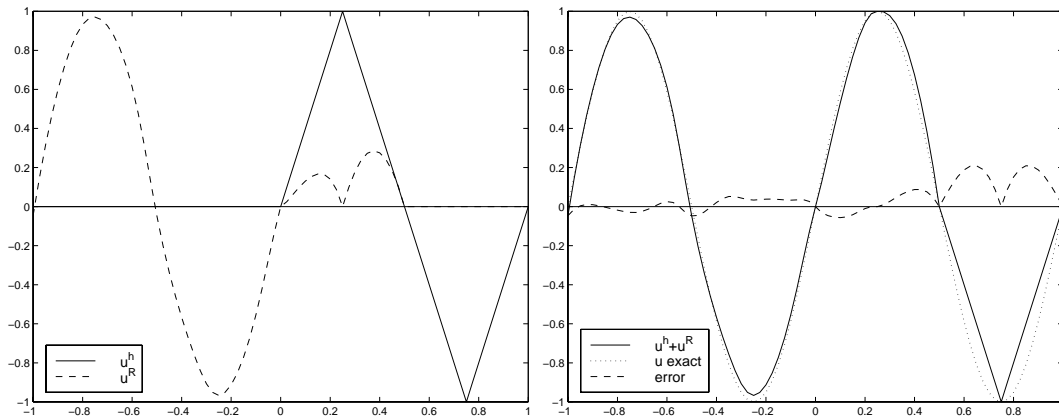


Figure 4.18: Mixed interpolation with 11 particles and 5 nodes

In $[0.5, 1]$ linear finite elements induce the larger error. In $[0, 0.5]$ the error is reduced with an “ h - p refinement”: particles are added and the order of consistency is increased. In both regions the finite element interpolation is complete. The price, in the number of degrees of freedom, is considerable. Similar results are obtained if the number of particles is increased. Figure 4.18 shows the results with the same finite element mesh, the same orders of consistency and 11 particles. The dilation parameter ρ is reduced by a half. The error measures can be found in Table 4.2.

This example also shows the influence of a coarse finite element mesh when the number of particles is increased. This point was already discussed in the error analysis. In $[-1, -0.5]$ and in $[0, 0.5]$ the distribution of particles is similar. In the former the precision is higher albeit that the number of degrees of freedom is lower than in the other region. In the latter the complete finite element interpolation introduces extra degrees of freedom but the error does not decrease. As previously noted, see section 4.4, if the finite element mesh is too coarse an increase in the number of particles does not reduce the error.

If the finite element mesh is enriched with mesh-free approximations, the coefficients associated to the finite element shape functions maintain their physical meaning. The mesh-free shape functions are hierarchical. However, convergence can only be achieved on a coarse mesh if the order of consistency is increased, i.e. adding more particles without any increase in m does not suffice.

4.5.3 Finite element enrichment with EFG in a 2D Poisson problem

The Poisson equation with Neumann and Dirichlet boundary conditions is solved next. The problem statement is

$$\left\{ \begin{array}{ll} \Delta u & = -f & \Omega = (0, 1) \times (0, 1) \\ \nabla u \cdot \mathbf{n} & = q_0 & \Gamma_n = \overline{\Omega} \cap \{y = 0\} \\ u & = u_0 & \Gamma_d = \partial\Omega \setminus \Gamma_n \end{array} \right.$$

where \mathbf{n} is the outward unit normal vector. The source term, f , and the boundary conditions, q_0 and u_0 , are chosen such that $u(x) = e^{-(6(x+y-1))^2}$ is the solution. Figure 4.19 depicts this solution (left) and a cross section on the plane $y = x$. Essential boundary conditions are imposed using Lagrange multipliers which are interpolated using the C^0 finite element interpolation functions along the boundary.

Figures 4.20 and 4.21 show the finite element mesh, the solution and the error distribution. An 8×8 quadrilateral mesh with bilinear finite elements (Q1) has been used. The

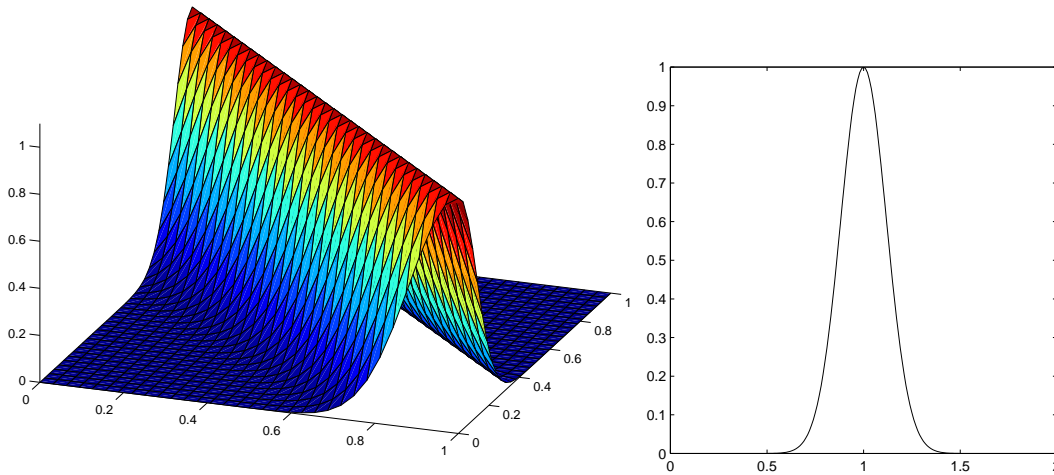


Figure 4.19: Analytical solution and section along $y = x$.

error is larger along the diagonal $x + y = 1$ and the error measure in the maximum norm (L_∞ norm) is 0.1707.

In order to improve the approximation, the finite element mesh is enriched adding particles and imposing an order of consistency $m = 2$. Figure 4.22 shows the finite element mesh and the distributions of particles. The error of the mixed approximation is also plotted in the same figure and with the same scale used in figure 4.20. In fact the measure in the maximum norm is now: 0.0204.

Finally, figure 4.23 presents the mixed approximation. The finite element approximation, u^h (top), is improved by a particle contribution, u^p (center), which induces the final mixed approximation, $u^h + u^p$ (bottom).

4.5.4 Finite element enrichment with EFG in nonlinear computational mechanics

This example reproduces the finite element enrichment with EFG in a nonlinear computational problem. A rectangular specimen with an imperfection is loaded, see (Díez, Arroyo and Huerta 2000, Huerta and Díez 2000). It has two axes of symmetry, a bilinear elastoplastic material is considered, and plane strain conditions are assumed. Figure 4.24 presents the problem statement with the material properties.

This problem has been solved with standard eight noded quadrilateral elements. Moreover, an adaptive error analysis (Huerta and Díez 2000, Huerta et al. 1999) has been conducted up to convergence. The final mesh and its equivalent inelastic strain distribution is

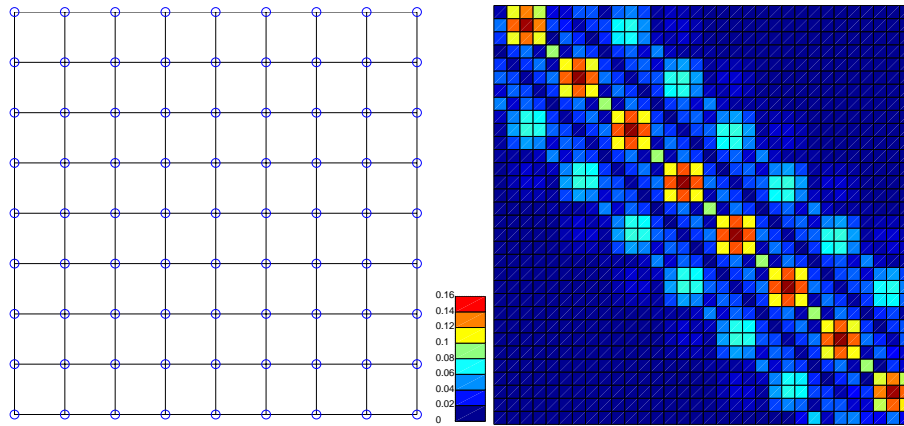


Figure 4.20: Finite element mesh and error distribution.

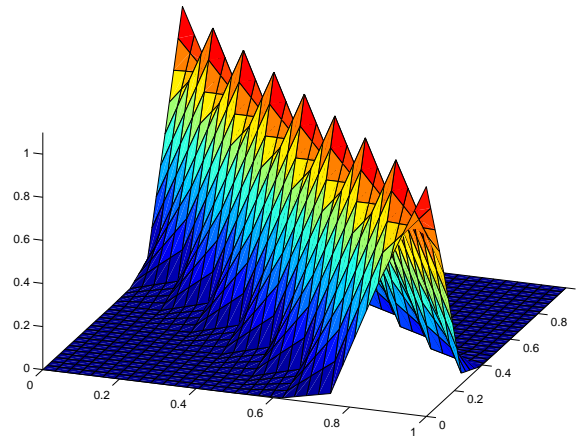
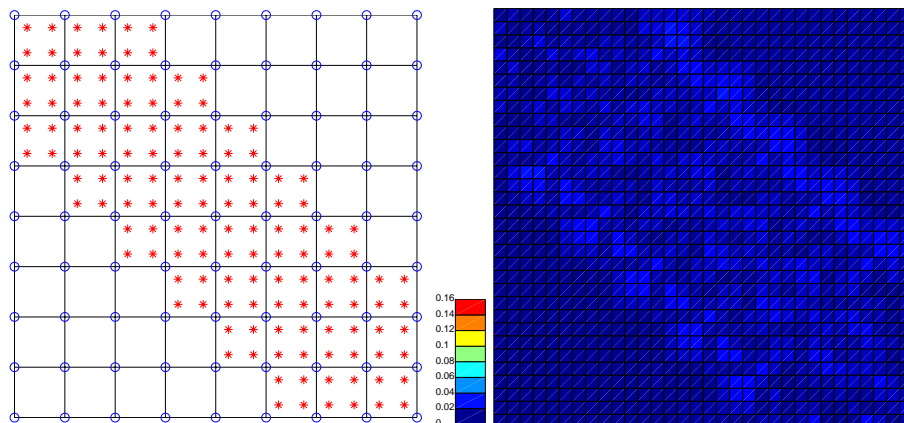
Figure 4.21: Approximation with 8×8 Q1 finite elements

Figure 4.22: Finite element mesh enriched with particles and error distribution of the mixed approximation.

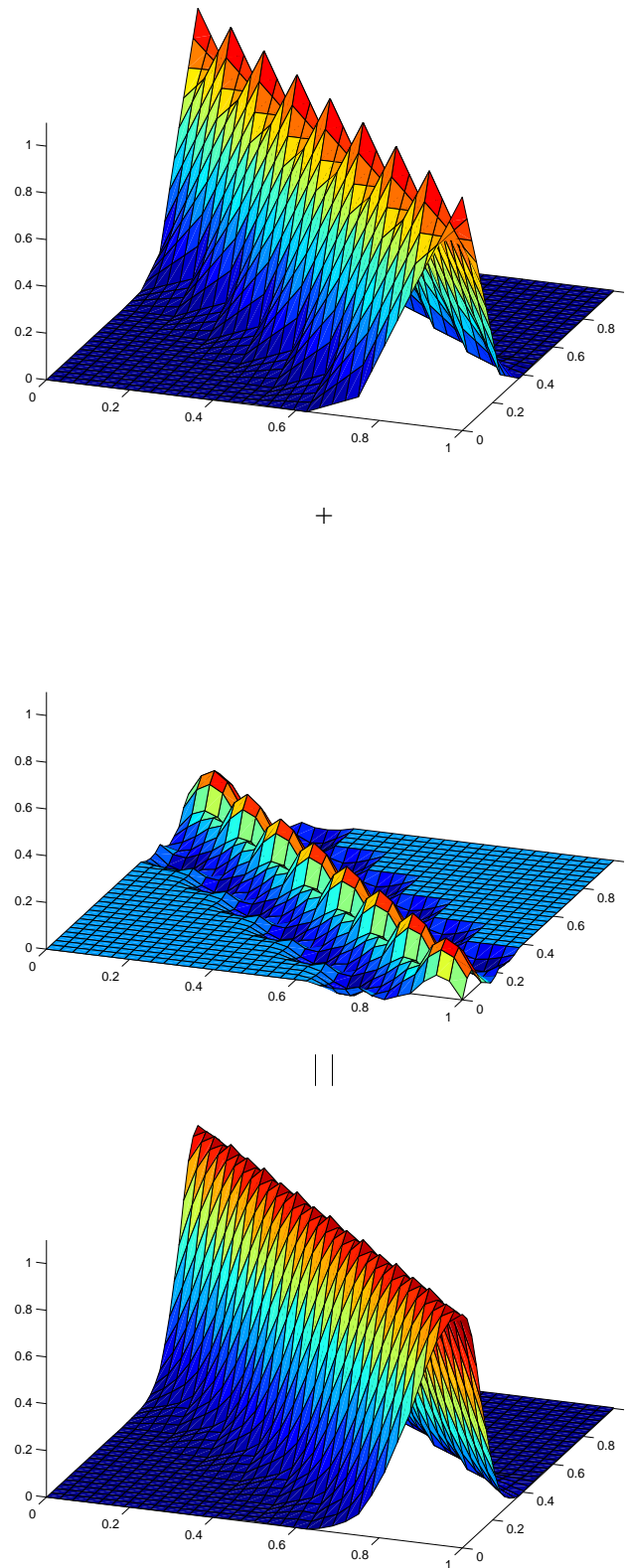


Figure 4.23: Finite element contribution w^h , enrichment with EFG u^ρ and mixed approximation $w^h + u^\rho$.

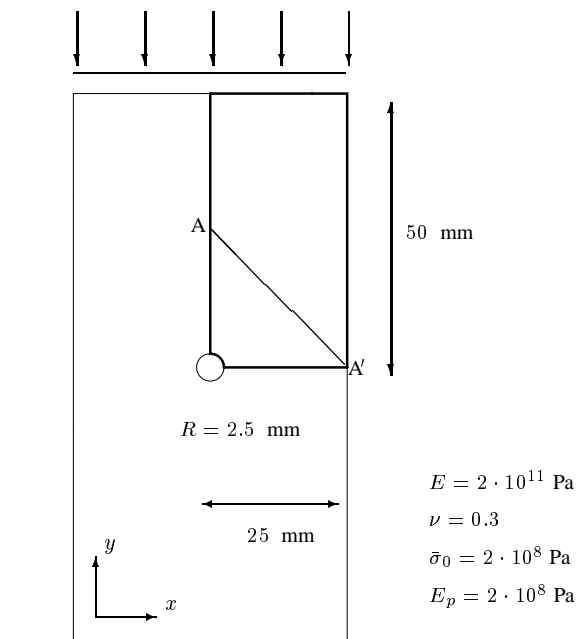


Figure 4.24: Problem statement: rectangular specimen with one centred imperfection.

shown in figure 4.25 (left). This mesh has 2022 dof and a relative error (measured in energy norm) of 0.18%.

The same example has also been solved with element free Galerkin. In order to obtain comparable results, the distribution of particles coincides with the distribution of nodes in the previous finite element mesh; and consistency of order two is required. Thus, the number of degrees of freedom (dof) is also 2022. Figure 4.25 (right) shows the distribution of particles and inelastic strains.

Results degrade drastically if a coarse mesh of quadrilateral bilinear finite elements (308 dof) is employed, see figure 4.26. However, when particles are added (308+906=1214 dof) and the order of consistency is increased ($m = 2$), the correct distribution of inelastic strains is recovered, see figure 4.26. Note that, the final finite element mesh in figure 4.25 (left) was obtained after an iterative process which needed for each iteration the generation of a new mesh. In this final example, figure 4.26, the original mesh is maintained and particles are added where they are needed.

Finally, figure 4.27 shows the evolution of the inelastic strains along the direction (A-A') for every configuration studied. Section (A-A') is plotted in figure 4.24.

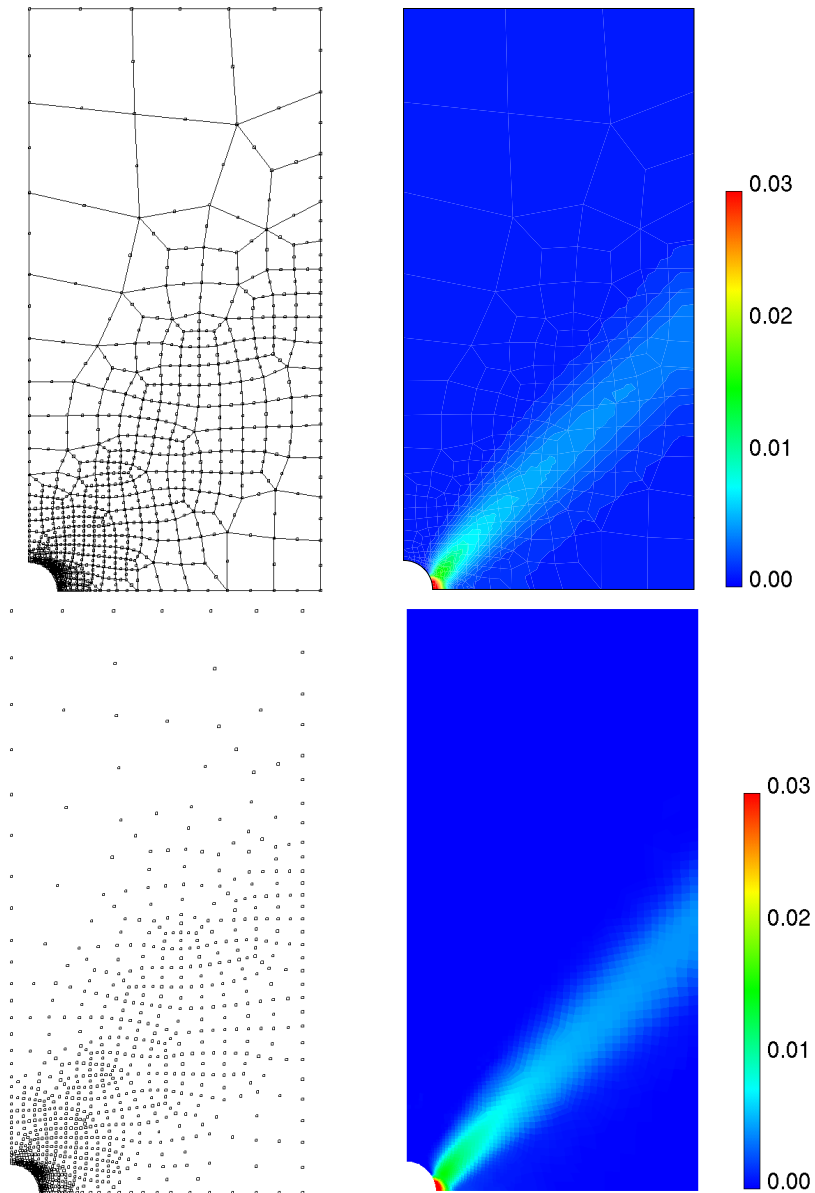


Figure 4.25: Final mesh with its corresponding equivalent inelastic strain for a standard finite element (8 noded elements) computation (top) and distribution of particles with its inelastic strain distribution for EFG (bottom).

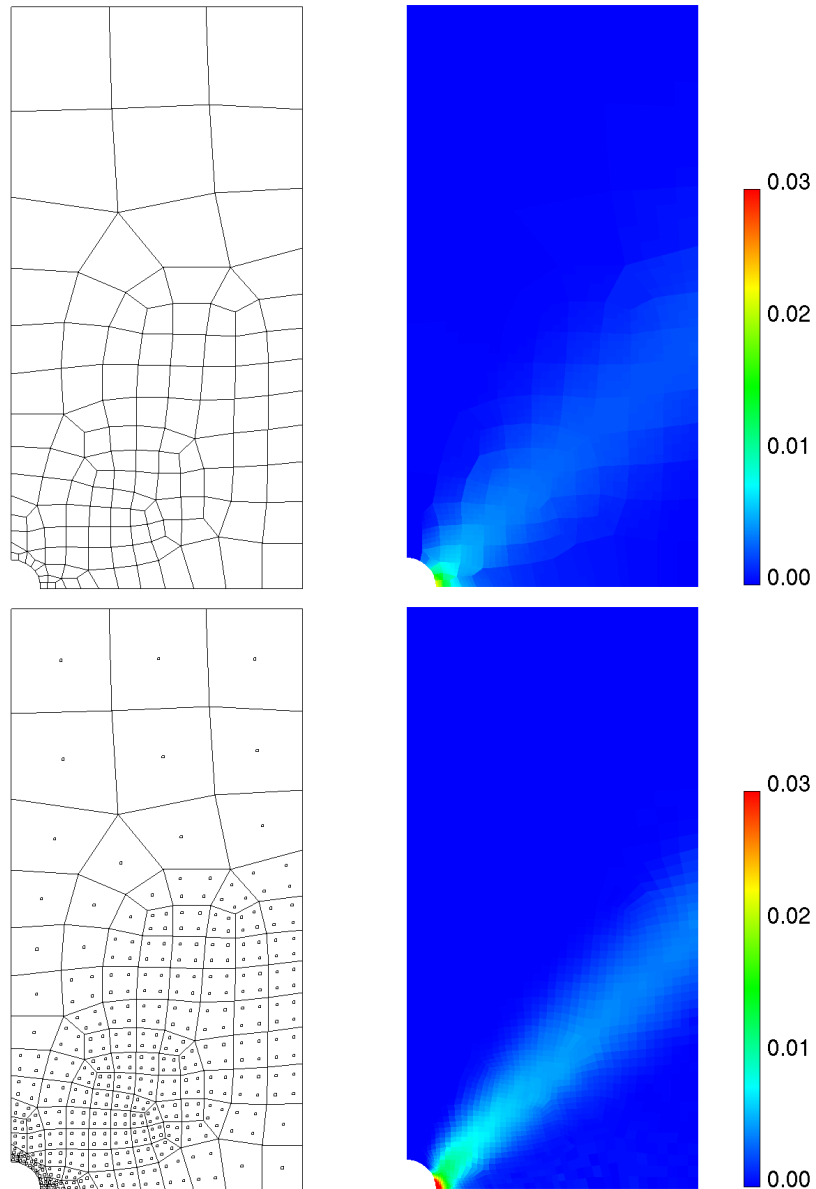


Figure 4.26: Coarse finite element mesh (Q1 elements) with its corresponding equivalent inelastic strain (top) and mixed interpolation with its equivalent inelastic strain distribution (bottom).

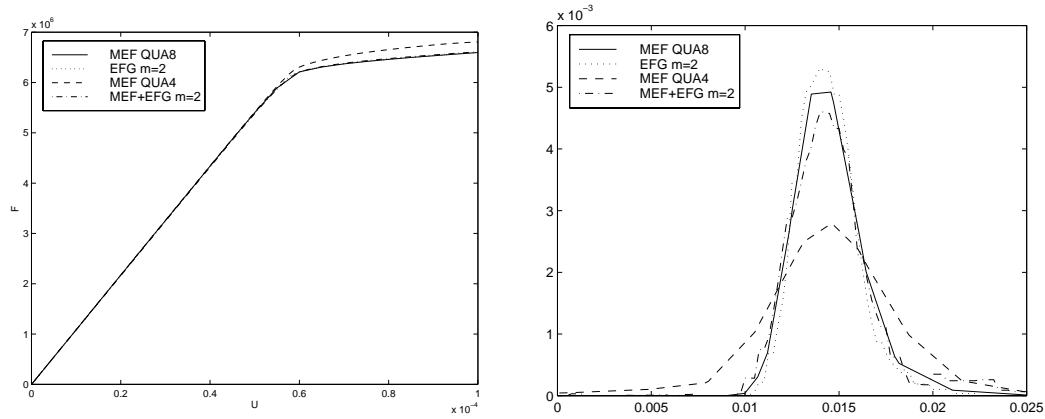


Figure 4.27: Force *versus* displacement (left) and evolution of the equivalent inelastic strain along (A-A') for each approximation (right).

4.5.5 Adaptivity in 2D convection-diffusion and diffusion-reaction problems coupling finite elements and particles

In this section a coupled FE-EFG formulation is used in order to take advantage of the comfort of EFG in refinement processes. Even if a good mesh generator is not available, the discretization can be easily refined suppressing some FE nodes and replacing them with a proper distribution of particles.

Diffusion-reaction problem

The diffusion-reaction problem is solved, namely

$$\begin{cases} -\nu\Delta u + \sigma u = 1 & \text{in } \Omega = (0, 1) \times (0, 1) \\ u = 0 & \text{on } \partial\Omega. \end{cases}$$

This problem has double symmetry with respect to $x = 0.5$ and $y = 0.5$. Therefore, it is solved in $[0.5, 1] \times [0.5, 1]$ with homogeneous Neumann conditions on the new boundaries (symmetry boundary conditions). For presentation purposes, in the following pictures the solution is depicted over the whole domain, although only a quarter of the domain is discretized.

The Galerkin FE solution obtained with 10×10 bilinear elements is shown in figure 4.28. The solution presents high gradients that cannot be properly interpolated with the coarse regular FE mesh. The interpolation needs to be enriched near the boundary.

The discretization can be easily enriched using particles. Thus some nodes are removed near the boundary, particles are added (red \times) and a mixed interpolation is considered. Fig-

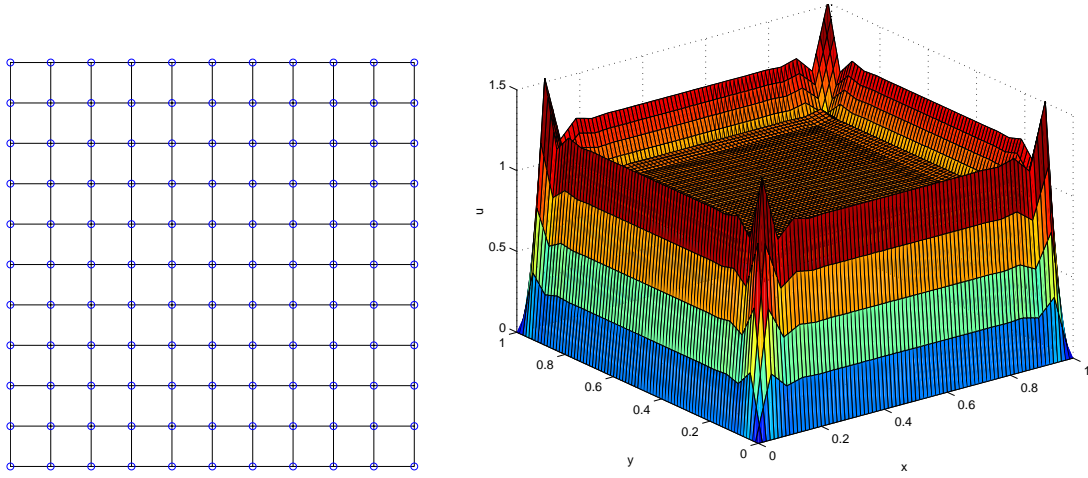


Figure 4.28: FE mesh (11x11=121 nodes) and Galerkin solution with $\nu = 10^{-5}$, $\sigma = 1$.

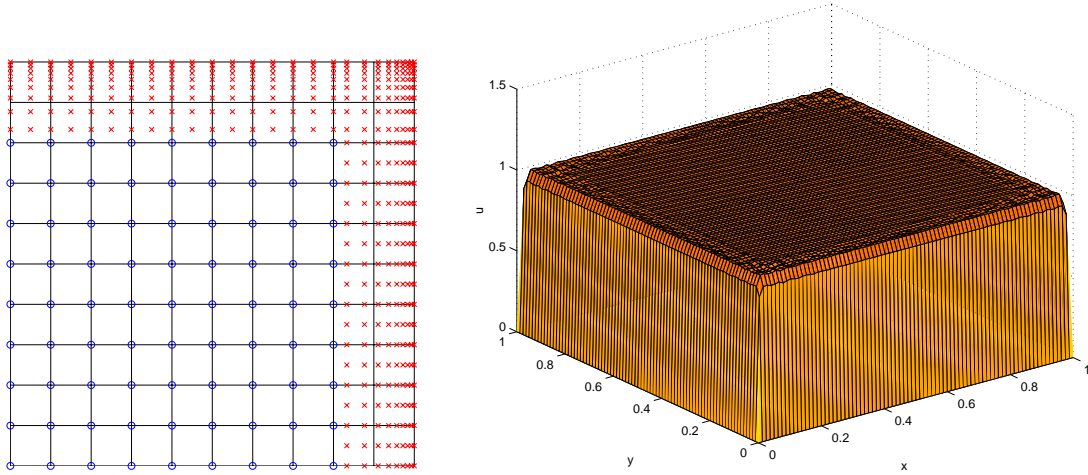


Figure 4.29: Mixed distribution with 81 nodes (o) and 387 particles (x), and Galerkin solution with $\nu = 10^{-5}$, $\sigma = 1$.

Figure 4.29 shows a refined distribution with 81 nodes and 387 new particles and the obtained solution. In each edge of the boundary there is a row of elements where the influence of all nodes is totally eliminated: only an EFG interpolation is considered, $u = u^p$. In the second row only some nodes are removed and a mixed interpolation is used: $u = u^h + u^p$ in the transition region. Particles do not need connectivities and the refinement can be easily performed. Rectangular supported weight functions, $\phi_p(x, y) = \phi_{1D}(\frac{x}{\rho_1})\phi_{1D}(\frac{y}{\rho_2})$, have been used in order to avoid singular matrices \mathbf{M} in the definition of the shape functions. Finally, there is no need to enrich the solution in the interior of the domain and the FE interpolation (with lower computational cost) can be preserved. The solution is obviously

improved after refinement.

Stationary convection-diffusion problems

Two layers example:

The convection-diffusion problem described in figure 4.30 is solved. Figure 4.31 shows the Galerkin solution for $|\mathbf{a}| = 1$ and $\nu = 0.0025$ solved with a regular mesh of 20×20 quadrilateral bilinear finite elements. The Peclet number is $Pe = \frac{|\mathbf{a}|h}{2\nu} = 10 > 1$ and therefore the Galerkin numerical solution suffers of important oscillations.

$$\begin{cases} -\nu \Delta u + \mathbf{a} \cdot \nabla u = 1 & \text{in } \Omega = (0, 1) \times (0, 1) \\ u = 0 & \text{on } \partial\Omega \end{cases}$$

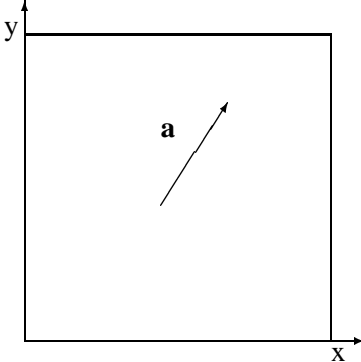
$$\mathbf{a} = |\mathbf{a}| (\cos(\pi/3), \sin(\pi/3))$$


Figure 4.30: Convection-diffusion problem statement.

First, the solution is improved with pure FE h-refinement. Figure 4.32 shows the Galerkin solution obtained with a FE mesh of 80×80 elements. Note that most of the oscillations have been eliminated but some of them persist. However, the refinement can be done in a more efficient manner. Now the proposed mixed approximation (coupling FE and particles) is used instead of the standard FE mesh refinement technique, see figure 4.33. Some nodes are removed and replaced by particles. It is worth mentioning that, there is no restriction on the particles position because connectivities are not needed.

In figures 4.34 and 4.35 a problem with a large Péclet number is presented: $\mathbf{a} = 1$, $\nu = 10^{-4}$. An SUPG stabilization technique (Brooks and Hugues 1982) is employed in order to avoid instabilities, with two different values of the intrinsic time parameter τ . The 20×20 FE solution is depicted in figure 4.34 with $\tau = 0.025$ and $\tau = 0.005$. A constant parameter τ is used all over Ω . The first value for the parameter, $\tau = 0.025$, has been computed with the standard 1D SUPG formula (Brooks and Hugues 1982) for the 20×20 mesh ($h = 0.05$). Thus, if τ is reduced to $\tau = 0.005$ there is not enough artificial diffusion and oscillations reappear. Oscillations are alleviated only if the artificial diffusion is large enough. Figure 4.35 shows the mixed interpolation results. If the intrinsic time is kept

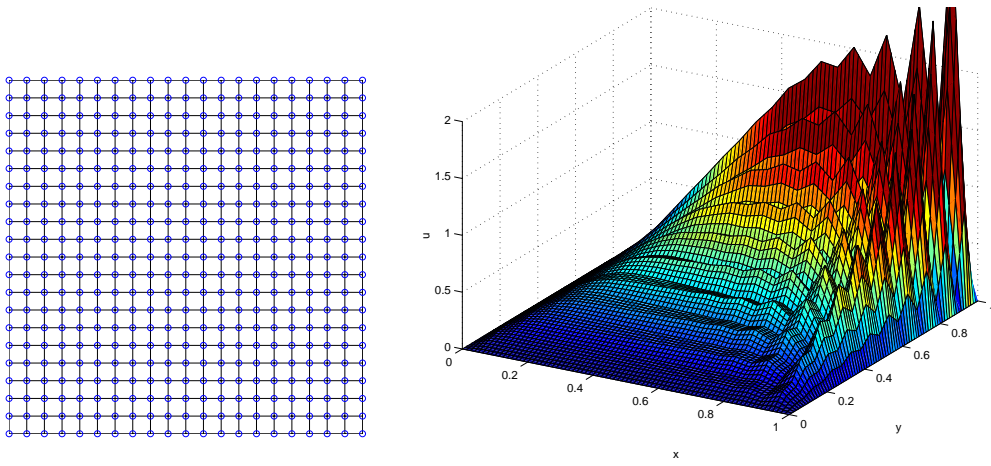


Figure 4.31: FE mesh ($21 \times 21 = 441$ nodes) and Galerkin solution for $|a| = 1, \nu = 0.0025$

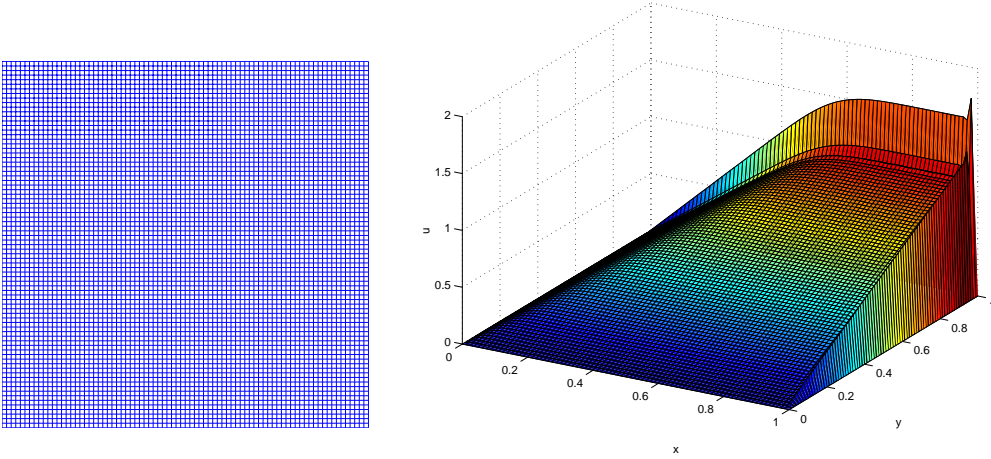


Figure 4.32: FE mesh ($81 \times 81 = 6561$ nodes) and Galerkin solution for $|a| = 1, \nu = 0.0025$

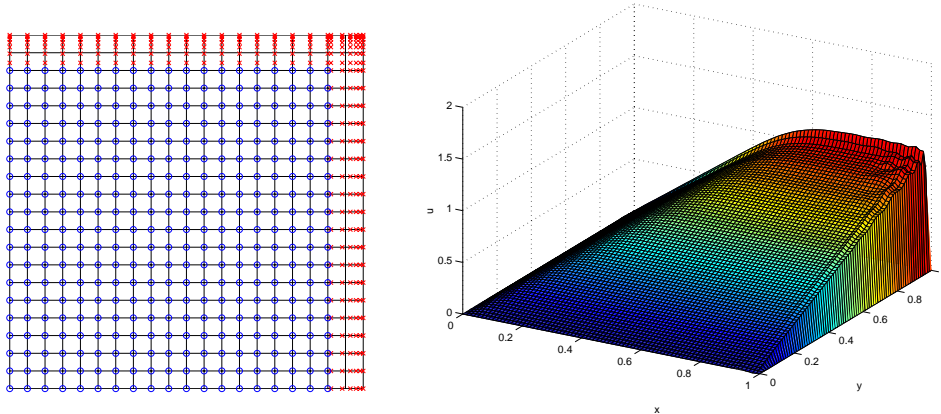


Figure 4.33: Discretization with 361 nodes and 289 particles and Galerkin solution for $|a| = 1, \nu = 0.0025$

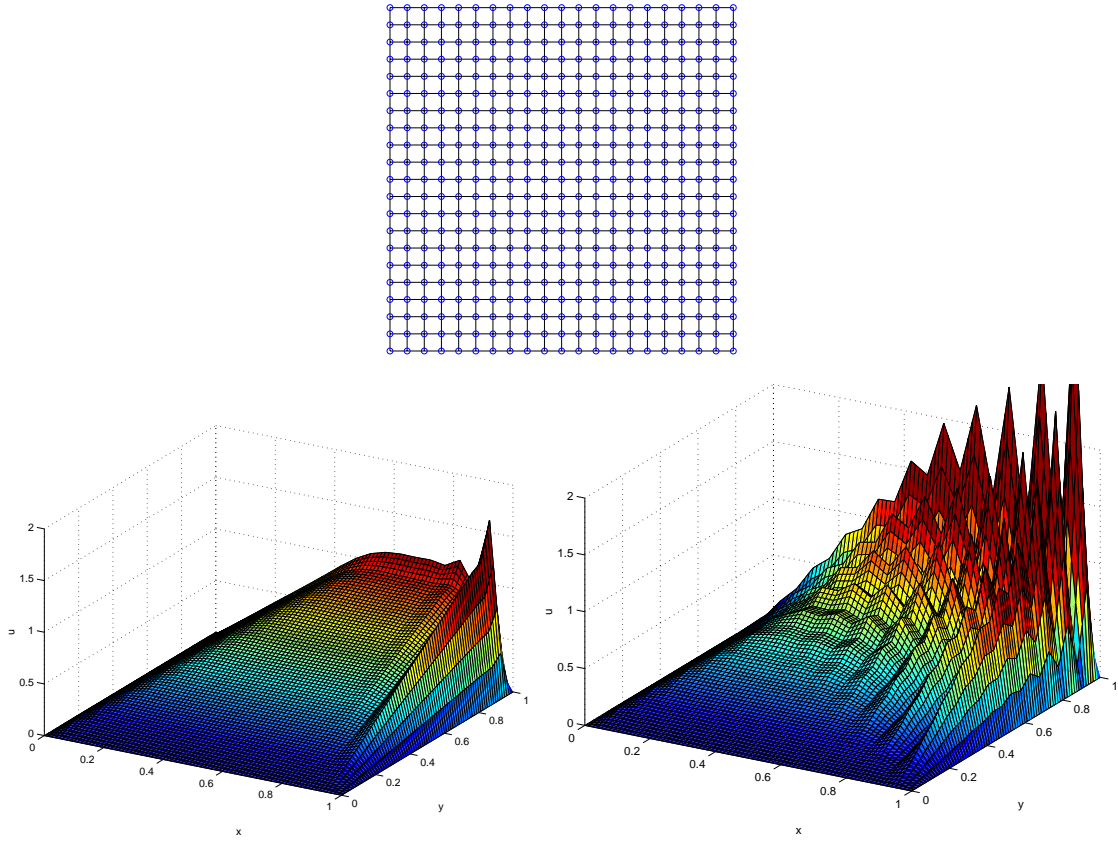


Figure 4.34: FE mesh ($21 \times 21 = 441$ nodes) and SUPG solution with $\tau = 0.025$ and $\tau = 0.005$, for $|a| = 1$, $\nu = 10^{-4}$

constant $\tau = 0.025$, as for the coarse FE mesh, the solution does not oscillate, but obviously it is over-diffusive. However, the refinement induced by the added particles allows using a lower added diffusion ($\tau = 0.005$) and thus, a more realistic solution is obtained.

Remark 4.5.1. The consistent SUPG weak form for this problem can be written as: find u such that

$$\begin{aligned} \int_{\Omega} \nabla v \nu \nabla u \, d\Omega + \int_{\Omega} v(\mathbf{a} \cdot \nabla u) \, d\Omega &+ \sum_e \int_{\Omega_e} \tau(\mathbf{a} \cdot \nabla v) [-\nu \Delta u + \mathbf{a} \cdot \nabla u] \, d\Omega = \\ \int_{\Omega} v \, d\Omega &+ \sum_e \int_{\Omega_e} \tau(\mathbf{a} \cdot \nabla v) \, d\Omega, \end{aligned} \quad (4.5.1)$$

for all v , where it is assumed that $v = 0$ on $\partial\Omega$ in order to clarify the notation. In (4.5.1) one can observe the usual Galerkin terms, in black, and the extra SUPG stabilization terms, in blue, integrated over the elements or integration cells, Ω_e . Note that there is one extra

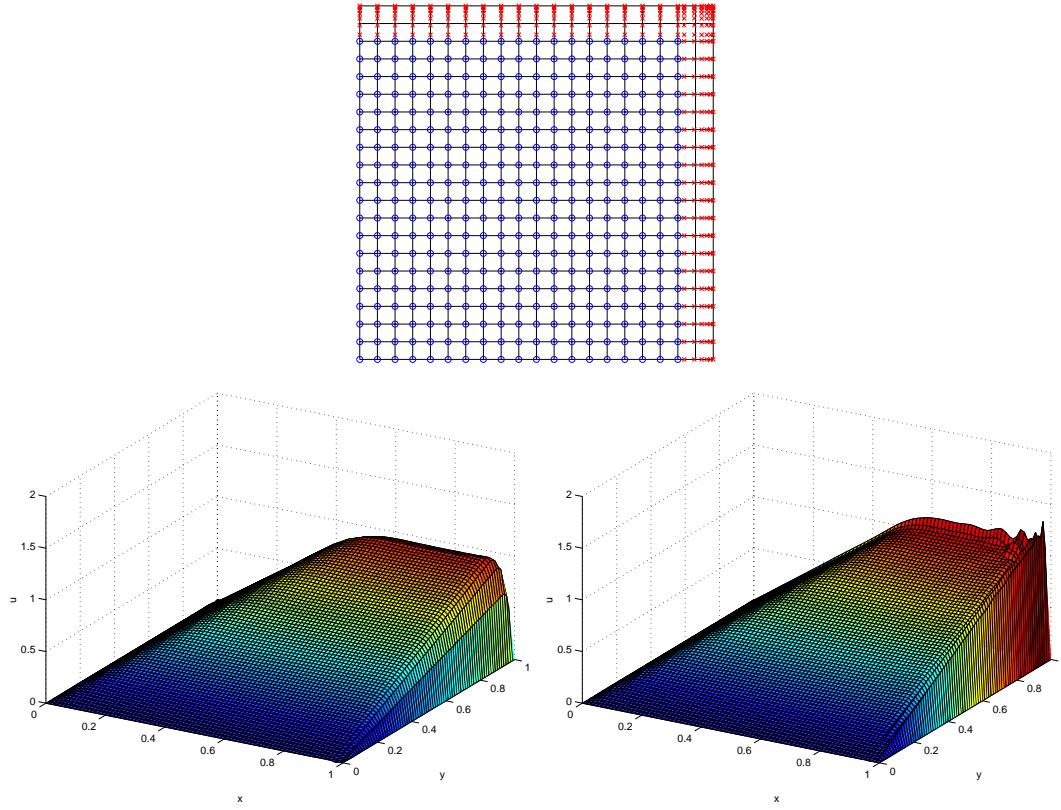


Figure 4.35: Discretization with 361 nodes (o) and 289 particles (x), and SUPG solution with $\tau = 0.025$ and $\tau = 0.005$, for $|a| = 1$, $\nu = 10^{-4}$.

term which includes second derivatives of the approximation, $\sum_e \int_{\Omega_e} \tau(\mathbf{a} \cdot \nabla v) \nu \Delta u \, d\Omega$, which can not be eliminated with integration by parts. As will be commented in chapter 5, when the EFG interpolation is used, second derivatives of the approximation are well defined in the whole domain and thus, the consistent weak form (4.5.1) can be considered. However, when linear finite elements are used, this term with second derivatives is usually neglected or under-represented and this non-consistent weak form is actually used

$$\int_{\Omega} \nabla v \nu \nabla u \, d\Omega + \int_{\Omega} v(\mathbf{a} \cdot \nabla u) \, d\Omega + \sum_e \int_{\Omega_e} \tau(\mathbf{a} \cdot \nabla v)(\mathbf{a} \cdot \nabla u) \, d\Omega = \int_{\Omega} v \, d\Omega + \sum_e \int_{\Omega_e} \tau(\mathbf{a} \cdot \nabla v) \, d\Omega, \quad (4.5.2)$$

$\forall v$. The lack of consistency due to this neglected term leads to errors in the numerical scheme, see (Jansen, Collins, Whiting and Shakib 1999) for details. However, these errors are almost negligible for the stationary case: there are not substantial differences between the solution obtained with the mixed interpolation with the non-consistent weak form (4.5.2)

and the solution obtained with the mixed interpolation with (4.5.2) in the FE region and (4.5.1) in the EFG region. This is not the case in transient problems, where the errors due to the lack of consistency can drastically degrade the accuracy and convergence in time, see chapter 5.

Three layers example:

The convection diffusion problem described in figure 4.36 is considered. The boundary conditions are chosen such that an internal layer is present in the solution.

$$\begin{cases} -\nu\Delta u + \mathbf{a} \cdot \nabla u = 0 & \text{in } \Omega = [0, 1] \times [0, 1] \\ u = 1 & \text{in } \Gamma_1 \\ u = 0 & \text{in } \partial\Omega \setminus \Gamma_1 \end{cases}$$

$$\mathbf{a} = |\mathbf{a}| (\cos(\pi/6), \sin(\pi/6))$$

$$|\mathbf{a}| = 1, \nu = 10^{-4}$$

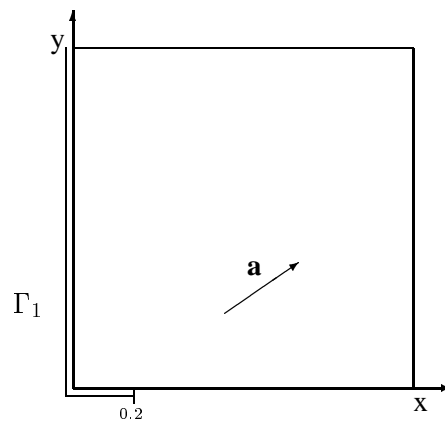


Figure 4.36: Convection-diffusion problem statement.

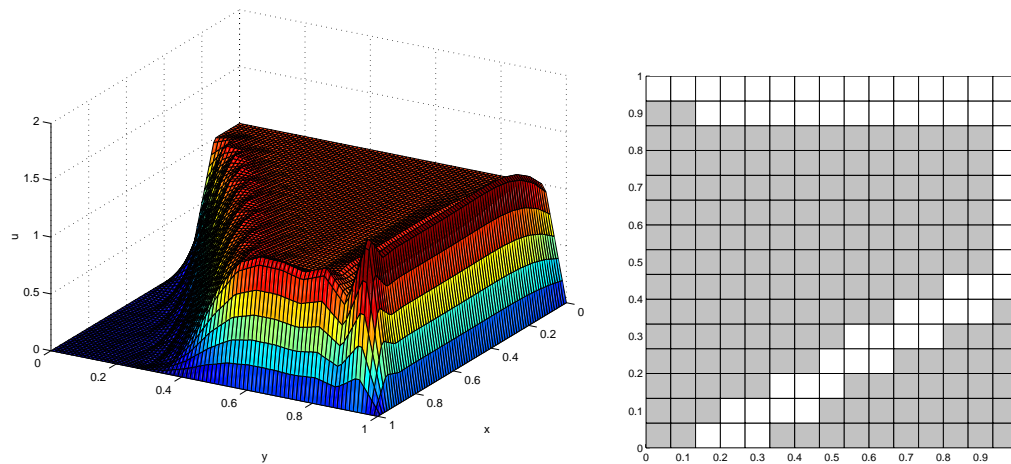


Figure 4.37: SUPG solution with 15×15 linear finite elements and $\tau = 0.0333$, and detection of elements with $\|\nabla u\| > \frac{1}{3h}$ (in white)

Figure 4.37 shows the SUPG numerical solution with 15×15 linear finite elements and $\tau = 0.0333$. The stabilization parameter has been computed with the standard 1D SUPG

formula. There still remain some oscillation in the solution. A mixed interpolation combining finite elements and particles is considered in order to improve the results: nodes are removed and replaced by a denser distribution of particles in all the elements with high gradients in the solution (see figure 4.37). There is no restriction on the particles position since particles do not need connectivities. Figure 4.38 shows the mixed distribution of nodes and particles and its corresponding SUPG solution with $\tau = 0.0333$ and $\tau = 0.015$. The refined mixed interpolation allows reducing the added diffusion ($\tau = 0.015$) and thus, a more realistic solution is obtained. Figure 4.39 shows a section along $x = 0.75$ for the finite element solution with $\tau = 0.0333$, and for the mixed interpolation solution with $\tau = 0.0333$ and $\tau = 0.015$. After refinement the solution is clearly improved in both the boundary layer and the internal layer. Similar results could be obtained with EFG in the whole domain or FE and a good mesh generator.

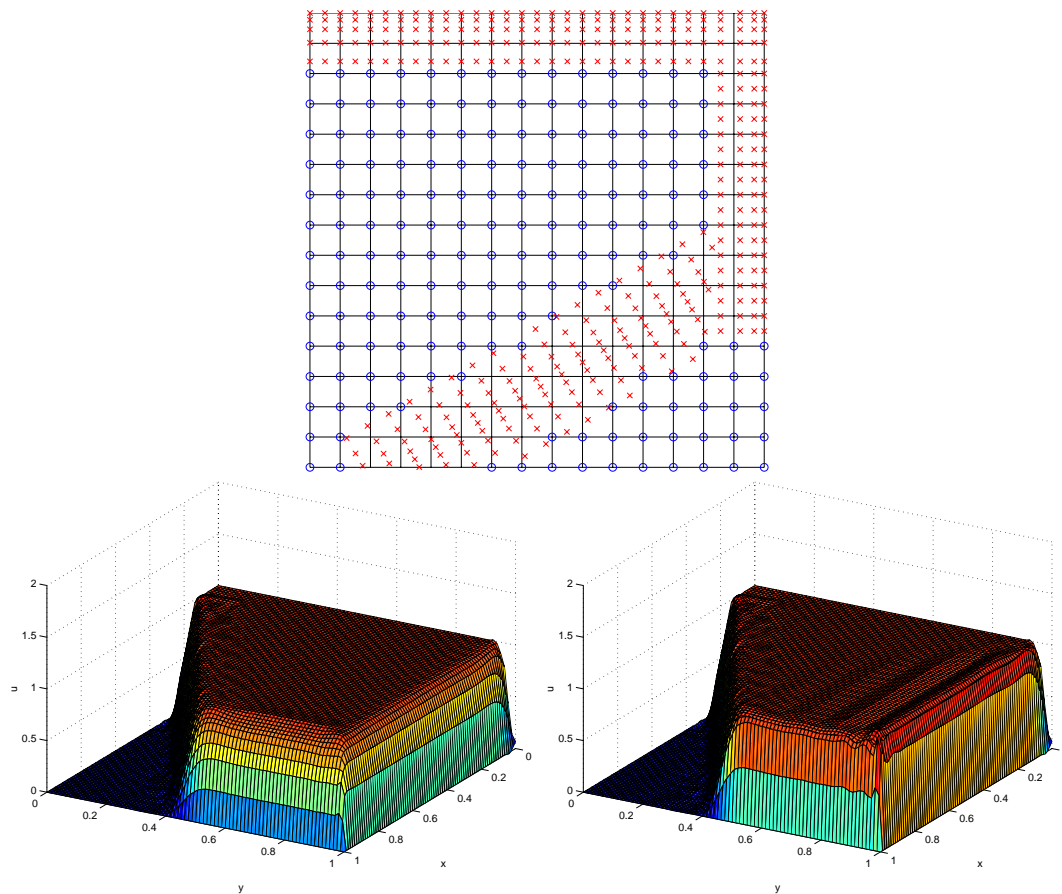


Figure 4.38: Mixed distribution with 210 nodes (o) and 211 particles (x), and corresponding SUPG solution with $\tau = 0.0333$ (left) and $\tau = 0.015$ (right)

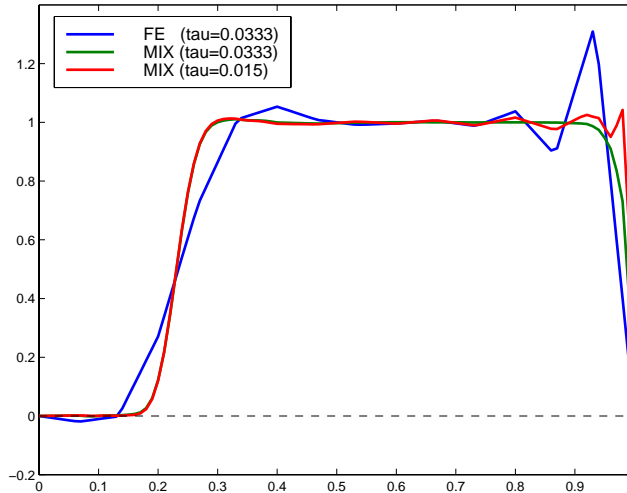


Figure 4.39: Section along $x = 0.75$ for the finite element interpolation with $\tau = 0.0333$ and the mixed interpolation with $\tau = 0.0333$ and $\tau = 0.015$

4.6 Conclusions

This chapter develops a mixed interpolation, it is based on finite element and mesh-free methods. In fact it is an extension of previous published papers by Liu, Belytschko and coworkers (Liu et al. 97, Liu et al. 1997, Belytschko et al. 1995) with a unified formulation generalizable to any spatial order (p or m) and with its corresponding convergence analysis. Two different cases have been studied: coupled finite elements with EFG, $p = m$, or enrichment of finite elements with EFG, $m > p$. For the sake of clarity, EFG has been used as the mesh-free method. However, generalization to other methods based on a Moving Least Squares development is straight forward.

The first case allows to implement Dirichlet boundary conditions in a standard finite element context. In fact, this was proposed by Belytschko et al. (1995) and here a simple generalization avoids the use of any ramp function and the need of substituting nodes per particles. That is, particles can be added arbitrarily in the region of the computational domain where the finite element interpolation is not complete. This ensures continuity of the solution (no coupling via Lagrange multipliers is imposed) and also enforces a uniform order of consistency (and thus of convergence) everywhere in the computational domain.

The coupled FE-EFG formulation can also be employed in order to take advantage of the comfort of EFG in refinement processes. In absence of a good mesh generator, the discretization can be easily refined just taking off some nodes and replacing them with a suitable distribution of particles. The convergence properties of the mixed approximation

are similar to those of the finite element method or element-free Galerkin.

The second case, enrichment of finite elements with EFG, also allows to improve the accuracy of finite elements where needed in an adaptive process without any remeshing. The *a priori* error bounds of this formulation are illustrated with numerical examples and stated in a formal setting. They indicate that both the element size, h , and the dilation parameter, ρ , influence the convergence, as well as the order of the finite element interpolation, p , and the increase of order of consistency, q , due to the added particles. Moreover, the *a priori* bound shows that h , h - p or ρ - q refinements will induce convergence but ρ refinement on its own will fail to decrease arbitrarily the error of the approximation. That is, convergence can not be attained by simply adding particles and thus reducing the dilation parameter, an increase in the order of consistency is needed.

Both cases are illustrated with several examples. They show the applicability of the proposed formulation in standard linear and nonlinear boundary value problems.

Chapter 5

Time accurate consistently stabilized mesh-free methods for convection dominated problems

5.1 Introduction

A great deal of effort has been devoted in the recent years to the development of finite element methods for the numerical approximation of transient convection-diffusion problems. It is well known that the standard Galerkin is not ideally suited to deal with the spatial discretization of convection dominated problems. Thus, other spatial discretization techniques are necessary to introduce the suitable amount of numerical dissipation in the presence of internal and boundary layers. In truly transient problems, another equally important aspect is to ensure an adequate coupling between the spatial approximation and the time integration scheme. Now, it is also well known that the combination of a standard Galerkin spatial discretization with classical second order accurate time stepping schemes, such as Lax-Wendroff and Crank-Nicolson methods, fails to produce satisfactory numerical results when convection dominates the transport process (no internal or boundary layers being present), see (Donéa, Quartapelle and Selmin 1987) or (Morton 1996). In conclusion, transient convection-diffusion problems need stabilization because of the internal and boundary layers, and high-order time stepping schemes for accuracy in convection dominated problems. Note that in real engineering problems the relative weight of the convective and diffusive term may vary in space and time, see for instance appendix B. This effect is usually accentuated by a non uniform mesh due to geometrical considerations. In order to overcome some of these difficulties, in (Donéa, Roig and Huerta 2000) a unified approach for high-order implicit time stepping is presented. Then, in (Huerta and Donéa 2001) and

(Huerta, Roig and Donéa 2001) these methods are combined with classical stabilization techniques in the framework of the finite element method.

However, finite element methods are usually non consistently stabilized. The second derivatives needed in the stabilization term are usually neglected. This implies a loss of convergence, which is more dramatic in high-order time accurate methods as it will be shown here. Several solutions are apparent and some of them have been explored. For instance, the stabilization parameter (*i.e.* the intrinsic time τ) could be modified for each integration scheme in order to ensure high-order time convergence rates, even if second derivatives are still not computed. Another alternative in order to preclude the computation of second derivatives is to take into account flux jumps across element boundaries (Tezduyar and Osawa 2000). Finally, second derivatives can be approximated (Jansen et al. 1999). This implies a global reconstruction for linear elements (a global least-squares problem). For high order elements, a local (element by element) reconstruction or the usual computation of the second derivatives can be envisioned. As claimed in (Jansen et al. 1999) both alternatives have similar computational cost and ensure the theoretical convergence rates.

In mesh-free methods, see section 2.2.4 or reference (Belytschko, Krongauz, Fleming, Organ, and Liu 1996), second derivatives are computed at a reduced extra cost, that is an extra cost considerably lower than in finite elements. Moreover the mesh-free interpolation space is a subset of $\mathcal{H}^2(\Omega)$ and thus, the standard stabilization techniques can be formulated naturally in $\mathcal{H}^2(\Omega)$. Second order space derivatives of the interpolation are well defined in the whole domain even with linear consistency. There are not neglected terms in the weak form and the convergence rates of the high-order time integration schemes are preserved. Moreover, the moving least-squares (MLS) interpolation allows increasing the order of the spatial discretization in a simple manner. With a mesh-free interpolation, space and time high-order consistent stabilized formulations are easily defined and implemented.

This chapter extends the time accurate schemes with classical stabilization techniques presented in (Huerta and Donéa 2001) to mesh-free methods, and compares the performance of such consistently stabilized methods with finite element results. It is organized as follows. In section 5.2 the Galerkin formulation, the stabilized least-squares (Donéa, Roig and Huerta n.d.) formulation and the Streamline-Upwind Petrov-Galerkin (Shakib and Hughes 1991, Tezduyar and Osawa 2000) formulation are considered in combination with two different time stepping multi-stage implicit methods, with second and fourth order respectively. In fact, all formulations are first recalled in the framework of finite elements in section 5.2.2. Then, section 5.2.3 is devoted to the particularization of these formulations

for the mesh-free interpolation. In section 4.4, a 1D numerical example allows analyzing the converge in time for the recalled formulations. The numerical experiments agree with the conclusions derived in the previous sections. Finally, numerical examples with mesh-free interpolation are shown in section 5.4 in order to illustrate the importance of time accurate computations and the need of stabilized formulations in the resolution of transient convection-diffusion problems.

5.2 Time and space discretization for the transient convection-diffusion equation

We are concerned with an accurate solution of the following transient convection-diffusion boundary value problem with constant coefficients: “Given the velocity field $\mathbf{a}(\mathbf{x})$, the constant diffusion coefficient ν and the source term $s(\mathbf{x}, t)$, find $u(\mathbf{x}, t)$ such that verifies

$$u_t + \mathbf{a} \cdot \nabla u - \nu \nabla^2 u = s \quad \text{in } \Omega \times (0, T), \quad (5.2.1)$$

the initial conditions,

$$u(x, 0) = u_0(x) \quad \text{in } \Omega,$$

and the boundary conditions,

$$\begin{aligned} u &= u_D && \text{in } \Gamma, \\ \nabla u \cdot \mathbf{n} &= f && \text{in } \partial\Omega \setminus \Gamma, \end{aligned}$$

where \mathbf{n} is the unitary outward normal vector”. Symbolically the partial differential equation (5.2.1) may be rewritten as

$$u_t + \mathcal{L}(u) = s, \quad (5.2.2)$$

where the spatial differential operator is defined as

$$\mathcal{L} := \mathbf{a} \cdot \nabla - \nu \nabla^2. \quad (5.2.3)$$

The numerical solution of such a problem clearly involves a double discretization process, that is, time discretization and space discretization. In this paper, the methodology proposed in (Huerta and Donéa 2001) is considered: (1) multi-stage time stepping schemes of high accuracy are used and (2) standard stabilization techniques are implemented. The objective is to adapt the standard stabilization techniques, well known in stationary problems, to transient problems in combination with multi-stage time stepping schemes. Consequently, in the following, time discretization precedes spatial discretization.

5.2.1 Time discretization

For illustration purposes, only two implicit multi-stage methods are presented. A more complete presentation can be found in (Donéa et al. 2000). These schemes can be written in incremental form as

$$\frac{\Delta \mathbf{u}}{\Delta t} - \mathbf{W} \Delta \mathbf{u}_t = \mathbf{w} u_t^n, \quad (5.2.4)$$

where the unknown $\Delta \mathbf{u} \in \mathbb{R}^{n_{\text{stg}}}$ is a vector whose dimension is the number of stages, n_{stg} . The vector $\Delta \mathbf{u}_t$ is the partial derivative of $\Delta \mathbf{u}$ with respect to time. The time derivatives in (5.2.4) are replaced by spatial derivatives using the original differential equation (5.2.2):

$$\frac{\Delta \mathbf{u}}{\Delta t} + \mathbf{W} \mathcal{L}(\Delta \mathbf{u}) = \mathbf{w} [s^n - \mathcal{L}(u^n)] + \mathbf{W} \Delta \mathbf{s} \quad (5.2.5)$$

The precise definition of $\Delta \mathbf{u}$, $\Delta \mathbf{s}$, \mathbf{w} and \mathbf{W} depends on each particular method:

Second order Padé approximation: R_{11} (Crank-Nicolson)

$$\boxed{\begin{array}{ll} \Delta \mathbf{u} = u^{n+1} - u^n, & \Delta \mathbf{s} = s^{n+1} - s^n, \\ \mathbf{W} = \frac{1}{2} & \mathbf{w} = 1. \end{array}} \quad (5.2.6)$$

Note that in this case $n_{\text{stg}} = 1$ and the vectors and matrix in (5.2.4) become scalars. In fact, this scheme corresponds to the well known Crank-Nicolson method.

Fourth order Padé approximation: R_{22}

$$\boxed{\begin{array}{ll} \Delta \mathbf{u} = \begin{Bmatrix} u^{n+\frac{1}{2}} - u^n \\ u^{n+1} - u^{n+\frac{1}{2}} \end{Bmatrix}, & \Delta \mathbf{s} = \begin{Bmatrix} s^{n+\frac{1}{2}} - s^n \\ s^{n+1} - s^{n+\frac{1}{2}} \end{Bmatrix}, \\ \mathbf{W} = \frac{1}{24} \begin{bmatrix} 7 & -1 \\ 13 & 5 \end{bmatrix}, & \mathbf{w} = \frac{1}{2} \begin{Bmatrix} 1 \\ 1 \end{Bmatrix}. \end{array}} \quad (5.2.7)$$

The R_{11} and R_{22} schemes are in fact implicit Runge-Kutta methods based on the Lobatto IIIA quadrature. For these methods the truncation error induced by (5.2.4) is precisely $\mathcal{O}(\Delta t^{2n_{\text{stg}}})$. However, it is important to note that the methodology proposed here is independent of these two particular schemes and can be implemented with any multi-stage algorithm.

Note that equations (5.2.4) and (5.2.5), with the corresponding initial and boundary conditions, define a problem in *strong form* which must be solved at each time step n .

That is, at each time step, the solution at time t^n , u^n , is assumed to be known and the partial differential equation (5.2.5), which only involves spatial derivatives, must be solved in order to obtain $\Delta \mathbf{u}$. Then, the solution at time t^{n+1} , u^{n+1} , is computed from u^n and $\Delta \mathbf{u}$.

Once the time discretization has been performed, both the mesh-free EFG interpolation or the finite element interpolation can be used in the discretization of the resulting partial differential equation, (5.2.4) or (5.2.5), at each time step. In the following section, the Galerkin formulation and the standard stabilization techniques are recalled in the context of the finite element interpolation. However, section 5.2.3 is devoted to the particularization these formulations for a mesh-free interpolation.

5.2.2 Spatial discretization. (I) Galerkin and stabilized formulations for the FE method

Application of the Galerkin formulation to the time stepping scheme (5.2.4) results in the following weak form

$$\left(\mathbf{v}, \frac{\Delta \mathbf{u}}{\Delta t}\right)_{\Omega} - (\mathbf{v}, \mathbf{W} \Delta \mathbf{u}_t)_{\Omega} = (\mathbf{v}, \mathbf{w} u_t^n)_{\Omega} \quad \forall \mathbf{v} \in [\mathcal{V}_0^h]^{\text{nsbg}}, \quad (5.2.8)$$

with \mathcal{V}_0^h subset of the usual functional space $\mathcal{H}_0^1 = \{v | v \in \mathcal{H}^1, v = 0 \text{ on } \partial\Omega \setminus \Gamma\}$ and the vector scalar product $(\mathbf{v}, \mathbf{u})_{\Omega} = \int_{\Omega} \mathbf{u} \cdot \mathbf{v} d\Omega$.

Note that the right-hand side of (5.2.8) is known, and that the second term of the left-hand side (i.e. $\Delta \mathbf{u}_t$) includes the Laplace operator, which is integrated by parts (see Donéa et al. 2000) for extended details).

In order to stabilize the convective term in a consistent manner (ensuring that the solution of the differential equation is also solution of the weak form), Hughes and coworkers have proposed several techniques (Hughes 1987, Shakib and Hughes 1991). An extra term weighted over the element interiors is added to the Galerkin weak form. This added term is a function of the residual of the differential equation to ensure consistency. These methods are designed for the steady convection-diffusion equation and subsequently extended to transient problems with second order time schemes and to space-time formulations. In (Huerta and Donéa 2001) and (Huerta, Roig and Donéa 2001) standard stabilization techniques are implemented with finite elements and high order time stepping schemes such as (5.2.4). The considered stabilization techniques are *streamline-upwind Petrov-Galerkin* (SUPG), *Galerkin least-squares* (GLS), *sub-grid scale* (SGS) and a *least-squares* (LS) type stabilization. Here, only the LS and the SUPG formulation are considered. However, generalization to other formulations is straightforward.

In order to have a consistent stabilization a residual must be defined. The residual in this case is chosen after time discretization. Thus, from (5.2.4) the residual is defined as

$$\mathcal{R}(\Delta \mathbf{u}) := \frac{\Delta \mathbf{u}}{\Delta t} - \mathbf{W} \Delta \mathbf{u}_t - \mathbf{w} u_t^n \quad (5.2.9)$$

and the consistently stabilized weak form is

$$\left(\mathbf{v}, \frac{\Delta \mathbf{u}}{\Delta t} \right)_\Omega - \left(\mathbf{v}, \mathbf{W} \Delta \mathbf{u}_t \right)_\Omega + \sum_e (\tau \mathcal{P}(\mathbf{v}), \mathcal{R}(\Delta \mathbf{u}))_{\Omega^e} = \left(\mathbf{v}, \mathbf{w} u_t^n \right)_\Omega. \quad (5.2.10)$$

Note that the stabilization term is added to the Galerkin weak form. In the stabilization term a free parameter τ appears (the intrinsic time scale, see (Shakib and Hughes 1991, Tezduyar and Osawa 2000)), and the operator \mathcal{P} characterizes the stabilization technique (see for instance (Codina 2000) for a general presentation). The truncation errors are not explicitly indicated: a term $\mathcal{O}(\Delta t^{2n_{stg}})$ can be added to (5.2.9) and (5.2.10). If the truncation error is neglected, the precision in time is characterized by the order of this error, depending on the particular scheme chosen.

The SUPG stabilization is defined by taking

$$\mathcal{P}(\mathbf{v}) := \mathbf{W}(a \cdot \nabla) \mathbf{v}. \quad (5.2.11)$$

Note that the matrix \mathbf{W} , which affects the convection term, induces a *non scalar* stabilization (each equation is affected by different coefficients). The weak form for the SUPG method is obtained after substitution of (5.2.11) in equation (5.2.10).

Remark 5.2.1. The stabilization term involves the residual, which includes the second-order term $\nabla^2 u$. When linear finite elements are used this term vanishes or is largely under-represented, with the corresponding degradation in the consistency of the stabilized formulation. The lack of consistency leads to errors of order $\mathcal{O}(\tau)$, i.e. the order of the neglected terms, added to the errors of the time integration scheme.

Remark 5.2.2. In order to keep the convergence rates in time, several possibilities can be useful. The stabilization parameter τ can be defined to be asymptotically of order $\mathcal{O}(\Delta t^{2n_{stg}})$. That is, a specific intrinsic time τ should be designed for each one of the time integration schemes. Other possibility is to include flux jump terms across the element boundaries in the stabilized formulation to take into account the neglected terms (see (Tezduyar and Osawa 2000) for details). In fact, reference (Jansen et al. 1999) shows that when linear finite elements are used the lack of consistency due to the neglected terms leads also to reduced convergence in space. For linear finite elements, it proposes a global reconstruction of second derivatives. This method recovers the ability to approximate the

residual in the stabilization term yielding a better consistency, through an iterative process. However, the increase in the computational cost is not negligible: a system of equations with global mass matrix must be solved at each iteration.

Remark 5.2.3. The use of high-order finite elements, such as quadratic elements, allows including second derivatives of the approximation in the residual in the stabilization term, and thus, consistent stabilized formulations can be defined. However, the computational cost and the implementation difficulties are highly increased due to the computation of second derivatives of the element mapping (Jansen et al. 1999).

To implement a *least-squares* (LS) formulation one uses directly the spatial strong form to construct the integral equation. Here, since time discretization is already performed, equations (5.2.4) and (5.2.5) are used. Consequently, one gets

$$\left(\frac{\mathbf{v}}{\Delta t} + \mathbf{W}\mathcal{L}(\mathbf{v}), \mathcal{R}(\Delta\mathbf{u})\right)_\Omega = 0. \quad (5.2.12)$$

The correct implementation of a standard least-squares formulation requires to work in \mathcal{H}^2 unless a mixed least-squares formulation is used, see (Carey, Pehlivanov, Shen, Bose and Wang 1998), and thus, \mathbf{v} and \mathbf{u} should be in subspaces of $[\mathcal{H}^2(\Omega)]^{\text{nstg}}$. However, an equivalent form which follows the same rationale as for standard stabilized methods, see equation (5.2.10), can be devised. It is equivalent in the sense that its unique solution is also the unique solution of (5.2.4) or (5.2.12). The first argument in (5.2.12) is split by linearity and the term containing $\mathcal{L}(\mathbf{v})$ is only evaluated in the element interiors, namely

$$(\mathbf{v}, \mathcal{R}(\mathbf{u}))_\Omega + \sum_e (\Delta t \mathbf{W}\mathcal{L}(\mathbf{v}), \mathcal{R}(\Delta\mathbf{u}))_{\Omega_e} = 0. \quad (5.2.13)$$

Note that in (5.2.13) the interpolation and tests functions can be taken in a subspace of $[\mathcal{H}^{1+}]^{\text{nstg}}$, where $\mathcal{H}^1 \subsetneq \mathcal{H}^{1+} := \{w \in \mathcal{H}^1(\Omega) / w|_{\Omega_e} \in \mathcal{H}^2(\Omega_e) \text{ for all element } \Omega_e\} \subsetneq \mathcal{H}^2$. The final formulation is still symmetric (note that this is not the case for other stabilization techniques such as SUPG, GLS or SGS), and now \mathcal{C}^0 finite elements can be used. This approach can also be cast in the form of a standard stabilization technique with the following definition of the operator \mathcal{P} and the intrinsic time τ

$$\tau\mathcal{P}(\mathbf{v}) := \Delta t \mathbf{W}\mathcal{L}(\mathbf{v}). \quad (5.2.14)$$

Remark 5.2.4. As in the standard stabilization techniques, some terms with second-order derivatives are neglected or under-represented when finite elements are considered to discretize the least-squares formulation. This leads to errors of order $\mathcal{O}(\Delta t)$ added to the errors of the time integration scheme.

5.2.3 Spatial discretization. (II) Galerkin and stabilized formulations for the EFG method

The EFG interpolation, see section 2.1.2, can also be considered in the spatial discretization of the Galerkin weak form (5.2.8). However, in the presence of internal or boundary layers the typical instabilities of the Galerkin formulation will soon appear. In fact, all the considered stabilized formulations (5.2.10) can be discretized with the mesh-free interpolation. Moreover, with a mesh-free method, the interpolation space is a subset of $\mathcal{H}^2(\Omega)$ (see remark 2.1.15), and thus, this other equivalent expression for the stabilized formulations (5.2.10) can be considered

$$\left(\mathbf{v}, \frac{\Delta \mathbf{u}}{\Delta t}\right)_\Omega - \left(\mathbf{v}, \mathbf{W} \Delta \mathbf{u}_t\right)_\Omega + (\tau \mathcal{P}(\mathbf{v}), \mathcal{R}(\Delta \mathbf{u}))_\Omega = \left(\mathbf{v}, \mathbf{w} u_t^n\right)_\Omega. \quad (5.2.15)$$

Note that, since the interpolation is performed in $\mathcal{H}^2(\Omega)$, the integration of the stabilization term can be done in the whole domain Ω . Moreover, the natural expression of the least-squares formulation (5.2.12) in $\mathcal{H}^2(\Omega)$ can be performed.

Remark 5.2.5. Note that, with the EFG interpolation space, second-order derivatives are well represented (see remark 2.1.15), and thus, consistent stabilized formulations can be easily implemented. In fact, there are two possible advantages of the mesh-free interpolation in the resolution of the transient convection-diffusion equation: (1) the order of consistency can be easily increased, and thus, high-order (in both space and time) formulations can be implemented in a simple way, and (2) the smoothness of the interpolant allows the definition of consistent stabilized formulations. There are no neglected terms and thus the convergence rates of the time integration schemes are preserved.

Remark 5.2.6 (Computation of derivatives). Belytschko and coworkers proposed in (Belytschko, Krongauz, Fleming, Organ, and Liu 1996) an efficient computation of the derivatives of the shape functions, see section 2.2.4. It is based on implicit derivation of (2.1.29). For example, in 1D the first and second derivatives of the shape function (2.1.27) can be expressed as

$$\frac{dN_i}{dx} = \mathbf{P}^T(x_i) \left[\boldsymbol{\alpha}_x(x) \phi\left(\frac{x-x_i}{\rho}\right) + \boldsymbol{\alpha}(x) \frac{1}{\rho} \phi_x\left(\frac{x-x_i}{\rho}\right) \right],$$

$$\frac{d^2N_i}{dx^2} = \mathbf{P}^T(x_i) \left[\boldsymbol{\alpha}_{xx}(x) \phi\left(\frac{x-x_i}{\rho}\right) + 2\boldsymbol{\alpha}_x(x) \frac{1}{\rho} \phi_x\left(\frac{x-x_i}{\rho}\right) + \boldsymbol{\alpha}(x) \frac{1}{\rho^2} \phi_{xx}\left(\frac{x-x_i}{\rho}\right) \right],$$

where \square_x denotes de derivative $\frac{d\square}{dx}$. Vectors $\boldsymbol{\alpha}_x$ and $\boldsymbol{\alpha}_{xx}$ can be obtained solving two small linear system of equations

$$\mathbf{M} \boldsymbol{\alpha}_x = \mathbf{P}_x - \mathbf{M}_x \boldsymbol{\alpha}, \quad \mathbf{M} \boldsymbol{\alpha}_{xx} = \mathbf{P}_{xx} - \mathbf{M}_{xx} \boldsymbol{\alpha} - 2\mathbf{M}_x \boldsymbol{\alpha}_x,$$

which are easily deduced by implicit derivation of (2.1.29). Note that matrix $\mathbf{M} \in \mathbb{R}^{(l+1) \times (l+1)}$ and its factorization has been computed previously in order to obtain vector $\boldsymbol{\alpha}$, so computation of first and second derivatives only involves the resolution of two small systems of equations through two backward and forward substitutions. Second derivatives of the shape functions can be easily computed in EFG with negligible extra computational cost.

5.3 Convergence of the Galerkin approach and the stabilized formulations

In this section, a numerical example is considered in order to analyze the convergence in time of the presented formulations and corroborate the conclusions derived in from section 5.2. The 1D convection-diffusion equation with constant coefficients is solved,

$$u_t + au_x = \nu u_{xx}, \quad x \text{ in } (0, 2), \quad t \text{ in } (0, 1),$$

with homogeneous Dirichlet boundary conditions. The initial condition, at $t = 0$, is chosen such that the analytical solution is known

$$u(x, t) = \frac{\sigma_0}{\sigma} e^{-\frac{(x-(x_0+at))^2}{2\sigma^2}}, \quad \sigma^2 = \sigma_0^2 + 2\nu t.$$

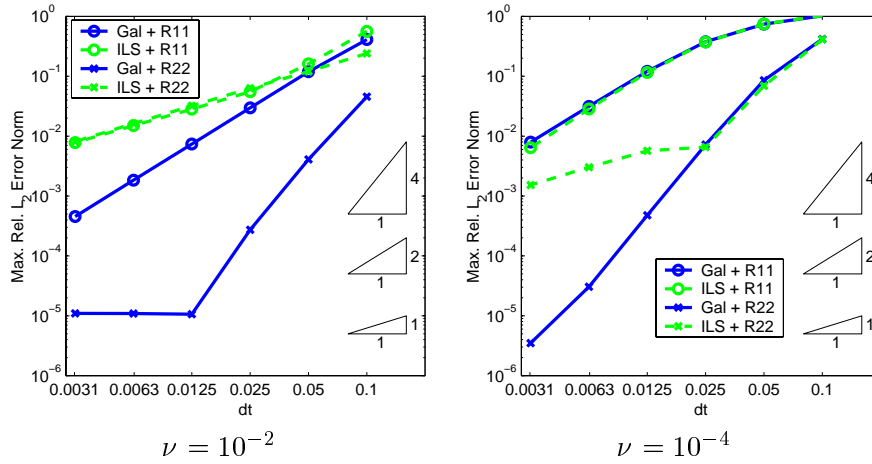


Figure 5.1: Finite elements convergence results with $h = 0.001$ and $a = 1$.

Both finite elements and particle results are studied. Figure 5.1 shows the evolution of the error against the time step for linear finite elements, with element size $h = 0.001$, and for two different values of the diffusion parameter ν . In all figures the error is evaluated

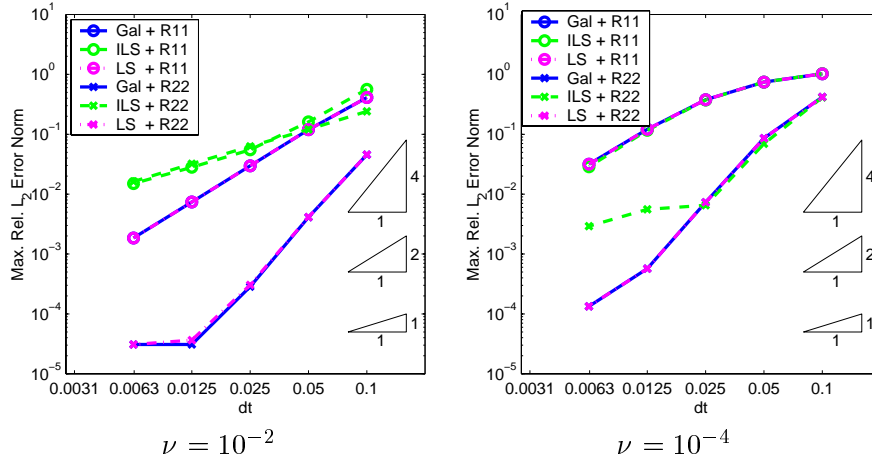


Figure 5.2: EFG convergence results with $h = 0.01$ (distance between particles), $\rho/h = 3.2$, $\mathbf{P} = \{1, x\}^T$ and $a = 1$.

in the $\mathcal{L}^2(\Omega)$ norm. In each plot, results are shown for the Galerkin and the Least-squares formulation with two different Padé time stepping schemes: R_{11} and R_{22} with order two and four respectively. The convergence rates are as expected when a Galerkin formulation is used. However, when the least-squares formulation (5.2.13) is used, the lack of consistency due to the neglected terms leads to errors of order $\mathcal{O}(\Delta t)$, with the corresponding degradation in the convergence rates. When the truncation error of the time integration scheme is small enough, the error is only $\mathcal{O}(\Delta t)$, instead of $\mathcal{O}(\Delta t^2)$ or $\mathcal{O}(\Delta t^4)$. In all figures ILS denotes the *incomplete least-squares* formulation, that is, the particularization of the least-squares formulation (5.2.13) for linear finite elements, and thus, with some neglected terms.

Figure 5.2 shows the convergence results for the EFG interpolation with linear consistency, distance between particles $h = 0.01$ and $\rho/h = 3.2$. Results are depicted for the Galerkin formulation, the consistent least-squares formulation (5.2.12) and the non-consistent ILS formulation. Once again, the ILS formulation corresponds to the weak form with the same $\mathcal{O}(\Delta t)$ neglected terms as with linear finite elements in figure 5.1. The convergence rates of the time stepping schemes are preserved when a consistent weak form is used. In fact, the convergence curves coincide with the Galerkin convergence curves. In this case convergence is as expected with both formulations: Galerkin and least-squares. Moreover, convergence degrades, as in the finite elements results, if the non consistent formulation ILS is used.

In order to preserve the high-order convergence rates of the time stepping schemes, a

consistent formulation must be used. With a mesh-free method, such as EFG, second order derivatives of the interpolation are well defined in the whole domain, and thus, consistent stabilized formulations, without neglected terms, can be easily defined and implemented.

Remark 5.3.1. Note that the spatial discretization limits the precision. That can be observed in the Galerkin case with the R_{22} scheme and $\nu = 10^{-2}$. Moreover, note that with the mesh-free interpolation it is enough to discretize the domain with 201 particles in order to obtain an accuracy in space similar to the accuracy with 2000 finite elements, more or less 10^{-5} . That is, a number of degrees of freedom ten times smaller in EFG than in finite elements. Recall that with linear consistency the finite element shape functions can be recovered from the EFG shape functions when $\rho/h \simeq 1$ (see figure 2.5) and, in most of the problems, the EFG interpolation with big enough ratio, for example $\rho/h = 3.2$, performs better than the finite element interpolation. In fact, for each problem an optimal value for the ratio ρ/h can be found (see for instance the numerical examples in chapter 3).

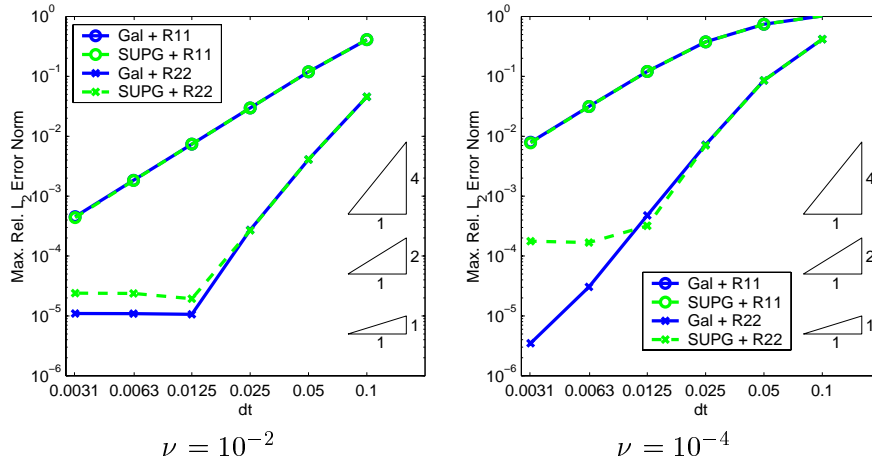
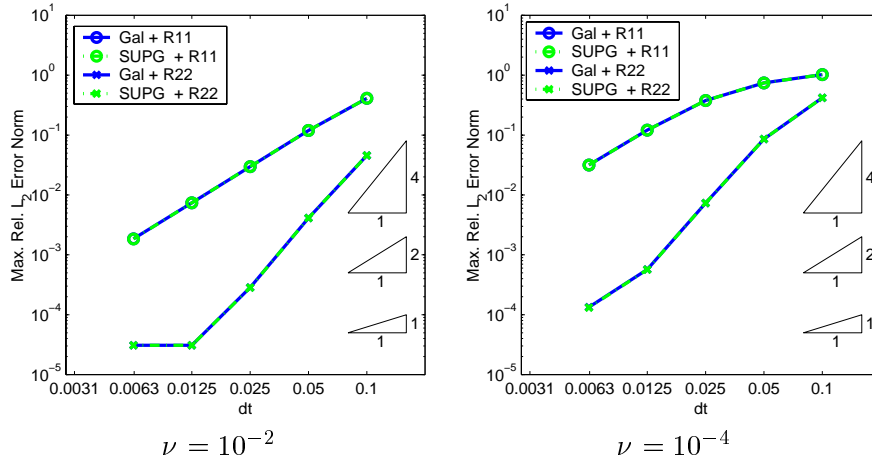
Similar results are obtained for the SUPG stabilized formulation, see figures 5.3 and 5.4. When finite elements are used, the intrinsic time τ is computed using the formula proposed in (Shakib and Hughes 1991), see (Tezduyar and Osawa 2000) for an interesting review, that is

$$\tau = \tau_{\text{FE}} := \frac{\Delta t}{2} \left(1 + \left(\frac{a\Delta t}{h} \right)^2 + 36 \left(\frac{\nu\Delta t}{h^2} \right)^2 \right)^{-\frac{1}{2}}. \quad (5.3.1)$$

Note that h can be interpreted as a measure of the radius of the support of the FE shape functions, equivalent to the dilation parameter ρ in EFG. So, when the EFG interpolation is considered the intrinsic time is computed with the same expression (5.3.1) just replacing the element size h by the dilation parameter ρ , that is,

$$\tau = \tau_{\text{EFG}} := \frac{\Delta t}{2} \left(1 + \left(\frac{a\Delta t}{\rho} \right)^2 + 36 \left(\frac{\nu\Delta t}{\rho^2} \right)^2 \right)^{-\frac{1}{2}}. \quad (5.3.2)$$

Once again, when particles are used, the consistent SUPG formulation in $\mathcal{H}^2(\Omega)$ (5.2.15) preserves the convergence rates of the time integration scheme (see figure 5.4). On the other hand, when linear finite elements are used, results can be degraded due to the neglected $\mathcal{O}(\tau)$ terms in (5.2.10) (see figure 5.3). For, $\nu = 10^{-2}$ the intrinsic time τ is small enough so that the effect of this $\mathcal{O}(\tau)$ error is negligible in comparison with the truncation errors of the R_{11} time stepping scheme and almost negligible with the R_{22} scheme. However, for the more convective problem with $\nu = 10^{-4}$, the error $\mathcal{O}(\tau)$ reduces drastically the convergence rates: the error is of order $\mathcal{O}(\tau)$ when the truncation errors of the time stepping schemes are small enough.

Figure 5.3: Finite elements convergence results with $h = 0.001$ and $a = 1$.Figure 5.4: EFG convergence results with $h = 0.01$, $\rho/h = 3.2$, $\mathbf{P} = \{1, x\}^T$ and $a = 1$.

5.4 Numerical examples

There are two important topics in the resolution of the transient convection-diffusion equation: (1) accurate transport of the unknown quantity u is necessary, and thus, high-order time stepping schemes are needed, and (2) in the presence of boundary or internal layers, it is necessary to stabilize the solution in order to avoid oscillations. Sections 5.2.3 and 5.3 already discussed how the smoothness of the EFG interpolation allows to easily define stabilized formulations in a consistent manner and preserve the convergence rates of the high-order time stepping schemes. In this section, some numerical examples are shown in order to see the influence of the different stabilization techniques and the time stepping

schemes in the numerical solution with EFG.

The first example is a 1D example whose solution tends to a stationary convection dominated solution. Therefore, the same problems of the stationary equation, that is boundary layers, are present in the transient solution and thus stabilized formulations are needed.

The second example is a 2D example where both problems of the transient convection-diffusion equation are present: (1) accurate transport of the unknown is needed and (2) boundary layers appear in the solution due to the Dirichlet boundary conditions. Therefore, high-order time stepping schemes and stabilized formulations are needed in order to obtain an accurate solution.

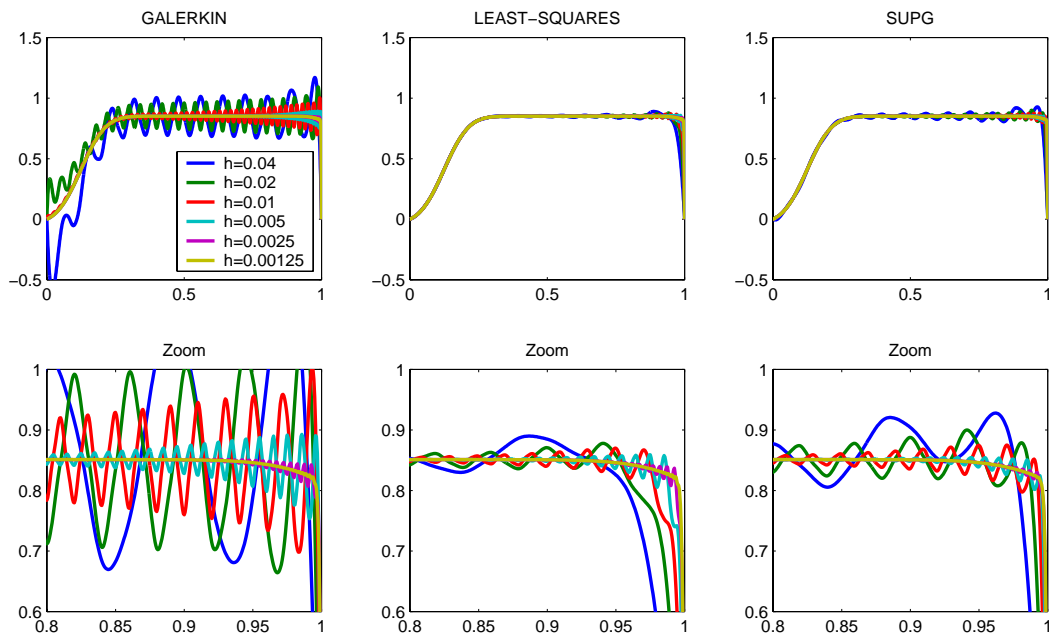


Figure 5.5: R_{11} solution at $t = 1$ for $a = 1$, $\nu = 10^{-3}$, $\rho/h = 3.2$ with $c = 1$

5.4.1 1D example

The transient convection-diffusion equation, $u_t + au_x = \nu u_{xx} + s$, is solved in $[0, 1]$ with velocity $a = 1$, diffusion $\nu = 10^{-3}$, initial condition $u(x, 0) = 0$, homogeneous Dirichlet boundary conditions and source term $s(x) = 5e^{-(10(x-\frac{1}{8}))^2}$.

The time step Δt is chosen such that the Courant number $c := a\Delta t/h$ is $c = 1$ for the R_{11} scheme and $c = 2$ for the R_{22} scheme, where h is the distance between particles.

Figures 5.5 and 5.6 show the solution at $t = 1$ obtained with the R_{11} and the R_{22} time stepping schemes. The Galerkin solution suffers from the typical oscillations in the presence

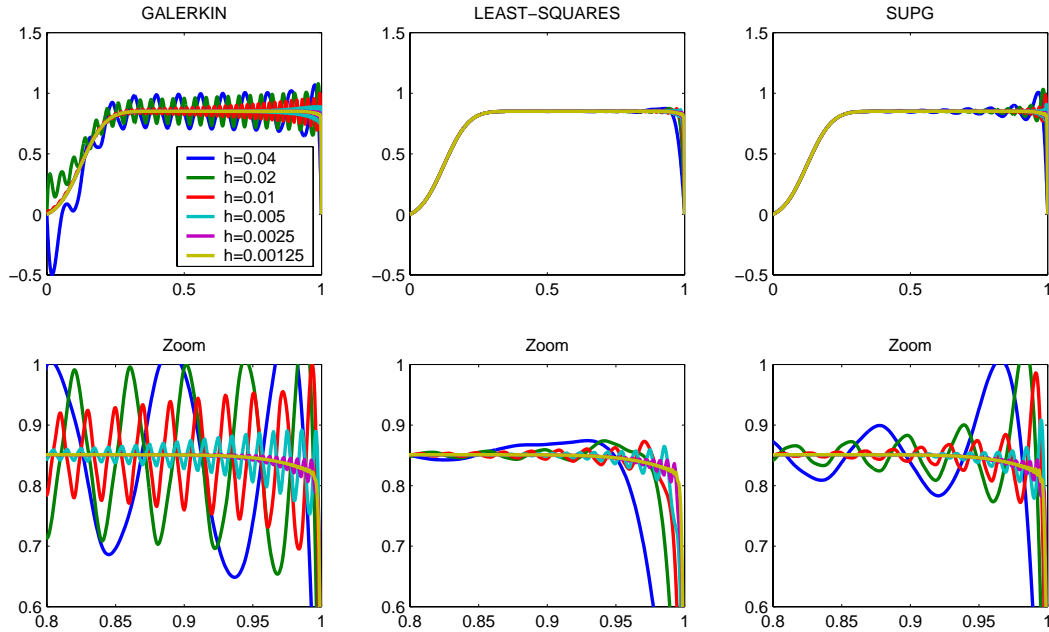


Figure 5.6: R_{22} solution at $t = 1$ for $a = 1$, $\nu = 10^{-3}$, $\rho/h = 3.2$ with $c = 2$

of boundary layers and stabilization techniques are necessary to improve the solution. As can be seen from the results, the diffusion added with the least-squares stabilization is larger than with the SUPG technique: it is easy to see that $\tau_{\text{SUPG}} \leq \tau_{\text{LS}} = \Delta t$ when formula (5.3.2) is used to compute τ_{SUPG} . The best result is obtained with the high-order time integration scheme R_{22} and the least-squares stabilization.

5.4.2 2D example

The 2D problem described in figure 5.7 is solved with small diffusion, $\nu = 10^{-5}$. The source term and the velocity field are defined as follows:

$$\mathbf{a} = (-(y-0.5), (x-0.5)) \quad s = e^{-t^{10}} \begin{cases} \cos(\pi/2\sqrt{x^2 + y^2}) & \text{if } \sqrt{x^2 + y^2} \leq 1 \\ 0 & \text{otherwise} \end{cases}$$

Figures 5.8 and 5.9 show the numerical solution obtained at $t = 15.9$ for the Galerkin and the least-squares formulations, with a 21×21 distribution of particles, $\rho/h = 3.2$ and linear consistency. The R_{11} and R_{22} time integration schemes have been used with Courant 1 and 3 respectively. Different sections of the obtained numerical solutions at $t = 15.9$ are depicted in figures ?? and ??.

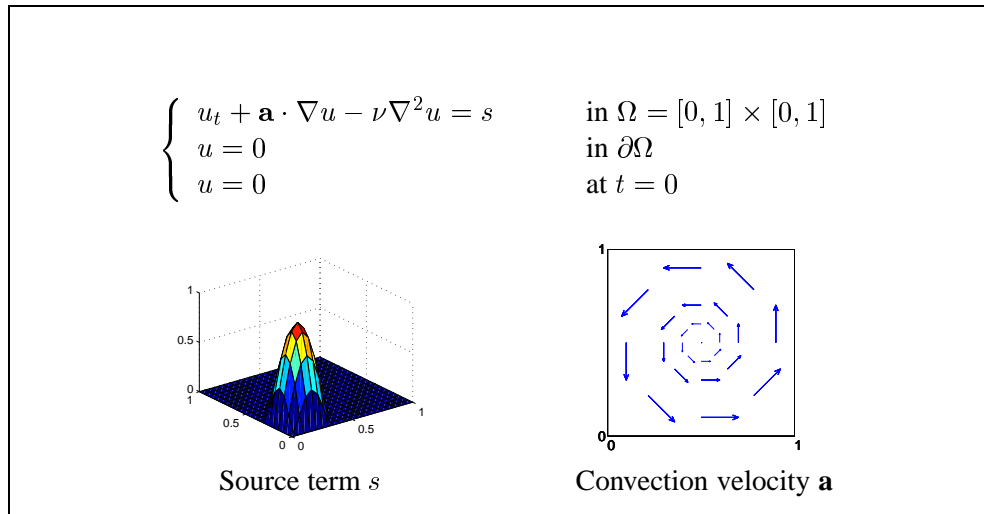
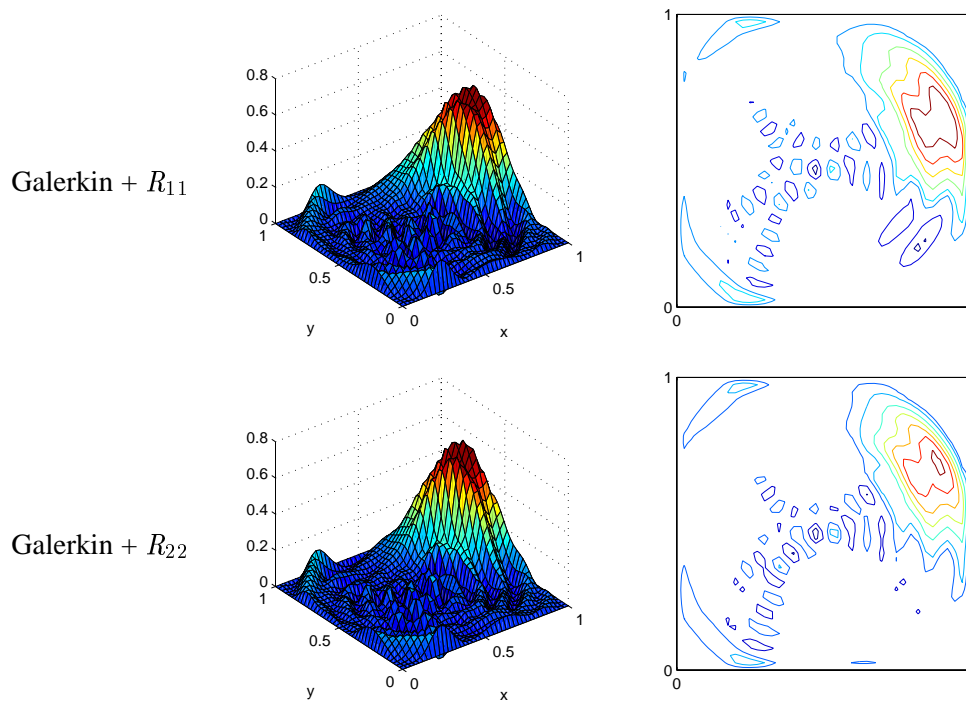


Figure 5.7: Problem statement for the 2D example

Figure 5.8: Galerkin solution and contour plot at $t = 15.9$ for $\nu = 10^{-5}$, $h = 0.05$, $\rho/h = 3.2$ with $c = 1$ for R_{11} and $c = 3$ for R_{22}

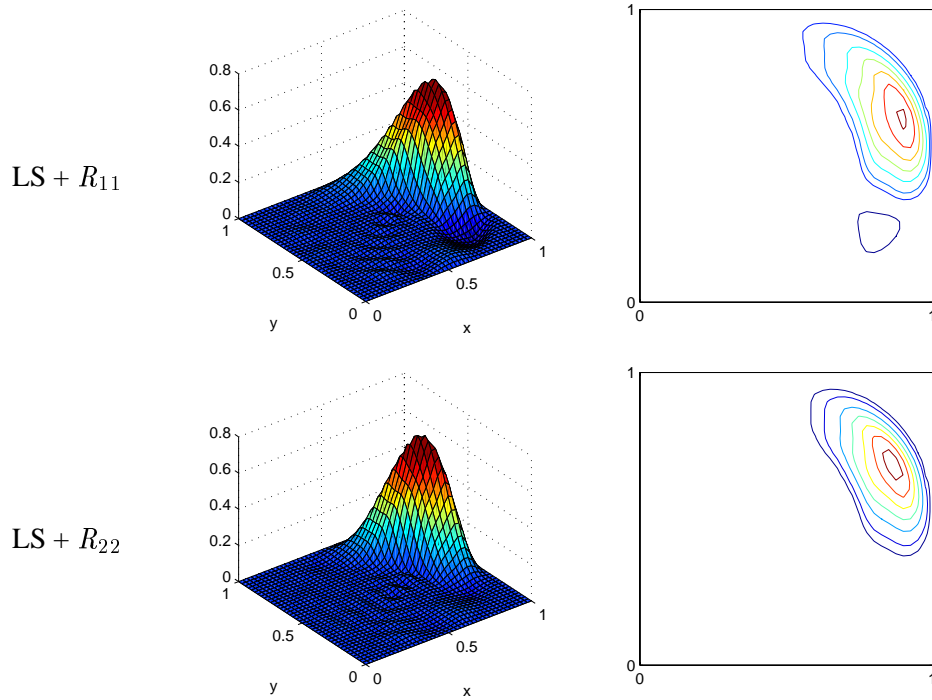
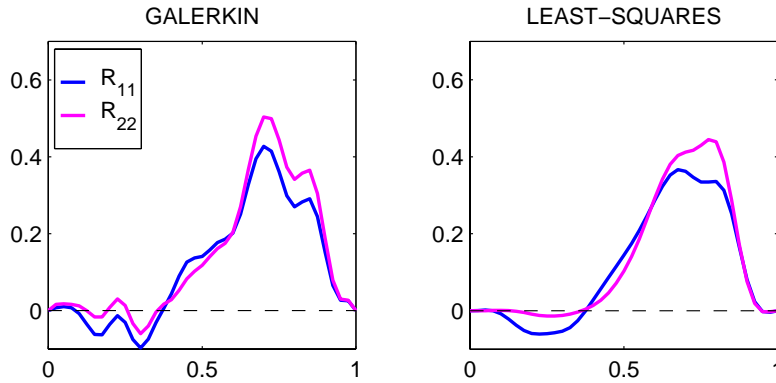
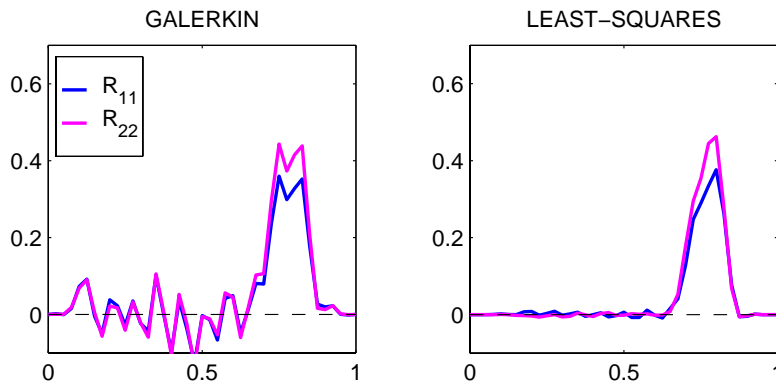


Figure 5.9: Least-squares solution and contour plot at $t = 15.9$ for $\nu = 10^{-5}$, $h = 0.05$, $\rho/h = 3.2$ with $c = 1$ for R_{11} and $c = 3$ for R_{22}

Boundary layers are present in the solution due to the convective character of the equation and the homogeneous Dirichlet boundary conditions. Thus, the typical instabilities of the Galerkin formulation soon appear. The numerical solution is clearly improved for the stabilized least-squares formulation: oscillations are alleviated and almost suppressed in the whole domain. However, important phase and amplitude errors can be observed in the numerical solution obtained for the R_{11} time stepping scheme. In figure ??, it is easy to see that the R_{11} solution presents negative values, with no physical sense. Obviously, the high-order R_{22} scheme provides a much better solution.

5.5 Concluding remarks

In this chapter, the formulation proposed in (Huerta and Donéa 2001) for transient convection-diffusion problems is used in the context of mesh-free methods. By performing the time discretization before the spatial one, standard stabilization techniques can be adapted to high-order time stepping schemes. However, with linear finite elements the lack of con-

Figure 5.10: Section along $x = 0.8$ Figure 5.11: Section along $y = x$

sistency due to neglected terms (terms with second order spatial derivatives) may degrade the convergence rates of the time integration scheme. In order to keep the high-order convergence rates the intrinsic time τ should be adapted to each time integration scheme or second derivatives should be globally reconstructed, with the corresponding increase in the computational cost.

This chapter proposes to perform the spatial discretization using mesh-free interpolation functions. With the EFG method, second derivatives of the approximation can be computed with negligible extra computational cost. The mesh-free interpolation space is a subset of $\mathcal{H}^2(\Omega)$ and thus, the standard stabilization techniques can be particularized for the EFG interpolation in $\mathcal{H}^2(\Omega)$. There are not neglected terms and the convergence rates of the high-order time integration schemes are preserved. Moreover, in EFG the order of the space discretization can be increased in a simple way. With a mesh-free interpolation, space and time high-order consistent stabilized formulations are easily defined and implemented.

Chapter 6

Summary and future developments

As noted in the introduction, although mesh-free methods are advantageous in many interesting situations, the popularization of these methods still requires further research. This thesis deals with the numerical analysis of mesh-free methods and, in particular, with the study of possible advantages and interesting applications of the EFG method.

The most relevant contributions of this thesis are the following.

1. Many mesh-free methods can be found in the literature which can be based on different ideas and with different properties. There is a real need of classifying, ordering and comparing these methods: in fact, the same or almost the same method can be found with different names in the literature. So, first of all, this thesis dedicates one chapter to the **state of the art of mesh-free methods**, with special emphasis on the EFG method and its properties and implementation. Although a good state of the art can be found in (Belytschko, Krongauz, Organ, Fleming and Krysl 1996), chapter 2 completes it including other mesh-free methods, such as the family of improved SPH methods, and comparing all of them. In fact, two families of mesh-free methods can be considered: the SPH method and its improved versions and the methods based on moving least-squares developments. In each one of this families several similarities can be found between different methods.
2. The behaviour of mesh-free methods and its comparison with the classical finite element method is still an open topic in many situations. In this thesis this comparison is performed in the framework of two relevant problems, with interesting conclusions.
 - ▷ Chapter 3 is devoted to the study of **volumetric locking** in the EFG method. As can be found in the literature, volumetric locking can drastically degrade the

finite element solution in mechanical computations. Although it was originally claimed that the EFG method does not suffer from locking, chapter 3 demonstrates that it is not true. A modal analysis has been used to study volumetric locking in the EFG method and some numerical examples have been used to corroborate the conclusions. Basically, the EFG method with linear consistency presents the same volumetric locking modes as linear finite elements. Although locking alleviates when the support of the shape functions increases, the same problems will occur in the incompressible limit. The influence of the order of consistency is also studied: for practical purposes in EFG an *hp* strategy can be implemented in a very simple way and, as in finite elements, will also suppress locking.

- ▷ The behaviour of mesh-free methods has also been studied in the context of **convection dominated problems**, with special emphasis on the transient case. In chapter 5 the formulation proposed in (Huerta and Donéa 2001) for transient convection-diffusion problems is used in the context of mesh-free methods. The advantages of the EFG method in comparison with the finite element method are studied in this context. With linear finite elements the lack of consistency due to neglected terms (terms with second order spatial derivatives) may degrade the convergence rates of the time integration scheme, unless specific techniques are considered with the corresponding increase in the computational cost and implementation difficulty. However, with the EFG method, second derivatives of the approximation can be computed with negligible extra computational cost. This allows the definition of space and time high-order consistent stabilized formulations, preserving the high order convergence rates. Some examples can also be found for the stationary case in section 4.5.5.

3. Although, this thesis shows how mesh-free methods perform much better than mesh-based methods in some situations, the finite element method is still more competitive in many other situations. In order to take advantage of the good properties of both methods, a **mixed interpolation combining the EFG method and the finite element method** is developed in chapter 4. Several authors have proposed to use this kind of mixed interpolations, however, in this thesis a unified and general formulation is presented. This formulation can be applied in two useful situations: enrichment and coupling. An *a priori error estimate* for the first one is proved in appendix A. As it was commented in the introduction, both applications can be useful in adaptive

processes: a coarse finite element mesh can be used in the whole domain and, after the use of an error estimator or indicator, some particles can be added freely where it is needed, with no remeshing cost. The applicability of this mixed interpolation is shown in several examples.

However, mesh-free methods are still novel methods, and thus, there are many topics about mesh-free methods that still require further research. Here some interesting research topics are proposed.

1. As noted in the introduction, at this moment one of the most important objectives is to take advantage of the ability of mesh-free methods in adaptivity processes. In particular, mesh-free methods present several good properties in convection dominated problems (see chapter 5), and thus, the application of the **mixed interpolation** presented in chapter 4 in the **simulation of active carbon canisters** seems very promising. The basic idea is to use a fixed coarse finite element mesh in the whole domain, with a cloud of moving particles following the moving front in order to increase the spatial accuracy where it is needed.
2. Imposing **essential boundary conditions** in a efficient and accurate way is other interesting topic. Section 2.2.3 recalls the most important techniques. However, there is not a comparison between them in terms of accuracy, computational cost and implementation difficulty. For instance, for the Lagrange multipliers method it is not easy to choose the optimal number of Lagrange multipliers: the boundary conditions are imposed in a not enough accurate way if too few multipliers are used and, on the other hand, the total system of equations becomes singular if too many multipliers are considered. So, it can be interesting to compare and study the different existing techniques. On the other hand, the idea of the mixed interpolation combining finite elements in the essential boundaries and particles in the rest of the domain could be applied, and may be improved, for this purpose.
3. Mesh-free methods presents obvious advantages in adaptive processes. So, it is also important to work in this research field.
 - ▷ In order to define an adaptive refinement strategy, as it is commented in (Huerta et al. 1999), an *a priori* error estimator and an *a posteriori* error estimator or error indicator are needed. Although there are *a priori* error estimates for most of the mesh-free methods, see for instance (Liu et al. 1997), there are not good *a*

posteriori error estimators. So, it necessary to investigate on this topic in order to define efficient adaptive strategies and ensure the accuracy of the calculations.

- ▷ Adaptive computations in transient problems can be easily done following the idea of Moving Finite Elements (MFE), see (Baines 1994). The basic idea of MFE is to adapt the finite element mesh at each time step in order to minimize the residual of the partial boundary value problem. The topology of the mesh is kept fixed and the position of the nodes are considered variables, (as well as the value of the solution at this nodes) in the minimization of the residual. However, in 2D and 3D computations the minimization usually leads to distorted elements or not well defined meshes. In this situation, specific techniques must be used in order to maintain a well defined mesh, with the corresponding increase in the implementation difficulty. Particle methods do not require connectivities, and thus there are no problems with distorted or badly defined meshes. So, may be MFE should evolve towards the "**Moving Particles**" method.
4. Other interesting research topic is the development of new mixed interpolations combining finite elements and mesh-free methods. The convergence results in the **enrichment of finite elements with particles** are not as good as it was originally expected, see section 4.4: when a coarse finite element mesh is fixed the error does not go to zero if only the number of particles is increased. May be the consistency condition 4.2.6 is too restrictive and other possibilities should be considered. On the other hand, the consistency condition can be imposed to reproduce non-polynomial functions. The finite element contribution in (4.2.3) can take care of the consistency while the mesh-free enrichment takes care of the reproducibility of more suitable functions in each particular problem, for instance trigonometric functions or logarithmic functions.
 5. Moreover, it is also necessary to compare finite elements with mesh-free methods in other problems, in order to determine other situations where mesh-free methods can be advantageous and explore all the possibilities of these methods.

Appendix A

Convergence of finite elements enriched with mesh-free methods

Here the convergence of the mixed interpolation presented in chapter 4 is analysed for the second case, that is, h - p enrichment of finite elements with particles (see section 4.4). This method allows to enrich the FE discretization everywhere adding particles and increasing the order of consistency. Recall that p is the degree of the finite element interpolation, and m is the order of consistency obtained with the added particles. Thus, the increment of consistency q is such that

$$q := m - p.$$

First, two results of EFG (Lemma A.1.1 and Lemma A.1.2), which are also valid for the proposed interpolation, are recalled. A proof of Lemma A.1.1 can be found in (Liu et al. 1997). Although a result similar to Lemma A.1.2 may also be found in (Liu et al. 1997), here a proof of Lemma A.1.2 is presented. Second, some properties of the FE basis are proved. Finally, a theorem that shows an *a priori* error estimate for such a mixed method is presented. This error estimate is proved under certain assumptions on the size of the finite elements (Theorem A.3.4). If this assumptions are not fulfilled, a less sharp error estimate is also found. This kind of error estimates are required to both study the convergence of the mixed method and design proper adaptive strategies.

A.1 Previous results

Lemma A.1.1 (Generalized consistency condition). *Let some functions $N_i \in \mathcal{C}^\ell$ verify the m -order consistency condition*

$$\sum_i (x - x_i)^r N_i(x) = \begin{cases} 0 & 0 < r \leq m \\ 1 & r = 0, \end{cases}$$

then for every r , $0 \leq r \leq m$, the functions N_i verify

$$\sum_i (x - x_i)^r \frac{d^k N_i}{dx^k}(x) = \begin{cases} 0 & r \neq k \\ r! & r = k, \end{cases}$$

for all k such that $0 \leq k \leq \ell$.

In the remainder of the paper the following hypothesis for the particle distribution is assumed to hold.

Hypothesis A.1.1. *In the refinement process, that is as ρ goes to 0, the particle distribution is homothetically densified. This is done ensuring that the particles belonging to a neighbourhood of x of radius ρ keep the same pattern during the refinement. Moreover, this pattern is such that matrix \mathbf{M} is regular (see remark 2.1.11).*

In order to clarify this hypothesis the following notation is introduced. Let I_x^ρ be, for every $x \in \Omega$, the set of indices of the particles in the support of the window function centred in x , i.e.

$$I_x^\rho := \{j \in I^\rho \text{ such that } |x_j - x| \leq \rho\}.$$

The pattern of normalized neighbour particles is defined to be

$$\Lambda_x^\rho := \{z_j := \frac{x - x_j}{\rho} \text{ for } j \in I_x^\rho\}.$$

Thus, Hypothesis A.1.1 is equivalent to assume that, passing from $\rho = \hat{\rho}$ to $\rho = \bar{\rho}$, for every $\tilde{x} \in \Omega$ it exists $\hat{x} \in \Omega$ such that $\Lambda_{\tilde{x}}^{\bar{\rho}} = \Lambda_{\hat{x}}^{\hat{\rho}}$. Consequently, $\mathbf{M}(\hat{x})|_{\rho=\hat{\rho}} = \mathbf{M}(\tilde{x})|_{\rho=\bar{\rho}}$ and the properties of \mathbf{M} are independent of ρ .

Lemma A.1.2. *Let Ω be an open bounded domain and $\phi \in \mathcal{C}^\ell(\Omega)$, $\ell \leq m$. Then, for all $x \in \Omega$, every element of matrix $\mathbf{M}^{-1}(x)$, the inverse of $\mathbf{M}(x)$, see (2.1.34), is bounded by a constant independent of x and ρ . Moreover, the k -th derivative ($k \leq \ell$) of every element of \mathbf{M} is $\mathcal{O}(\rho^{-k})$.*

Proof. The first part of the Lemma, *i.e.* $\mathbf{M}^{-1}(x)$ is bounded, is a direct consequence of Hypothesis A.1.1. The k -th derivative of $\mathbf{M}(x)$ is rearranged using the normalized variable z :

$$\begin{aligned} \frac{d^k}{dx^k} \mathbf{M}(x) &= \sum_{j \in I^\rho} \frac{d^k}{dx^k} \left[\mathbf{P} \left(\frac{x - x_j}{\rho} \right) \mathbf{P}^T \left(\frac{x - x_j}{\rho} \right) \phi \left(\frac{x - x_j}{\rho} \right) \right] \\ &= \rho^{-k} \sum_{j \in I_x^\rho} \frac{d^k}{dz^k} \left[\mathbf{P}(z) \mathbf{P}^T(z) \phi(z) \right] \Big|_{z=(x-x_j)/\rho} \end{aligned}$$

Under the assumption of Hypothesis A.1.1 the term

$$\sum_{j \in I_x^\rho} \frac{d^k}{dz^k} \left[\mathbf{P}(z) \mathbf{P}^T(z) \phi(z) \right] \Big|_{z=(x-x_j)/\rho}$$

is independent of ρ and therefore the Lemma is proved. \square

Remark A.1.1. In what follows, $\|\cdot\|_\infty$ stands for both the maximum norm of a vector and the subordinate matrix norm (“max row sum”). Note that the standard norm denoted by $\|\cdot\|_{\mathcal{L}_\infty}$, associated with the linear space \mathcal{L}_∞ , is also used later.

Corollary A.1.3. *Under the assumptions of Lemma A.1.2, constants $C^{\mathbf{M}}$ and $C_k^{\mathbf{M}}$ ($k = 0, \dots, \ell$) independent of x and ρ , exist and are such that*

$$\|\mathbf{M}^{-1}(x)\|_\infty \leq C^{\mathbf{M}}, \quad \text{and} \quad \left\| \frac{d^k \mathbf{M}}{dx^k} \right\|_\infty \leq C_k^{\mathbf{M}} \rho^{-k}, \quad k = 0, \dots, \ell.$$

Proof. Trivial given the definition of the matrix norm subordinate to the maximum vector norm. \square

A.2 FE element properties

Definition A.2.1. Let $R_\ell^{(k)}(x)$, $0 \leq k \leq p$, be the k -th derivative of the remainder (point-wise error) in the finite element interpolation of the monomial x^ℓ :

$$R_\ell^{(k)}(x) := \frac{d^k}{dx^k} \left[x^\ell - \sum_{i \in I^h} x_i^\ell N_i^h(x) \right] = \frac{d^k(x^\ell)}{dx^k} - \sum_{i \in I^h} x_i^\ell \frac{d^k N_i^h}{dx^k}(x).$$

In order to simplify the notation, the explicit dependence of $R_\ell^{(k)}$ on x is omitted. If finite elements of order p are used, in each element $R_\ell^{(k)}$ can be rewritten (Isaacson and Keller 1966) as:

$$R_\ell^{(k)} = \begin{cases} 0 & 0 \leq \ell \leq p \\ \frac{\ell! L^k(x) \xi^{\ell-(p+1)}}{(\ell-(p+1))! (p+1-k)!} & p < \ell \leq m, \end{cases} \quad (\text{A.2.1})$$

where $\xi = \xi(x)$ is an unknown point inside the finite element where x is located, where

$$L^k(x) = \prod_{j=0}^{p-k} (x - \eta_j), \quad (\text{A.2.2})$$

and the $p + 1 - k$ distinct and unknown points, η_j , lie inside the finite element.

Lemma A.2.1. *For $k = 0, \dots, p$, the p -order finite element basis verifies*

$$\sum_{i \in I^h} (x - x_i)^r \frac{d^k N_i^h}{dx^k}(x) = 0, \quad \text{for } r = 1, \dots, p \text{ and } r > k, \quad (\text{A.2.3})$$

and

$$\left| \sum_{i \in I^h} (x - x_i)^r \frac{d^k N_i^h}{dx^k}(x) \right| \leq \mu_{r,k} h^{r-k}, \quad \text{for } r \geq p + 1 > k, \quad (\text{A.2.4})$$

where

$$\mu_{r,k} := \frac{r!}{(r - (p + 1))! (p + 1 - k)!}.$$

Proof. The l.h.s. of (A.2.3) is rearranged using the Newton's binomial expression:

$$\begin{aligned} \sum_{i \in I^h} (x - x_i)^r \frac{d^k N_i^h}{dx^k}(x) &= \sum_{i \in I^h} \left[\sum_{\ell=0}^r (-1)^\ell \binom{r}{\ell} x_i^\ell x^{r-\ell} \right] \frac{d^k N_i^h}{dx^k}(x) \\ &= \sum_{\ell=0}^r (-1)^\ell \binom{r}{\ell} x^{r-\ell} \left[\sum_{i \in I^h} x_i^\ell \frac{d^k N_i^h}{dx^k}(x) \right] \\ &= \sum_{\ell=0}^r (-1)^\ell \binom{r}{\ell} x^{r-\ell} \left[\frac{d^k}{dx^k} (x^\ell) - R_\ell^{(k)} \right]. \end{aligned} \quad (\text{A.2.5})$$

Moreover,

$$\frac{d^k}{dx^k} (x^\ell) = \begin{cases} 0 & \text{if } \ell < k \\ \frac{\ell!}{(\ell-k)!} x^{\ell-k} & \text{if } \ell \geq k, \end{cases} \quad (\text{A.2.6})$$

and therefore $x^{r-\ell} \frac{d^k}{dx^k} (x^\ell)$ is either 0 for $\ell < k$, or $x^{r-k} \frac{\ell!}{(\ell-k)!}$ for $\ell \geq k$. Thus, using (A.2.1), (A.2.5) is expressed as

$$\sum_{i \in I^h} (x - x_i)^r \frac{d^k N_i^h}{dx^k}(x) = x^{r-k} \sum_{\ell=k}^r \binom{r}{\ell} \frac{(-1)^\ell \ell!}{(\ell-k)!} - \sum_{\ell=p+1}^r (-1)^\ell \binom{r}{\ell} x^{r-\ell} R_\ell^{(k)}. \quad (\text{A.2.7})$$

Note that the first sum of the r.h.s. term of (A.2.7) cancels because, for $r > k$,

$$\sum_{\ell=k}^r (-1)^\ell \binom{r}{\ell} \frac{\ell!}{(\ell-k)!} = (-1)^k \frac{r!}{(r-k)!} \left[\sum_{j=0}^{r-k} (-1)^j \binom{r-k}{j} \right] = 0, \quad (\text{A.2.8})$$

and consequently

$$\sum_{i \in I^h} (x - x_i)^r \frac{d^k N_i^h}{dx^k}(x) = \sum_{\ell=p+1}^r (-1)^{\ell+1} \binom{r}{\ell} x^{r-\ell} R_\ell^{(k)}. \quad (\text{A.2.9})$$

If $r \leq p$, obviously ℓ cannot range between $p + 1$ and r , thus,

$$\sum_{i \in I^h} (x - x_i)^r \frac{d^k N_i^h}{dx^k}(x) = 0, \quad r \leq p.$$

which does coincide with (A.2.3). For $r > p$, using (A.2.1), (A.2.9) becomes

$$\sum_{i \in I^h} (x - x_i)^r \frac{d^k N_i^h}{dx^k}(x) = \frac{L^k(x) r!}{(p+1-k)!} \sum_{\ell=p+1}^r \frac{(-1)^{\ell+1} x^{r-\ell} \xi^{\ell-(p+1)}}{(\ell-(p+1))! (r-\ell)!}. \quad (\text{A.2.10})$$

A new mute index $j := \ell - (p + 1)$ and a new parameter $s := r - (p + 1)$ are defined and thus, (A.2.10) can be rewritten as

$$\begin{aligned} \sum_{i \in I^h} (x - x_i)^r \frac{d^k N_i^h}{dx^k}(x) &= (-1)^p \frac{L^k(x) r!}{(p+1-k)! s!} \sum_{j=0}^s \binom{s}{j} x^{s-j} (-\xi)^j \\ &= (-1)^p \frac{L^k(x) r!}{(p+1-k)! s!} (x - \xi)^s. \end{aligned} \quad (\text{A.2.11})$$

Since $|L^k(x)| \leq h^{p+1-k}$, when $|x - \xi| \leq h$, (A.2.11) can be bounded, namely,

$$\left| \sum_{i \in I^h} (x - x_i)^r \frac{d^k N_i^h}{dx^k}(x) \right| \leq \frac{r!}{(p+1-k)! s!} h^{r-k}, \quad (\text{A.2.12})$$

which is precisely the inequality (A.2.4). \square

Remark A.2.1. The term that cancels according to (A.2.8), that is the first sum of the r.h.s. term of (A.2.7), is a rearranged expression of

$$\sum_{\ell=0}^r (-1)^\ell \binom{r}{\ell} x^{r-\ell} \frac{d^k}{dx^k} (x^\ell)$$

for $r > k$, see (A.2.5). However, for $k > r$, this term is obviously also zero because $d^k(x^\ell)/dx^k = 0$ for $\ell = 0, \dots, r$. This term is not zero for $k = r$. In this case, the cited term takes the value of $(-1)^r r!$. Nevertheless, Lemma A.2.1 is restricted to $r > k$ because it is the only case needed in the rest of the paper.

In order to prove the convergence results (error bound theorems) several lemmas and a theorem are needed. Their goal is to bound the shape function, N_j^p , and its derivatives. Hence, a bound on the r.h.s. of (4.2.8) and then a bound for α are needed.

Lemma A.2.2. Let $q_r(x) := x^r$. Then, for $k = 0, \dots, p$,

$$\frac{d^k}{dx^k} \left[q_r(0) - \sum_{i \in I^h} q_r \left(\frac{x - x_i}{\rho} \right) N_i^h(x) \right] = 0, \quad r = 0, \dots, p, \quad (\text{A.2.13})$$

and

$$\left| \frac{d^k}{dx^k} \left[q_r(0) - \sum_{i \in I^h} q_r \left(\frac{x - x_i}{\rho} \right) N_i^h(x) \right] \right| \leq \lambda_{k,r} \frac{h^{r-k}}{\rho^r}, \quad r \geq p+1, \quad (\text{A.2.14})$$

where $\lambda_{k,r}$ are the following constants independent of x , ρ and h :

$$\lambda_{k,r} := \frac{r!}{(r-k)!} \sum_{\ell = \max\{k-r+p+1, 0\}}^k \binom{k}{\ell} \binom{r-k}{p+1-\ell}. \quad (\text{A.2.15})$$

Proof. In order to simplify the notation

$$t_r(x) := q_r(0) - \sum_{i \in I^h} q_r \left(\frac{x - x_i}{\rho} \right) N_i^h(x) \quad (\text{A.2.16})$$

is defined. Three cases are considered: $r = 0$, $1 \leq r \leq p$ and $p < r$. In the first case, for $r = 0$, $q_0(x) = 1$ and $t_0(x) = 1 - \sum_{i \in I^h} N_i^h(x) = 1 - 1 = 0$. In the second case, for $r = 1, \dots, p$, Lemma A.2.1 gives, for $k = 0$,

$$t_r(x) = -\frac{1}{\rho^r} \left[\sum_{i \in I^h} (x - x_i)^r N_i^h(x) \right] = 0.$$

Hence, $d^k(t_r(x))/dx^k = 0$ for every k and, consequently, (A.2.13) is proved. For the last case, $r > p$,

$$\begin{aligned} \frac{d^k t_r}{dx^k}(x) &= -\frac{1}{\rho^r} \sum_{i \in I^h} \frac{d^k}{dx^k} \left[(x - x_i)^r N_i^h(x) \right] \\ &= -\frac{1}{\rho^r} \sum_{i \in I^h} \left\{ \sum_{\ell=0}^k \binom{k}{\ell} \frac{d^{k-\ell}}{dx^{k-\ell}} [(x - x_i)^r] \frac{d^\ell N_i^h}{dx^\ell}(x) \right\}. \end{aligned}$$

Using (A.2.6) and changing the order of the sums, the previous formula is expressed as

$$\frac{d^k t_r}{dx^k}(x) = -\frac{1}{\rho^r} \sum_{\ell=0}^k \binom{k}{\ell} \frac{r!}{(r-k+\ell)!} \left[\sum_{i \in I^h} (x - x_i)^{r-k+\ell} \frac{d^\ell N_i^h}{dx^\ell}(x) \right].$$

Note that $r - k + \ell > \ell$ because $r > p \geq k$. Then, Lemma A.2.1 applies and the sum with index i is zero if $\ell + r - k \leq p$. Therefore, the sum in ℓ begins with $\ell = \max\{k - r + (p + 1), 0\}$. Using now Lemma A.2.1 for the remaining terms, the bound (A.2.14) is proved:

$$\left| \frac{d^k t_r}{dx^k}(x) \right| \leq \frac{1}{\rho^r} \left[\sum_{\ell=\max\{k-r+p+1,0\}}^k \binom{k}{\ell} \frac{r!}{(r-k+\ell)!} \mu_{r-k+\ell,\ell} \right] h^{r-k}.$$

□

A.3 Convergence of FE enriched with EFG

Lemma A.3.1. *Let k be such that $0 \leq k \leq p$. Suppose $h \leq Q_k \rho$, where the following definition Q_k stands for given p and m :*

$$Q_k := \begin{cases} 1 & \text{for } m = p + 1, \\ \min_{r=p+2,\dots,m} \left(\frac{\lambda_{k,p+1}}{\lambda_{k,r}} \right)^{\frac{1}{r-(p+1)}} & \text{for } m > p + 1. \end{cases} \quad (\text{A.3.1})$$

and $\lambda_{k,r}$ are the constants defined in (A.2.15). Then, the derivatives of the r.h.s. of equation (4.2.8) verify the following inequality:

$$\left\| \frac{d^k}{dx^k} \left[\mathbf{P}(0) - \sum_{i \in I^h} \mathbf{P} \left(\frac{x - x_i}{\rho} \right) N_i^h(x) \right] \right\|_{\infty} \leq \lambda_{k,p+1} \frac{h^{p+1-k}}{\rho^{p+1}}. \quad (\text{A.3.2})$$

Proof. Since $h \leq Q_k \rho$, by definition (A.3.1), then for $r = p + 2, \dots, m$

$$\lambda_{k,r} \left[\frac{h}{\rho} \right]^{r-(p+1)} \leq \lambda_{k,p+1}.$$

Using now Lemma A.2.2 for every component, $t_r(x)$, of the r.h.s. in (4.2.8) one gets

$$\frac{d^k t_r}{dx^k} = 0 \quad \text{for } r = 0, \dots, p,$$

$$\frac{d^k t_r}{dx^k} = \lambda_{k,p+1} \frac{h^{p+1-k}}{\rho^{p+1}} \quad \text{for } r = p + 1,$$

and

$$\left| \frac{d^k t_r}{dx^k}(x) \right| \leq \lambda_{k,r} \left[\frac{h}{\rho} \right]^{r-(p+1)} \frac{h^{p+1-k}}{\rho^{p+1}} \leq \lambda_{k,p+1} \frac{h^{p+1-k}}{\rho^{p+1}} \quad \text{for } r = p + 2, \dots, m.$$

□

Lemma A.3.2. *Let k be such that $0 \leq k \leq p$. Suppose $h/\rho \leq \min_{0 \leq s \leq k} Q_s$, where Q_s is the constant defined in (A.3.1). Then, it exists a constant C_k^* , independent of ρ , h and x , such that the solution, α , of the linear system of equations (4.2.8) verifies*

$$\left\| \frac{d^k \alpha}{dx^k} \right\|_{\infty} \leq C_k^* \frac{h^{p+1-k}}{\rho^{p+1}}. \quad (\text{A.3.3})$$

Proof. The r.h.s. of (4.2.8) is defined as $\mathbf{T} = \mathbf{T}(x) := \mathbf{P}(0) - \sum_{i \in I^h} \mathbf{P}\left(\frac{x-x_i}{\rho}\right) N_i^h(x)$.

Thus, equation (4.2.8) is rewritten as

$$\mathbf{M}\alpha = \mathbf{T}. \quad (\text{A.3.4})$$

Using Lemma A.3.1 and Corollary A.1.3, the previous equation implies:

$$\|\alpha\|_{\infty} \leq \|\mathbf{M}^{-1}\|_{\infty} \|\mathbf{T}\|_{\infty} \leq \underbrace{C^{\mathbf{M}} \lambda_{0,p+1}}_{C_0^*} \frac{h^{p+1}}{\rho^{p+1}}.$$

Once (A.3.3) is proved for $k = 0$, we proceed by induction on k , that is, assume

$$\left\| \frac{d^s \alpha}{dx^s} \right\|_{\infty} \leq C_s^* \frac{h^{p+1-s}}{\rho^{p+1}} \quad \text{for } s = 0, \dots, k-1. \quad (\text{A.3.5})$$

Differentiating (A.3.4) yields

$$\left[\sum_{s=0}^{k-1} \binom{k}{s} \frac{d^{k-s} \mathbf{M}}{dx^{k-s}} \frac{d^s \alpha}{dx^s} \right] + \mathbf{M} \frac{d^k \alpha}{dx^k} = \frac{d^k \mathbf{T}}{dx^k}.$$

Rearranging terms, the following expression for the k -th derivative of α is found:

$$\frac{d^k \alpha}{dx^k} = \mathbf{M}^{-1} \left[\frac{d^k \mathbf{T}}{dx^k} - \sum_{s=0}^{k-1} \binom{k}{s} \frac{d^{k-s} \mathbf{M}}{dx^{k-s}} \frac{d^s \alpha}{dx^s} \right].$$

Since $\rho/h \leq Q_k$, using Lemma A.3.1, Corollary A.1.3 and the induction hypothesis (A.3.5), the following inequality is obtained:

$$\begin{aligned} \left\| \frac{d^k \alpha}{dx^k} \right\|_{\infty} &\leq \|\mathbf{M}^{-1}\|_{\infty} \left[\left\| \frac{d^k \mathbf{T}}{dx^k} \right\|_{\infty} + \sum_{s=0}^{k-1} \binom{k}{s} \left\| \frac{d^{k-s} \mathbf{M}}{dx^{k-s}} \right\|_{\infty} \left\| \frac{d^s \alpha}{dx^s} \right\|_{\infty} \right] \\ &\leq C^{\mathbf{M}} \left[\lambda_{k,p+1} \frac{h^{p+1-k}}{\rho^{p+1}} + \sum_{s=0}^{k-1} \binom{k}{s} C_{k-s}^{\mathbf{M}} \rho^{s-k} C_s^* \frac{h^{p+1-s}}{\rho^{p+1}} \right] \\ &\leq \widehat{C} \frac{h^{p+1-k}}{\rho^{p+1}} + \sum_{s=0}^{k-1} \widehat{C}_s \frac{h^{p+1-s}}{\rho^{p+1+k-s}}. \end{aligned}$$

When $k > 0$, assuming $h/\rho \leq Q_s$ for $s = 0, \dots, k-1$, it follows that

$$\frac{h^{p+1-s}}{\rho^{p+1+k-s}} \leq (Q_s)^{k-s} \frac{h^{p+1-k}}{\rho^{p+1}}. \quad (\text{A.3.6})$$

Consequently,

$$\left\| \frac{d^k \boldsymbol{\alpha}}{dx^k} \right\|_{\infty} \leq C_k^* \frac{h^{p+1-k}}{\rho^{p+1}}.$$

□

Theorem A.3.3 (Shape function's bound). *Let m be the order of consistency of the mixed approximation $u^h + u^\rho$, such that $m = p + q$, where p is the order of the finite element approximation, u^h , and $q > 0$ is the order increment due to u^ρ . Let ℓ such that $0 \leq \ell \leq p$. Assume the following regularity conditions for the exact solution, u , and the weighting function, ϕ : $u \in C^{m+1}(\bar{\Omega})$ and $\phi \in C^\ell(\bar{\Omega})$, where Ω is bounded and $\partial\Omega$ is smooth. Finally, assume that $h/\rho \leq \min_{0 \leq k \leq \ell} Q_k$ where Q_k is the constant defined in (A.3.1). Then, for $k = 0, \dots, \ell$, the following inequality holds:*

$$\left\| \frac{d^k N_j^\rho}{dx^k} \right\|_{L^\infty} \leq C_k^{**} \frac{h^{p+1-k}}{\rho^{p+1}},$$

where C_k^{**} is a constant independent of x , ρ and h .

Proof. Using the Newton's binomial expression in (4.2.5), the k -th derivative of the shape function N_j^ρ is

$$\frac{d^k N_j^\rho}{dx^k}(x) = \sum_{s=0}^k \binom{k}{s} \left[\frac{d^s \boldsymbol{\alpha}}{dx^s}(x) \right]^T \frac{1}{\rho^{k-s}} \frac{d^{k-s} [\mathbf{P}(z)\phi(z)]}{dz^{k-s}} \Big|_{z=(x-x_i)/\rho}, \quad (\text{A.3.7})$$

Note that $\phi(z) = 0$ if $|z| > 1$. Therefore, by Lemma A.3.2,

$$\left| \frac{d^k N_j^\rho}{dx^k}(x) \right| \leq \sum_{s=0}^k \binom{k}{s} C_s^* \frac{h^{p+1-s}}{\rho^{p+1+k-s}} \left\{ \max_{|z| \leq 1} \left\| \frac{d^{k-s} [\mathbf{P}(z)\phi(z)]}{dz^{k-s}} \right\|_{\infty} \right\}$$

Note that the term in braces is a constant independent of h and ρ . Moreover, with the assumption $h/\rho \leq \min_{0 \leq k \leq \ell} Q_k$, see equation (A.3.6), it follows that

$$\left| \frac{d^k N_j^\rho}{dx^k}(x) \right| \leq \underbrace{\left[\sum_{s=0}^k \binom{k}{s} C_s^* (Q_s)^{k-s} \left\{ \max_{|z| \leq 1} \left\| \frac{d^{k-s} [\mathbf{P}(z)\phi(z)]}{dz^{k-s}} \right\|_{\infty} \right\} \right]}_{C_k^{**}} \frac{h^{p+1-k}}{\rho^{p+1}}.$$

□

Theorem A.3.4 (Error bound). *Under the same assumptions of Theorem A.3.3,*

$$|u - (u^h + u^\rho)|_{\mathcal{W}_\infty^k} \leq h^{p+1-k} [C_1 h^q + C_2 \rho^q] |u|_{\mathcal{W}_\infty^{m+1}} \quad k = 0, \dots, \ell. \quad (\text{A.3.8})$$

where C_1 and C_2 are independent of the finite element size, h , and the dilation parameter, ρ , of the mesh-free approximation.

Proof. Let x be a point in Ω and let x_i be either a node of the finite element where x is located, i.e. $|x - x_i| < h$, or a particle such that $N_i^\rho(x) \neq 0$, i.e. $|x - x_i| < \rho$. Consider the m -order Taylor expansion of u around x

$$\begin{aligned} u(x_i) = & u(x) + (x_i - x) \frac{du}{dx}(x) + \frac{(x_i - x)^2}{2} \frac{d^2u}{dx^2}(x) + \dots \\ & + \frac{(x_i - x)^m}{m!} \frac{d^m u}{dx^m}(x) + \frac{(x_i - x)^{m+1}}{(m+1)!} \frac{d^{m+1}u}{dx^{m+1}}(\xi), \end{aligned} \quad (\text{A.3.9})$$

where $\xi = \theta x + (1 - \theta)x_i$, for some θ such that $0 \leq \theta \leq 1$. The point ξ lies in Ω if the finite elements are convex and ρ is small enough near the smooth boundary. Let us define

$$N_i(x) := \begin{cases} N_i^h(x) & i \in I^h, \\ N_i^\rho(x) & i \in I^\rho. \end{cases}$$

The derivative of the approximation of u yields

$$\frac{d^k u}{dx^k}(x) \simeq \frac{d^k (u^h + u^\rho)}{dx^k}(x) = \sum_{i \in I^h \cup I^\rho} u(x_i) \frac{d^k N_i}{dx^k}(x). \quad (\text{A.3.10})$$

The shape functions N_j^ρ are derived in order to achieve m -order consistency. Thus, the complete set of functions N_i (including the finite element basis) has m -order consistency. Then, replacing (A.3.9) in (A.3.10), and applying Lemma A.1.1, a new expression is obtained:

$$\begin{aligned} \frac{d^k (u^h + u^\rho)}{dx^k}(x) = & u(x) \underbrace{\sum_{i \in I^h \cup I^\rho} \frac{d^k N_i}{dx^k}(x)}_0 + \frac{du}{dx}(x) \underbrace{\sum_{i \in I^h \cup I^\rho} (x_i - x) \frac{d^k N_i}{dx^k}(x)}_0 + \dots \\ & + \frac{1}{k!} \frac{d^k u}{dx^k}(x) \underbrace{\sum_{i \in I^h \cup I^\rho} (x_i - x)^k \frac{d^k N_i}{dx^k}(x)}_{k!} + \dots \\ & + \frac{1}{m!} \frac{d^m u}{dx^m}(x) \underbrace{\sum_{i \in I^h \cup I^\rho} (x_i - x)^m \frac{d^k N_i}{dx^k}(x)}_0 \\ & + \frac{1}{(m+1)!} \frac{d^{m+1} u}{dx^{m+1}}(\xi) \sum_{i \in I^h \cup I^\rho} (x_i - x)^{m+1} \frac{d^k N_i}{dx^k}(x). \end{aligned}$$

The previous expression can be rewritten as:

$$\begin{aligned} \frac{d^k [u - (u^h + u^\rho)]}{dx^k}(x) &= \frac{-1}{(m+1)!} \frac{d^{m+1}u}{dx^{m+1}}(\xi) \left[\sum_{i \in I^h} (x_i - x)^{m+1} \frac{d^k N_i^h}{dx^k}(x) \right. \\ &\quad \left. + \sum_{j \in I^\rho} (x_j - x)^{m+1} \frac{d^k N_j^\rho}{dx^k}(x) \right]. \end{aligned} \quad (\text{A.3.11})$$

For a given x the first sum in the r.h.s. of (A.3.11) may be restricted to the $p+1$ nodes of the finite element where x is located and which verify $|x - x_i| \leq h$. Similarly, the second sum in the r.h.s. of (A.3.11) is circumscribed to the particles x_j such that x is included in the support of $N_j^\rho(x)$, i.e. particles such that $|x - x_j| \leq \rho$. Let us denote by n the maximum number of particles verifying $|x - x_j| \leq \rho$. Hence, from (A.3.11) the following bound is obtained

$$\begin{aligned} \left| \frac{d^k (u^\rho + u^h)}{dx^k}(x) \right| &\leq \frac{1}{(m+1)!} \left| \frac{d^{m+1}u}{dx^{m+1}}(\xi) \right| \left[(p+1)h^{m+1} \max_{i \in I^h} \left| \frac{d^k N_i^h}{dx^k} \right| \right. \\ &\quad \left. + n\rho^{m+1} \max_{j \in I^\rho} \left| \frac{d^k N_j^\rho}{dx^k} \right| \right]. \end{aligned}$$

On one hand, the k -th derivative ($k < p$) of the finite element shape functions is $\mathcal{O}(h^{-k})$. On the other, Theorem A.3.3 bounds the shape functions N_j^ρ and their derivatives. Consequently,

$$\begin{aligned} \left\| \frac{d^k u}{dx^k} - \frac{d^k (u^\rho + u^h)}{dx^k} \right\|_{\mathcal{L}_\infty} &\leq \left[C_1 h^{m+1-k} + C_2 \frac{h^{p+1-k}}{\rho^{p+1}} \rho^{m+1} \right] \left\| \frac{d^k u^{m+1}}{dx^k} \right\|_{\mathcal{L}_\infty} \\ &\leq h^{p+1-k} [C_1 h^q + C_2 \rho^q] \left\| \frac{d^k u^{m+1}}{dx^k} \right\|_{\mathcal{L}_\infty}, \end{aligned}$$

which is precisely (A.3.8). \square

Corollary A.3.5. *Let m be the order of consistency of the mixed approximation $u^h + u^\rho$, such that $m = p + q$, where p is the order of the finite element approximation, u^h , and $q > 0$ is the order increment due to u^ρ . Suppose that the following regularity conditions hold for the exact solution, u , and the weighting function, ϕ : $u \in C^{m+1}(\bar{\Omega})$ and $\phi \in C^0(\bar{\Omega})$, where Ω is bounded and $\partial\Omega$ is smooth. Finally, assume that the element size h is small enough with respect to the dilation parameter ρ , i.e.*

$$\frac{h}{\rho} \leq \min_{r=p+1, \dots, m} \binom{r}{p+1}^{\frac{-1}{r-(p+1)}}.$$

Then,

$$\|u - (u^h + u^\rho)\|_{\mathcal{L}_\infty} \leq h^{p+1} [C_1 h^q + C_2 \rho^q] |u|_{\mathcal{W}_\infty^{m+1}} \quad (\text{A.3.12})$$

where C_1 and C_2 are independent of the finite element size, h , and the dilation parameter, ρ , of the mesh-free approximation.

Remark A.3.1. The error bound given in (A.3.12) allows to predict the convergence behaviour of the mixed finite element-particle interpolation. That is, when both h and ρ decrease simultaneously, the order of convergence is $p + q + 1 = m + 1$. When h goes to zero while ρ is kept constant, the order is either $p + 1$ if $C_1 h^q < C_2 \rho^q$ or $m + 1$ when $C_1 h^q \gg C_2 \rho^q$. And finally, convergence is ensured at a rate of q when ρ goes to zero provided that $C_1 h^q \ll C_2 \rho^q$. But, if h is kept constant as ρ goes to zero, it is necessary to increase the order of consistency in order to achieve asymptotic convergence. Numerical examples of these situations are shown in (Huerta and Fernández-Méndez 2000).

If the restriction on the mesh size, $h/\rho \leq \min_{0 \leq k \leq \ell} Q_k$, is omitted, Lemma A.3.1 must be rewritten, the previous results are no longer valid and must be replaced by less sharp error bounds.

Lemma A.3.6. *With no restriction on the element size, the independent term in equation (4.2.8) verifies*

$$\left\| \frac{d^k}{dx^k} \left[\mathbf{P}(0) - \sum_{i \in I^h} \mathbf{P}\left(\frac{x - x_i}{\rho}\right) N_i^h(x) \right] \right\|_{\infty} \leq \lambda_{k,p+1} \frac{h^{p+1-k}}{\rho^m}, \quad k = 0, \dots, p.$$

Proof. Trivial from Lemma A.2.2. □

Reproducing the proof of the previous lemmas, the following less accurate error bound is easily proved:

Theorem A.3.7 (Error bound). *Under the same assumptions of Theorem A.3.4 but with no restriction on the element size, the error bound is*

$$|u - (u^h + u^\rho)|_{\mathcal{W}_\infty^k} \leq h^{p+1-k} [C_1 h^q + C_2 \rho^1] |u|_{\mathcal{W}_\infty^{m+1}},$$

where C_1 and C_2 are independent of the finite element size, h , and the dilation parameter, ρ , of the mesh-free approximation.

Corollary A.3.8. *Under the same assumptions of Corollary A.3.5 but with no restriction on the element size, the following inequality holds:*

$$\|u - (u^h + u^\rho)\|_{\mathcal{L}_\infty} \leq h^{p+1} [C_1 h^q + C_2 \rho^1] |u|_{\mathcal{W}_\infty^{m+1}},$$

where C_1 and C_2 are independent of the finite element size, h , and the dilation parameter, ρ , of the mesh-free approximation.

A.4 Concluding remarks

In this appendix the enrichment of finite elements with particles is analysed. From the expression of the obtained error bounds it is deduced that, in order to ensure asymptotic convergence, the enrichment of the finite element solution must be done either (1) increasing at the same time the number of particles and the order of consistency, or (2) keeping constant the ratio $\frac{h}{\rho}$, and thus increasing simultaneously the number of particles and the number of nodes. However, if h and m are kept constant no convergence is achieved although ρ goes to zero. In any case, there is an important improvement of the solution when particles are added to a finite element mesh.

Appendix B

Numerical simulation of active carbon canisters

Active carbon canisters are used in the automotive industry to control the pollutant emission. The canister is located between the fuel tank and the atmosphere, see figures B.1 and B.2. It is a receptacle containing active carbon, a material specially designed in order to capture and store hydrocarbon (HC) particles (adsorption), see figure B.3. During periods with high temperatures, in the loading process, the fuel in the tank evaporates leaving contaminant HC. The goal is to avoid that the HC goes freely into the atmosphere. When the vehicle starts, in the purge process, the combustion air goes into the motor through the canister, cleaning the active carbon (desorption). The HC particles from the active carbon are added to the fuel coming from the fuel tank in the combustion.

Industrial canister design is a lengthy task, involving the testing of prototypes, due to various factors:

- (1) the canisters typically have a rather complex 3D geometry, because they must occupy the space left after other components have already been placed during the design process (see figure B.3)
- (2) they are subject to very strict emission regulations in the American and European markets regarding several design parameters (working capacity, purge, refuelling, etc.)
- (3) different materials (active carbon of various types, air chambers, foams, etc.) are required to meet these regulations.

The ultimate goal is the (at least partial) replacement of prototype testing by finite element simulations, thus shortening the design cycle, see for instance (Hossain and Yonge 1992) and (Huerta, Rodríguez-Ferran, Sarrate, Díez and Fernández-Méndez 2001). The goal is

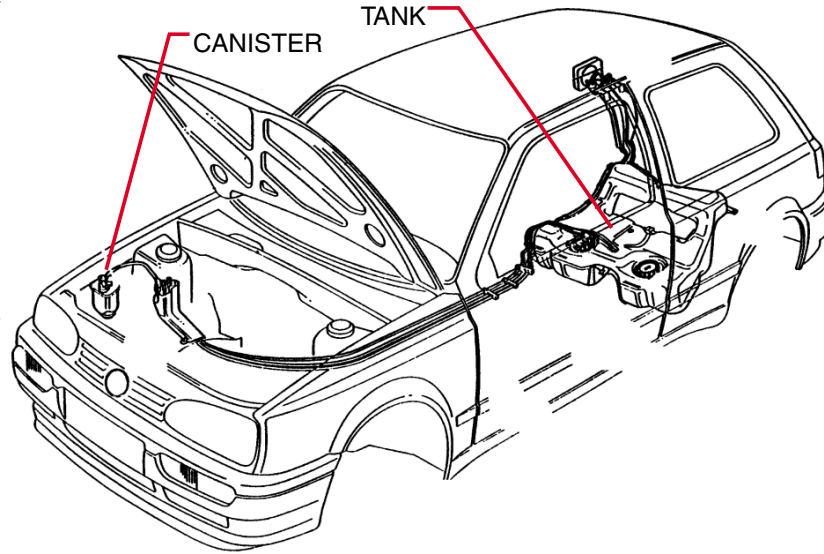


Figure B.1: Canister location

to model, for instance, the complete evolution of a clean canister up to breakthrough (the canister is full enough so that some HC goes out to the atmosphere).

The dominant physical phenomenon in a canister is the transport of HC. In (Huerta, Rodríguez-Ferran, Sarrate, Díez and Fernández-Méndez 2001) transport is modelled by means of a convection-diffusion-reaction equation:

$$u_t + \mathbf{v} \cdot \nabla u - \nu \Delta u + \sigma(u)u = f(u)$$

where u is the concentration of HC in air, \mathbf{v} is the air velocity field inside the canister, which is previously computed solving a potential flow problem, and ν is the diffusion coefficient. The reaction term $\sigma(u)u$ and the source term $f(u)$, which are highly nonlinear, model the adsorption (under loading conditions) or desorption (during the purge) of HC. This adsorption/desorption process involves complex mass transfer processes on the surface and in the pores of the active carbon particles. The mass transfer process depends on the HC concentration in air, u , and on the HC in carbon, usually modelled by extra variables.

However, during the loading process, the air convection velocity \mathbf{v} is usually small enough so that the mass transfer process between air and active carbon can be considered instantaneous. That is, the convected "dirty" air ($u > 0$) transfers all the HC mass to the active carbon, and becomes "clean" air ($u = 0$) almost instantaneously, and until the active carbon becomes saturated. Thus, the HC front becomes sharp and advances with slower velocity in the carbon regions, due to this fast mass transfer phenomena. Under

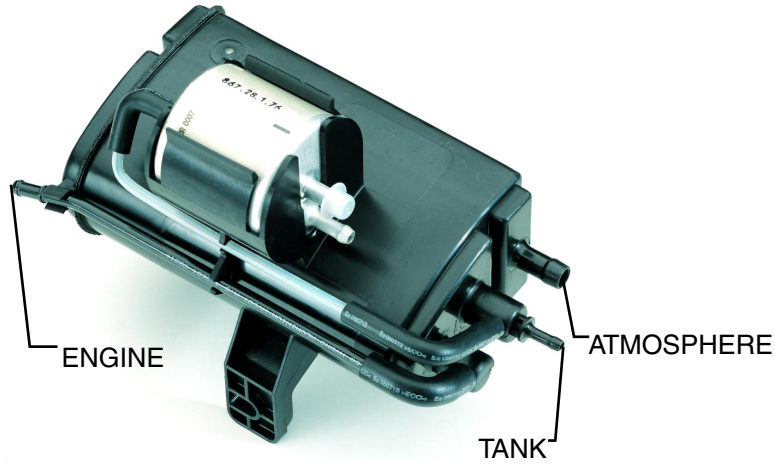


Figure B.2: Canister

this conditions, the problem can be modelled by a simple transient convection-diffusion equation in the whole domain,

$$u_t + \tilde{\mathbf{v}} \cdot \nabla u - \nu \Delta u = 0$$

where $\tilde{\mathbf{v}}$ represents the HC front velocity, which is computed from the air velocity \mathbf{v} just multiplying with a factor α :

$$\tilde{\mathbf{v}} = \alpha \mathbf{v}.$$

The factor α depends on the material properties. For example, is is equal to 1 at the air cambers or foams, where there is not adsorption process and the HC is convected with the air velocity, and more or less 10^{-2} at the active carbon regions, where the front of HC becomes slower than the air velocity due to the carbon adsorption effect. Under this conditions, the problem can be modelled by a simple linear transient convection-diffusion equation. All the examples in this appendix have been computed with this simplified model. However, most of the problems in the numerical resolution of the more general nonlinear case are also present in the simplified problem.

Various numerical challenges can be identified. Due to the complex 3D geometry of most canisters, the flow is highly non-uniform. In fact, recent canister designs typically incorporate air chambers to smooth air flow. The transport problem is convection-dominated and inherently transient. In the nonlinear case the problem involves multi-physics at two very different length scales (the small or local scale of the active carbon pellets (mm) and



Figure B.3: Active carbon and several canisters

the large or global scale of the canister (dm)). This problem is avoided in the simplified loading problem. However, high variations in the front convection velocity field are present in both cases, due to the treatment of different materials: the front velocity is more or less 100 times greater in the air chambers than in the carbon regions.

To tackle these difficulties, a proper combination of sophisticated numerical algorithms is required:

- ▷ Unstructured 3D finite element meshes are employed.
- ▷ High-order time-stepping schemes in combination with a least-squares stabilized formulation are considered in order to obtain an accurate solution and avoid oscillations, see chapter 5 for details.
- ▷ A least-squares stabilization technique has been chosen in order to obtain symmetric linear systems of equations. This enables the efficient resolution of large and sparse systems of equations arising in 3D computations, with a preconditioned conjugated gradient solver and compact row storage.
- ▷ Shock-capturing techniques, see (Tezduyar and Park 1986) or (Codina 1993), are also needed in some cases due to the presence of sharp fronts in the HC concentration.
- ▷ In the nonlinear case, the non-linearity of the reaction term is fully accounted for at the local (i.e. active carbon particle) level, so the global problem is linear.

Some numerical results are shown in section B.1. All this work has been developed in a contract between the LaCàN group (Laboratory de Càlcul Numèric at the Universitat Politècnica de Catalunya) and Expert Components S.A., a leading European canister manufacturer. Although they are not included in this appendix, nonlinear and unloading simulations have also been done. However, there are many topics that still need further research.

B.1 Numerical examples

The objective of this section is to illustrate some topics of interest in the design of active carbon canisters.

The following 2D example shows the influence of the air chambers in the canister behaviour and its importance in order to obtain an optimal design. The inclusion of air chambers in the canister design presents two possible advantages:

- (i) as noted in the introduction, recent canister designs typically incorporate air chambers to smooth air flow,
- (ii) the active carbon mass needed in the canister production is smaller due to the air chambers, and thus, the canister cost becomes cheaper.

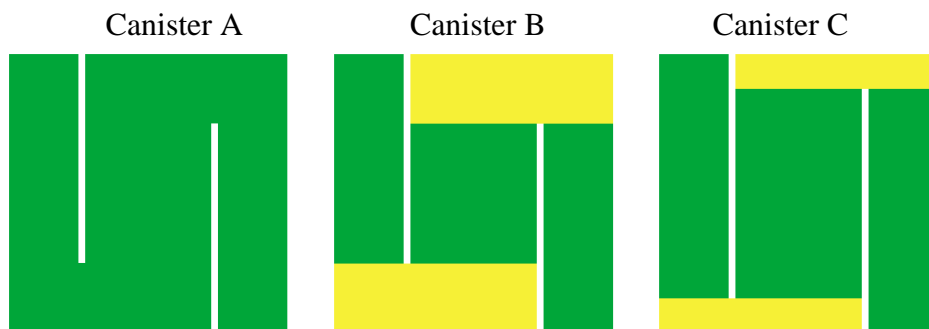


Figure B.4: Three 2D canister models with active carbon (in green) and air chambers (in yellow)

Figure B.4 shows three 2D simplified models for an active carbon canister. Recall that usually the external geometry of the canister is fixed, since it must occupy the space left after other components have already been placed during the design process. Canister A corresponds to a classical canister, it is totally filled with active carbon. Canisters B and

C incorporates two air chambers (in yellow). However, the air chamber in canister C is smaller than in canister B in order to compare the effect. The objective of this experiment is to corroborate (ii) and to investigate about the possible influence of the shape of the air chambers.

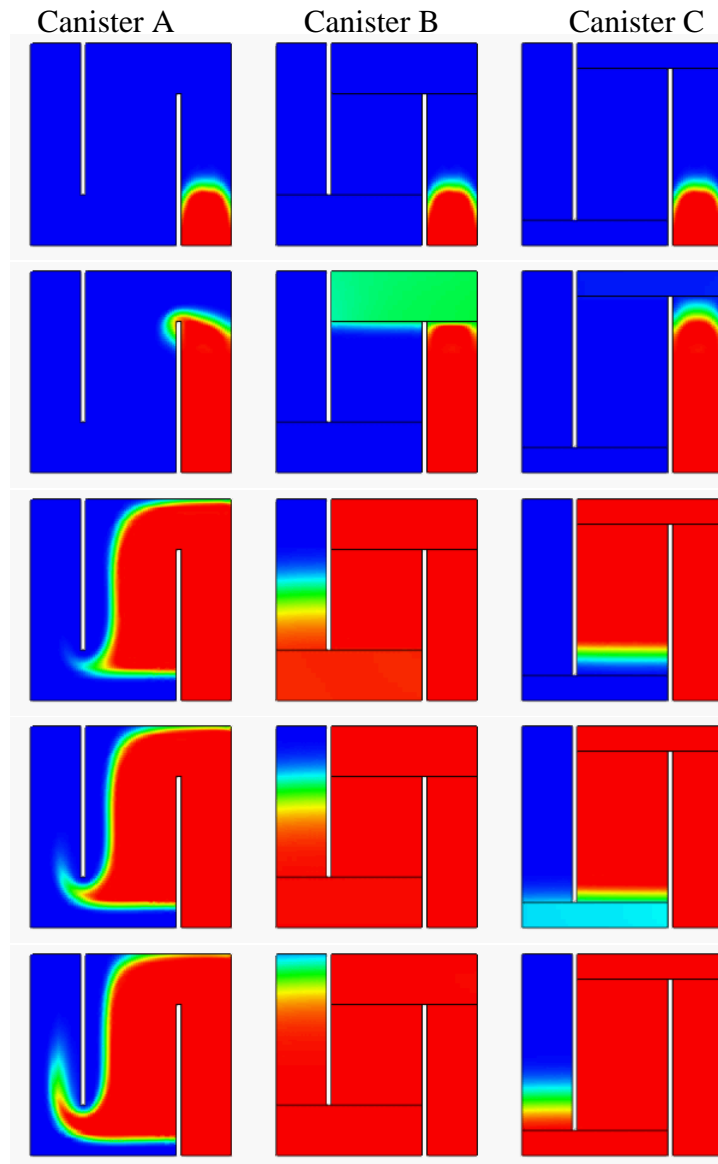


Figure B.5: Evolution of the concentration at five different time steps for the three canisters described in figure B.4

The solution at different time steps is shown in figure B.5. As is was expected the flow becomes smoother in the active carbon regions and the HC front advances almost orthogonal

to the faces of canisters B and C, due to the presence of air chambers. However, canister C corresponds to the most attractive design, since its breakthrough will happen later than in the other prototypes. Moreover, when comparing canister C with canister A, the quantity of active carbon needed in the production of canister C is much smaller than in canister A, with the corresponding savings in the canister cost. So, the conclusion is that, a good design of the interior of the canister, including the design of the air chambers, can provide efficient and cheaper canisters.

Figure B.6 shows a 3D simulation of a more realistic canister. Interior chambers with air, foam, fleece and different types of active carbon are included in the model. Although, there are many topics that still require further research, numerical methods can be a powerful tool in canister design.

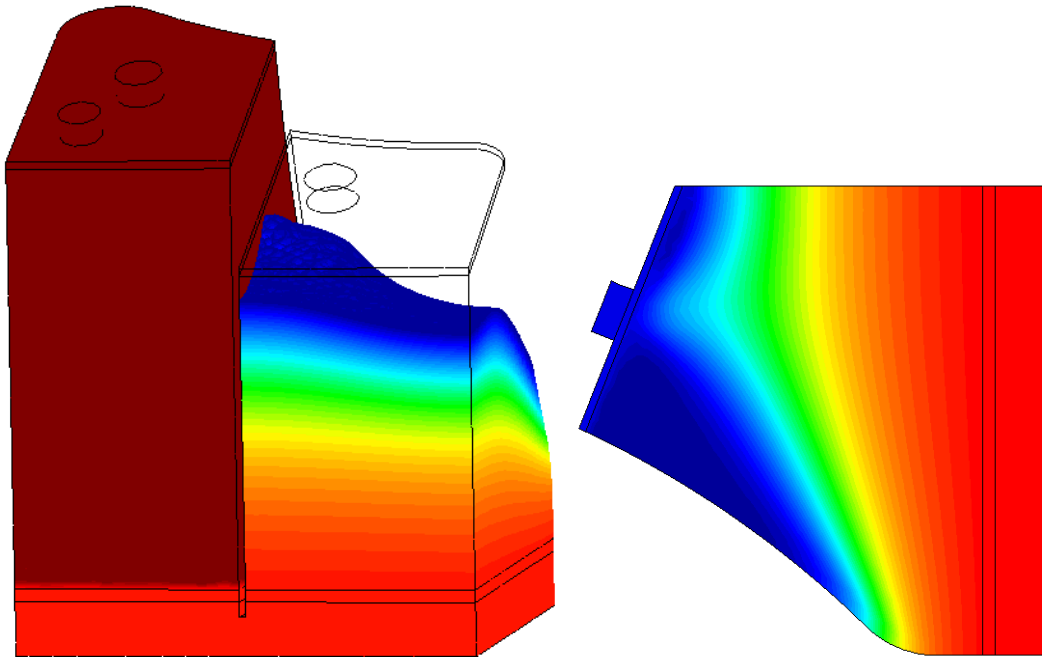


Figure B.6: Concentration in a 3D canister and orthogonal cut.

B.2 Conclusions and remarks

As it has been shown in the examples, numerical methods can be a powerful tool in the design of smart canisters, including for instance the design of air chambers. However, there are still many problems to overcome in order to attain an efficient numerical simulation of active carbon canisters. Active carbon canisters are subject to very strict emission regu-

lations in the American and European markets. It is necessary to obtain a very accurate solution in order to determine if one canister verifies or not one test. For instance, it is important to determine the quantity of HC that goes out from the canister with a very high precision, and thus, the shape and the position of the advancing front must be interpolated in a very accurate way.

These are some concrete topics to work in:

- ▷ About the spatial discretization, most of the realistic examples need 3D computations, and thus, the use of a dense enough mesh in the whole domain usually leads to a too large computational cost. In fact, the situation becomes terrible for the nonlinear model, which must be used at least in the unloading process. If only finite elements are used, the mesh should be adapted in order to capture the advancing front. This implies a degradation in the solution (due to successive projections of the solution between meshes) and an increase in the computational cost. In fact, in 3D it is not so easy to find a good mesh generator, which adapts the mesh to the prescribed densities of nodes. So, the mixed interpolation that combines finite elements and mesh-free methods presented in chapter 4 can be a good choice: a fixed coarse finite element mesh can be used in the whole domain, with a cloud of moving particles following the moving front in order to increase the spatial accuracy where it is needed.
- ▷ On the other hand, it is also necessary to discretize the problem with enough accuracy in time. So, high order time stepping schemes must be considered. Chapter 5 shows the capabilities of mesh-free methods in combination with high-order time stepping schemes and stabilization techniques. So, the use of mixed interpolations combining finite elements and mesh-free methods turns out to be hopeful in the numerical simulation of active carbon canisters.
- ▷ In the nonlinear case the problem involves multi-physics with two different time scales: local problem associated to the active carbon pellets usually requires a time step much smaller than the global problem. In order to maintain a not too small time step in the global problem, with the corresponding saving in the computational cost, sub-stepping techniques can be considered to solve the local problem in a enough accurate way.
- ▷ Although some problems are avoided in the simplified loading problem, high variations in the front convection velocity field are present in both cases due to the treatment of different materials: the front velocity is more or less 100 times greater in

the air chambers than in the carbon regions. So, it can be attractive to use multi-time-stepping algorithms, see (Belytschko and Mullen 1977) and (Gravouil and Combescure 2001), in order to adapt the time step to each region and calculate with a proper and almost uniform Courant number.

However, it is important to note that qualitative results can be easily obtained and, although this results can be useless in the verification of particular tests, they are useful to improve the canister design.

Bibliography

- Armero, F. (1999), On the locking of standard finite elements. Classroom notes.
- Askes, H., de Borst, R. and Heeres, O. (1999), ‘Conditions for locking-free elasto-plastic analyses in the element-free galerkin method’, *Computer Methods in Applied Mechanics and Engineering* **173**, 99–109.
- Babuška, I. and Melenk, J. (1995), The partition of the unity finite element method, Technical Report BN-1185, Institute for Physical Science and Technology, University of Maryland, Maryland.
- Baines, M. J. (1994), *Moving Finite Elements*, Monographs on Numerical Analysis, K.W. Morton, B. Parlet and J. Walsh Eds. Oxford Science Publications.
- Belytschko, T., Krongauz, Y., Fleming, M., Organ, D., and Liu, W. K. (1996), ‘Smoothing and accelerated computations in the element free galerkin method’, *Journal of Computational and Applied Mathematics* **74**, 111–126.
- Belytschko, T., Krongauz, Y., Organ, D., Fleming, M. and Krysl, P. (1996), ‘Meshless methods: an overview and recent developments’, *Computer Methods in Applied Mechanics and Engineering* **139**, 3–47.
- Belytschko, T., Lu, Y. Y. and Gu, L. (1994), ‘Element-free galerkin methods’, *International Journal for Numerical Methods in Engineering* **37**, 229–256.
- Belytschko, T. and Mullen, R. (1977), ‘Explicit integration of structural problems’, *Finite Elements in Nonlinear Mechanics* **2**, 697–720.
- Belytschko, T. and Organ, D. (1997), Element-free Galerkin methods for dynamic fracture in concrete, in ‘Comp. Plasticity. Fundamentals and Applications. D.R.J. Owen, E. Oñate and E. Hilton (Eds.)’, Barcelona, Spain, pp. 304–321.
- Belytschko, T., Organ, D. and Krongauz, Y. (1995), ‘A coupled finite element-free galerkin method’, *Computational Mechanics* **17**, 186–195.
- Belytschko, T. and Tabbara, M. (1996), ‘Dynamic fracture using element-free galerkin methods’, *International Journal for Numerical Methods in Engineering* **39**, 923–938.

- Bonet, J. and Kulasegaram, S. (2000), 'Correction and stabilization of smooth particle hydrodynamics methods with applications in metal forming simulations', *ijmme* **47**, 1189–1214.
- Bonet, J. and Lok, T. (1999), 'Variational and momentum preservation aspects of smooth particle hydrodynamic formulations', *cmame* **180**, 97–115.
- Bouillard, P. and Suleau, S. (1998), 'Element-free galerkin method for helmholtz problems: formulation and numerical assessment of the pollution effect', *Computer Methods in Applied Mechanics and Engineering* **162**, 317–335.
- Breitkopf, P., Rassineux, A. and Villon, P. (2001), Mesh-free operators for consistent field transfer in large deformation plasticity, in 'Book of abstracts of the 2nd European Conference on Computational Mechanics: Solids, Structures and Coupled Problems in Engineering', Cracow, Poland.
- Brooks, A. N. and Hugues, T. (1982), 'Streamline upwind/petrov-galerkin formulations for convection dominated flows with particular emphasis on the incompressible navier-stokes equations', *Computer Methods in Applied Mechanics and Engineering* **32**, 259.
- Carey, G., Pehlivanov, A., Shen, Y., Bose, A. and Wang, K. (1998), 'Least-squares finite elements for fluid flow and transport', *International Journal for Numerical Methods in Fluids* **27**, 97–107.
- Chen, J. S., Pan, C., Wu, C. T. and Liu, W. K. (1996), 'Reproducing kernel particle methods for large deformation analysis of non-linear', *Computer Methods in Applied Mechanics and Engineering* **139**, 195–227.
- Chen, J., Yoon, S., Wang, H. and Liu, W. K. (2000), 'An improved reproducing kernel particle method for nearly incompressible finite elasticity', *Computer Methods in Applied Mechanics and Engineering* **181**, 117–145.
- Chu, Y. A. and Moran, B. (1995), 'A computational model for nucleation of solid-solid phase transformations', *Modelling Simul. Mater. Sci. Eng.* **3**, 455–471.
- Codina, R. (1993), 'A discontinuity-capturing crosswind-dissipation for the finite element solution of the convection-diffusion equation', *Computer Methods in Applied Mechanics and Engineering* **110**, 325–342.
- Codina, R. (2000), 'On stabilized finite elements methods for linear systems of convection-diffusion-reaction equations', *Computer Methods in Applied Mechanics and Engineering* **188**, 61–82.
- Díez, P., Arroyo, M. and Huerta, A. (2000), 'Adaptivity based on error estimation for viscoplastic softening materials', *Mechanics of Cohesive-Frictional Materials* **5**, 87–112.
- Dolbow, J. and Belytschko, T. (1999), 'Volumetric locking in the element free galerkin method', *International Journal for Numerical Methods in Engineering* **46**, 925–942.

- Donéa, J., Quartapelle, L. and Selmin, V. (1987), 'An analysis of time discretization in the finite element solution of hyperbolic problems', *Journal of Computational Physics* **70**, 463–499.
- Donéa, J., Roig, B. and Huerta, A. (2000), 'High-order accurate time-stepping schemes for convection-diffusion problems', *Computer Methods in Applied Mechanics and Engineering* **182**, 249–275.
- Donéa, J., Roig, B. and Huerta, A. (n.d.), 'Time accurate solution of convective transport problems', *International Journal for Numerical Methods in Engineering* . submitted.
- Duarte, C. A. and Oden, J. T. (1996), 'H-p clouds - an h-p meshless method', *Numerical Methods for Partial Differential Equations* **12**, 1–34.
- Dyka, C. T. (1994), Addressing tension instability in sph methods, Technical Report NRL/MR/6384, NRL.
- Gosz, J. and Liu, W. K. (1996), 'Admissible approximations for essential boundary conditions in the reproducing kernel particle method', *Computational Mechanics* **19**, 120–135.
- Gravouil, A. and Combescure, A. (2001), 'Multi-time-step explicit-implicit method for non-linear structural dynamics', *International Journal for Numerical Methods in Engineering* **50**, 199–225.
- Günter, F. C. and Liu, W. K. (1998), 'Implementation of boundary conditions for meshless methods', *Computer Methods in Applied Mechanics and Engineering* **163**, 205–230.
- Hegen, D. (1996), 'Element free galerkin methods in combination with finite element approaches', *Computer Methods in Applied Mechanics and Engineering* **135**, 143–166.
- Hossain, M. A. and Yonge, D. R. (1992), 'Finite element modeling of single-solute activated-carbon adsorption', *Journal of Environmental Engineering* **118**, 238–252.
- Huerta, A. and Díez, P. (2000), 'Error estimation including pollution assessment for nonlinear finite element analysis', *Computer Methods in Applied Mechanics and Engineering* **181**, 21–41.
- Huerta, A. and Donéa, J. (2001), 'Time-accurate solution of stabilized convection-diffusion-reaction equations: I. time and space discretization', *Communications in Numerical Methods in Engineering* . submitted.
- Huerta, A. and Fernández-Méndez, S. (2000), 'Enrichment and coupling of the finite element and meshless methods', *International Journal for Numerical Methods in Engineering* **48**, 1615–1636.
- Huerta, A., Rodríguez-Ferran, A., Díez, P. and Sarrate, J. (1999), 'Adaptive finite element strategies based on error analysis', *International Journal for Numerical Methods in Engineering* **46**, 1803–1818.

- Huerta, A., Rodríguez-Ferran, A., Sarrate, J., Díez, P. and Fernández-Méndez, S. (2001), Numerical modelling, a tool to improve the design of active carbon canisters, in 'Abstracts of the Sixth U.S. National Congress on Computational Mechanics', Dearborn, Michigan.
- Huerta, A., Roig, B. and Donéa, J. (2001), 'Time-accurate solution of stabilized convection-diffusion-reaction equations: Ii. accuracy analysis and examples', *Communications in Numerical Methods in Engineering* . submitted.
- Hughes, T. (1987), *The Finite Element Method*, Prentice-Hall: New Jersey.
- Isaacson, E. and Keller, H. B. (1966), *Analysis of numerical methods*, John Wiley & Sons, New York. (Reprinted by Dover Publications, 1994).
- Jansen, K. E., Collins, S. S., Whiting, C. and Shakib, F. (1999), 'A better consistency for low-order stabilized finite element methods', *Computer Methods in Applied Mechanics and Engineering* **174**, 153–170.
- Johnson, G. R. and Beissel, S. R. (1996), 'Normalized smoothing functions for sph impact computations', *International Journal for Numerical Methods in Engineering* **39**, 2725–2741.
- Liszka, T. and Orkisz, J. (1980), 'The finite difference method at arbitrary irregular grids and its application in applied mechanics', *Computers and Structures* **11**, 83–95.
- Liu, W., Belytschko, T. and Oden, J. (1996), 'Meshless methods', *Computer Methods in Applied Mechanics and Engineering* **139**.
- Liu, W. K., Chen, Y., Jun, S., Chen, J. S., Belytschko, T., Pan, C., Uras, R. A. and Chang, C. T. (1996), 'Overview and applications of the reproducing kernel particle methods', *Archives of Computational Methods in Engineering, State of the Art Reviews* **3**, 3–80.
- Liu, W. K., Jun, S. and Zhang, Y. F. (1995), 'Reproducing kernel particle methods', *International Journal for Numerical Methods in Fluids* **20**, 1081–1106.
- Liu, W. K., Li, S. and Belytschko, T. (1997), 'Moving least square reproducing kernel methods.(i) methodology and convergence', *Computer Methods in Applied Mechanics and Engineering* **143**, 113–154.
- Liu, W. K., Uras, R. A. and Chen, Y. (97), 'Enrichment of the finite element method with reproducing kernel particle method', *Journal of Applied Mathematics* **64**, 861–870.
- Lucy, L. B. (1977), 'A numerical approach to the testing of the fission hypothesis', *The Astronomical Journal* **82**, 1013–1024.
- Monaghan, J. J. (1982), 'Why particle methods work', *SIAM Journal of Scientific and Statistical Computing* **3**, 422.
- Monaghan, J. J. (1988), 'An introduction to sph', *Computer Physics Communications* **48**, 89–96.

- Morton, K. W. (1996), Numerical solution of convection-diffusion problems, in K. W. M. R. J. Knops RJ, ed., 'Applied Mathematics and Mathematical Computation', Vol. 12, Chapman & Hall.
- Nayroles, B., Touzot, G. and Villon, P. (1992), 'Generalizing the finite element method: diffuse approximation and diffuse elements', *Computational Mechanics* **10**, 307–318.
- Oñate, E. and Idelsohn, S. (1998), 'A mesh-free finite point method for advective-diffusive transport and fluid flow problems', *Computational Mechanics* **21**, 283–292.
- Organ, D., Fleming, M., Terry, T. and Belytschko, T. (1996), 'Continuous meshless approximations for nonconvex bodies by diffraction and transparency', *Computational Mechanics* **18**, 225–235.
- Orkisz, J. (1998), Meshless finite difference method. i basic approach, in 'Proc. of the IACM-Fourth World Congress in Computational Mechanics', CIMNE.
- Perrone, N. and Kao, R. (1975), 'A general finite difference method for arbitrary meshes', *Computers and Structures* **5**, 45–58.
- Shakib, F. and Hughes, T. J. R. (1991), 'A new finite element formulation for computational fluid dynamics: Ix. fourier analysis of space-time galerkin/least-squares algorithms', *Computer Methods in Applied Mechanics and Engineering* **87**, 35–58.
- Suri, M. (1996), 'Analytical and computational assessment of locking in the *hp* finite element method', *Computer Methods in Applied Mechanics and Engineering* **133**, 347–371.
- Swengle, J. W., Hicks, D. L. and Attaway, S. W. (1995), 'Smoothed particle hydrodynamics stability analysis', *Journal of Computational Physics* **116**, 123–134.
- Tezduyar, T. E. and Park, Y. (1986), 'Discontinuity-capturing finite element formulations for nonlinear convection-diffusion-reaction equations', *Computer Methods in Applied Mechanics and Engineering* **59**, 307–325.
- Tezduyar, T. and Osawa, Y. (2000), 'Finite element stabilization parameters computed from element matrices and vectors', *Computer Methods in Applied Mechanics and Engineering* **190**, 411–430.
- Timoshenko, S. and Goodier, J. (1987), *Theory of elasticity (3rd edn)*, McGraw-Hill: New York.
- Vila, J. P. (1999), 'On particle weighted method and smooth particle hydrodynamics', *Mathematical Models and Methods in Applied Sciences* **9**, 161–209.
- Wagner, G. J. . and Liu, W. K. (2001), 'Hierarchical enrichment for bridging scales and mesh-free boundary conditions', *International Journal for Numerical Methods in Engineering* **50**, 507–524.

-
- Wagner, G. J. and Liu, W. K. (2000), 'Application of essential boundary conditions in mesh-free methods: a corrected collocation method', *International Journal for Numerical Methods in Engineering* **47**, 1367–1379.
- Zhu, T. and Atluri, S. (1998), 'A modified collocation method and a penalty formulation for enforcing the essential boundary conditions in the element free galerkin method', *Computational Mechanics* **21**, 211–222.